Stimuli-responsive Materials and Structures with Electrically Tunable Mechanical Properties

by

Jeffrey Thomas Auletta

B.S. Chemistry, University of North Florida, 2009

Submitted to the Graduate Faculty of

the Kenneth P. Dietrich School of Arts and Sciences in partial fulfillment

of the requirements for the degree of

Doctor of Philosophy

University of Pittsburgh

2017

UNIVERSITY OF PITTSBURGH

DIETRICH SCHOOL OF ARTS AND SCIENCES

This dissertation was presented

by

Jeffrey Thomas Auletta

It was defended on

March 30, 2017

and approved by

Tara Y. Meyer, Associate Professor, Chemistry

David H. Waldeck, Professor, Chemistry

Alexander Star, Professor, Chemistry

William W. Clark, Professor, Mechanical Engineering & Materials Science

Dissertation Advisor: Tara Y. Meyer, Associate Professor, Chemistry

Stimuli-responsive Materials and Structures with Electrically Tunable Mechanical Properties

Jeffrey Thomas Auletta, PhD

University of Pittsburgh, 2017

Stimuli-responsive Materials and Structures with Electrically Tunable Mechanical Properties

Jeffrey Thomas Auletta, PhD

University of Pittsburgh, 2017

Electricity, a convenient stimulus, was used to manipulate the mechanical properties of two classes of materials, each with a different mechanism. In the first system, macroscale electroplastic elastomer hydrogels (EPEs) were reversibly cycled through soft and hard states by sequential application of oxidative and reductive potentials. Electrochemically reversible crosslinks were switched between strongly binding Fe^{3+} and weak to non-binding Fe^{2+}, as determined by potentiometric titration. With the incorporation of graphene oxide (GO) into the EPE, a significant enhancement in modulus and toughness was observed, allowing for the preparation of thinner EPE samples, which could be reversibly cycled between soft and hard states over 30 minutes. Further characterization of this EPE by magnetic susceptibility measurements suggested the formation of multinuclear iron clusters within the gel.

Copper-derived EPEs which exploited the same redox-controlled mechanism for switching between hard and soft states were also prepared. Here, the density of temporary crosslinks and the mechanical properties were controlled by reversibly switching between the +1 and +2 oxidation states, using a combination of electrochemical/air oxidation and chemical reduction. In addition to undergoing redox-controlled changes in modulus, these EPEs exhibited shape memory.

In the second system, electroadhesion between ionomer layers was exploited to create laminate structures whose rigidity depended on the reversible polarization of the dielectric polymers. The role of the counter-ion in determining the intrinsic and electroadhesive properties of poly(ethylene-*co*-acrylic acid) ionomers in bi- and tri-layered laminate structures was examined. PEAA ionomers were prepared with three tetraalkylammonium cations (NR_4^+, R = methyl, TMA^+; ethyl, TEA^+; and propyl, TPA^+). Reflecting the increasing hydrophobicity of the longer alkyl chains, water uptake changed as a function of counterion with $TMA^+ > TEA^+ > TPA^+$. The glass transition temperatures, electrical resistivities, elastic moduli, and coefficients of friction were measured and found to depend on the cation identity. Overall, the cation-influenced mechanical properties of the ionomer determined the flexural rigidity range, but not the magnitude of the rigidity change, between the on and off states.

TABLE OF CONTENTS

LIST OF TABLES

LIST OF FIGURES

LIST OF EQUATIONS

LIST OF SCHEMES

SYMBOLS AND ABBREVIATIONS

A	ampere
AA	acrylic acid
APS	ammonium persulfate
BoPET	bi-axially oriented poly(ethylene terephthalate)
C	coulomb
C	capacitance
cm	centimeter
d	thickness
D	diffusion coefficient
d	day
°C	degrees Celsius
DSC	differential scanning calorimetry
E	Young’s modulus
ε'	dielectric constant, real component
ε''	dielectric constant, imaginary component
ε	dielectric constant
F	force (N)
FEP	fluorinated ethylene propylene
FT-IR	fourier transform infrared
G	shear modulus
g	gram
GPC	gel permeation chromatography
h	hour
Hz	hertz
i	current
i	$\sqrt{-1}$
I	Second area moment of inertia

kPa	kilopascals
M	Molar (moles per liter)
mA	milliamp
$\overline{M}_c$	molecular weight between crosslinks
mg	milligram
MHz	megahertz
µL	microliter
µm	micrometer
µmol	micromole
min	minutes
mmole	millimole
$\overline{M}_n$	number average molecular weight for linear polymer prepared without crosslinker
M_n	number average molecular weight
mol	mole
MPa	megapascal
N	newton
nm	nanometer
NMR	nuclear magnetic resonance
Ω	ohm
Pa	pascal
PAA	poly(acrylic acid)
PEAA	poly(ethylene-*co*-acrylic acid)
PEG-DA	poly(ethylene glycol)-diacrylate
PFA	perfluoroalkoxy copolymer
PNIPAM	poly(N-isopropylacrylamide)
PTFE	poly(tetrafluoroethylene)
PVDF	poly(vinylidene fluoride)
R	resistance
R_c	contact resistance
ref.	reference

ρ	resistivity
ρ	polymer density in kg/m^3
ρ'	resistivity, real component
ρ''	resistivity, imaginary component
RT	room temperature
s	second
SA	sodium acrylate
σ'	conductivity, real component
σ	conductivity
σ''	conductivity, imaginary component
SS	sodium 4-vinylbenzenesulfonate
T	temperature
Tc T_c	crystallization transition temperature
TEMED	tetramethylethylenediamine
T_g	glass transition temperature
TGA	thermogravimetric analysis
θ	phase angle
T_m	melting transition temperature
UV-Vis	ultraviolet-visible
V	volt
V	voltage (potential)
VP	4-vinylpyridine

PREFACE

Acknowledgements

During my time here at Pitt, I have certainly seen my fair share of highs and lows, but I'm thankful to have ridden so many great science-waves during my stay. Without the lulls, those button-worthy moments would not have felt so pleasant. I'm ever-grateful to the multitude of people who have helped me along the way.

First, I would like to thank my PhD advisor, Prof. Tara Meyer for her tireless commitment, encouragement, and support during my 6 years in her lab. Thank you for giving me the invaluable opportunity to have lively, and sometimes hotly-contested, scientific discussions. Your tutelage and passion for producing high-quality science have made me the scientist I am today. In addition to being an excellent mentor, you have always found a way to help both inside and outside of the lab. Thank you, Tara.

To the current and former members of the Meyer lab, Dr. Ryan Stayshich for pulling me in, Dr. Ryan Weiss for your afternoon musical melodies, Dr. Jian Li for your outside ideas, and Dr. Amy Short for your brilliance, thank you all for enriching my time in the lab. To Dr. Percy Calvo-Marzal, thank you for being so kind and teaching me the ropes of electrochemistry. To Shaopeng Zhang and especially Michael Washington, thank you for being there when I needed your ear and thoughts, in and out of the lab. To Gregory LeDonne and Colin Ladd, I am thankful to have worked with such bright and intelligent people as you. And to everyone else in the lab, Emily Barker, Jordan Swisher, and Jamie Nowalk, thank you for being such excellent lab mates.

I am grateful to have worked with a number of high-caliper undergraduate students, all of whom made strong contributions to their projects even when science just wouldn't go their way.

My thanks goes to Rachel Harris, Nicholas Perri, Kai Gronborg, and Michael Kerins for your contributions to the EPE project, especially Rachel who worked incessantly on the copper material. To Nicole Bauer and Michael Kerins, who took up the charge on two new projects and held strong in the face of seemingly endless disappointments; thank you for bringing your unique energy to your work.

I would also like to thank my committee members, Professors David Waldeck, Alex Star, and William (Buddy) Clark for your support. Thank you Prof. Waldeck for all of your helpful discussions on electrochemical results over the years and for allowing me access to your potentiostat. Thank you Prof. Star for your insights and discussions on carbon nanomaterials. And finally, thank you Prof. Clark for your helpful suggestions and perspective, and for giving me the opportunity to work closely with your students in engineering.

Thanks also to the members of my Proposal Committee, Prof. Sean Garrett-Roe for mentoring me through the process and providing me with timely feedback and advice. Thanks also to Professors Haitao Liu and Jill Millstone for serving on my proposal defense committee.

I would also like to extend a second thanks to Prof. Haitao Liu for his constant feedback and suggestions on the EPE project regarding graphene and graphene oxide materials. I am also indebted to Prof. Sunil Saxena, Mathew Lawless and Dr. Ishara Silva for their expertise in copper EPR spectroscopy. Thanks also to Rob Bressin and Evan Carder for your organic chemistry expertise, general life advice, and overall mayhem.

I would also like to thank my colleagues in the engineering department, Mark Delaney, Dr. Amin Motlagh, and especially Eliot George and Carlos Arguero for your thoughts and work on the electroadhesive project. Thanks also to Professor Qing-Ming Zhang for access to the dielectric impedance analyzer and to Professor Susan Fullerton for your guidance regarding collecting and

interpreting dielectric impedance results. Thanks also to Professor Tevis Jacobs for your helpful discussions on surface interactions.

I would also like to thank our collaborators in Mathematics, Professors David Swigon and Anna Vaintchen, and Dr. Hang Nguyen for your helpful discussions.

Thanks also to those who guided and encouraged me before beginning my graduate career, particularly Professor Michael Lufaso and Dr. Hank Eng for helping me discover my passion for research. Thanks to my former research group at the Mayo Clinic, Jacksonville, Professor Terrone Rosenberry, Dr. William Tay, Patricia Martin, Jeremy Nix, and those from the synthesis core: Dr. Abdul Fauq, Robert Chapman, and Dr. Ghulam Maharvi for your support in pursuing graduate school.

Thanks also to my friends and family for your constant encouragement and love. To my parents and brothers, thank you for your endless love and understanding. Thanks also to Kristi Howard for first introducing me to the wonderful city of Pittsburgh. To my friends in music Larry, Dan, Tim, and Josh, thanks for keeping the Vibe alive, and to Zach Reinert for being one of the best damn scientists and metal drummers I know.

And finally, to Meredyth Wegener, thank you for your love, encouragement, kindness, patience, and understanding. I would not be here without you.

1.0 INTRODUCTION

1.1 OVERVIEW

The overarching goal of this work was to develop materials and structures whose mechanical properties can be reversibly switched between hard and soft states using electricity. Presented here are two distinct strategies to control mechanical properties using electricity. The first strategy focuses on exploiting redox chemistry to reversibly control the coordination preferences of metal ions. The second strategy focuses on using polymer-based electroadhesion to bind the layers of laminates and reversibly switch the overall stiffness of the structure between rigid and flexible. In this introduction, focus is directed only to the first strategy and relevant background on stimuli-responsive materials. An overview of the second strategy will be given in Chapter 5.

Specific to strategy 1, the overall goal of this research was to design, synthesize, and understand the chemical nature of a class of hydrogels with redox-active crosslinks whose mechanical properties could be reversibly manipulated using an electrical input. We chose to explore an electrical stimulus rather than more common stimuli such as ionic strength, temperature and pH because this approach avoids the need for heating/cooling and does not require addition of reagents or collection of waste. Metal-crosslinked hydrogels were targeted because they offer advantages over other redox-based materials in their reversibility, range of moduli, scalability, and maintenance of three-dimensional shape in all states. The further elaboration of these materials through the addition of a graphene/graphene oxide filler was also explored with a goal of creating responsive hydrogels with a wider range of mechanical properties. In the long term these materials could be used for applications such as tissue engineering,[1] drug and protein delivery,[2-3] sensors,[4] actuators,[5] shape memory devices, and morphing structures.

1.2 STIMULI-RESPONSIVE MATERIALS

Utilizing a broad range of input, stimuli-responsive materials with switchable mechanical properties have been developed using light,[6] temperature,[7] pH, ionic strength, electric field,[8] magnetic field,[9] enzyme-catalysis,[10] and redox reactions[11]. Each of these strategies involves a stimuli-induced change in crosslink density, a key contributor to the mechanical response of the material to external force.

The mechanical properties of a polymer depend both on the structural properties of the polymer backbone and the nature of the chemically-induced interactions between polymer chains. Structurally, the molecular weight, polydispersity, chain orientation, degree of branching and chain entanglements influence physical interactions between polymer chains. Chemically, interactions are governed by the formation of crystalline domains, hydrogen bonds, ionic interactions, dipole-dipole interactions, and other inter- and intramolecular forces. These chemically-derived interactions are typically of greater importance than the fundamental structure of the polymeric backbone. These interactions also alter the distribution of crosslinks.

Crosslinks can be divided into two categories: permanent covalent, and temporary, non-covalent interactions. Many stimuli-responsive materials with alterable mechanical properties focus on the use of non-covalent interactions to change the crosslink density of the material. Below are described selected examples of previous reports that exploit this strategy.

Temperature is widely used as a method to alter polymer mechanical properties. Thermoplastics, for example, are used extensively in industry and exhibit dramatic changes in mechanical properties once heated past their glass transition temperature (T_g), forming a viscous mixture of flowing polymer chains. Other thermoresponsive polymers incorporate monomers such as N-isopropylacrylamide (NIPAM)[12] whose polymer, PNIPAM, exhibits a lower critical solution temperature (LCST). At room temperature, PNIPAM is hydrated and collapses to a dehydrated form when heated past its LCST, resulting in an increase in modulus.

Polymers containing sulfonated cellulose nanocrystals (CNCs) rapidly respond to hydration changes, eliciting dramatic changes in mechanical properties of the composite (Figure 1.1). As reported by Rowan and Weder, these CNCs, or "whiskers", when embedded in a polymeric matrix have high affinity for one another under dry conditions creating a stiff material. In the presence of a hydrogen-bonding solvent such as water, these whisker-whisker interactions are "switched-off" resulting in a softened material.[13]

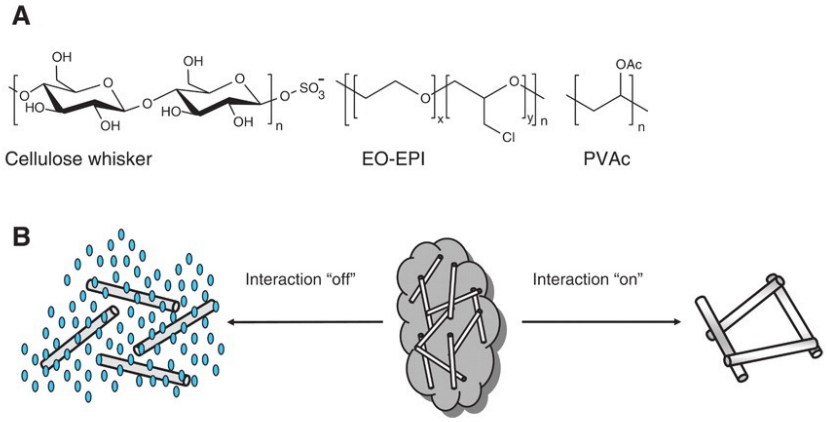

Figure 1.1 (A) Chemical structure of cellulose whiskers isolated through sulfuric acid hydrolysis of tunicate cellulose pulp and the matrix polymers used. (B) Schematic representation of the architecture and switching mechanism in the artificial nanocomposites with dynamic mechanical properties. (Adapted with permission from Capadona, J. R.; Shanmuganathan, K.; Tyler, D. J.; Rowan, S. J.; Weder, C., *Science*, **2008**, 319 (5868), 1370-1374. Reprinted with permission from AAAS).

In addition to heat and solvation, light can also be used to induce mechanical property changes depending on the nature of the light-absorbing component. Reversible photocrosslinking[14] and azo-benzene *cis-trans* isomerization have been shown to reversibly alter the Young's modulus of polymer films using UV-light (Figure 1.2a and b).[15] Reversible adhesives derived from metallosupramolecular polymers containing zinc complexes have also been shown to transform UV-light into heat, raising the temperature of the polymer above its T_g, softening the adhesive joint (Figure 1.2c).[16]

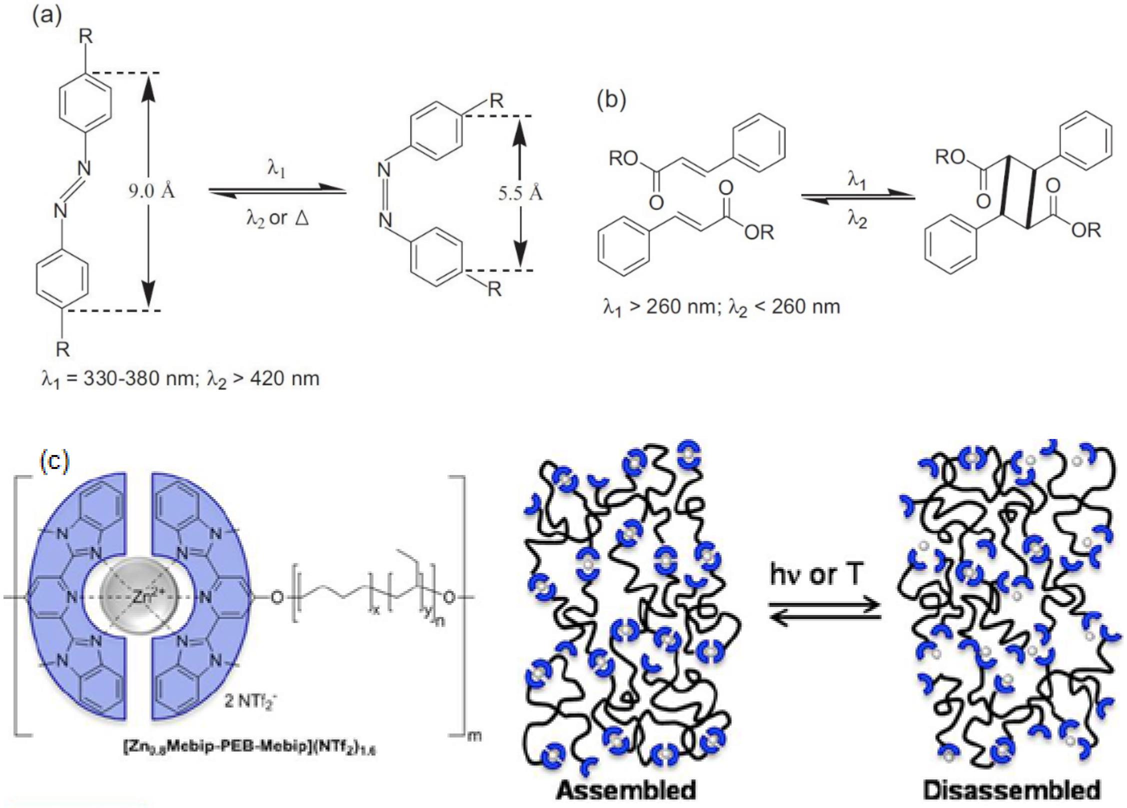

Figure 1.2 (a) *Trans-cis* photoisomerization of azobenzene groups; (b) photodimerization of the cinnamic acid group; (c) chemical structure of zinc cluster and schematic assembly and disassembly of supramolecular polymer with light or heat; (a) and (b) adapted from Jiang, H. Y.; Kelch, S.; Lendlein, A., *Adv. Mater.* **2006**, 18 (11), 1471-1475. Copyright © 2006 by John Wiley Sons, Inc. Reprinted by permission of John Wiley & Sons, Inc. (c) Reproduced with permission from Heinzmann, C.; Coulibaly, S.; Roulin, A.; Fiore, G. L.; Weder, C., *ACS Applied Materials & Interfaces* **2014**, 6 (7), 4713-4719. Copyright 2014 American Chemical Society.

The repetitive application of mechanical force has also been used to alter mechanical properties, known as strain-stiffening. When subjected to recurring elastic stress, irreversible stiffening can occur in elastomeric materials containing carbon nanotubes[17] or liquid crystals.[18] Similarly, materials containing mechanophores, or groups reactive to mechanical deformation, can induce increases in modulus by mechanical bond scission, increasing crosslink density.[19-20] Collagen containing biomaterials such as ligaments and tendons also exhibit reversible strain-stiffening.[21-22]

Related to this work, electrical current has been used to alter mechanical properties. Here, current flow causes Joule-heating of the material past its T_g, making this stimulus a sub-class of thermoresponsive materials.[23-24] This response is distinct from the work presented herein as redox reactions are not employed to alter the mechanical properties.

Supramolecular materials have also gained considerable attention for the range of stimuli possible and types of crosslinks which may be formed and encompass many of the methods given above.[25] β-cyclodextrins (host-guest interactions),[26] quadruple hydrogen-bonding motifs,[27] diblock-copolymers,[28] electrostatic interactions (such as polyelectrolyte complexes),[29-30] metal-ligand coordination, and π-π stacking[31] have all been utilized to create different materials which respond to stimuli.

The theme relating all of these materials with alterable mechanical properties is the modification of chain-chain interactions via a stimulus, (or multiple stimuli), resulting in a change in crosslink density. While these approaches all present elegant solutions to the problem, an unmet need exists for materials whose mechanical properties can be altered without the use of external reagents or heating/cooling where the material maintains mechanical integrity in both soft and hard states. Electrical input is particularly useful for achieving this aim since it offers spatial control of the stimulus, does not require the addition or removal of reagents or heating. Metal-ligand interactions are especially amenable to this approach as oxidation state-dependent binding and crosslinking is well-understood. Indeed, others have utilized this technique, but until recently, only a handful of examples existed which utilized electricity alone without the need for chemical reagents to reversibly alter mechanical properties where three-dimensional shape is preserved. In the following sections, our approach to this problem is presented and background is given on hydrogels, hydrogel nanocomposites, and other redox-responsive materials which utilize oxidation state dependent binding to alter mechanical properties. Highlighted are materials harnessing metal ions as reversible crosslink points, with emphasis on those featuring electrical input as stimulus.

1.3 HYDROGELS AND MATERIALS WITH REDOX-ACTIVE CROSSLINKS

1.3.1 Redox-responsive materials with tunable mechanical properties

1.3.1.1 Metal-ion based materials with changes in primary coordination sphere

Numerous examples exist of stimuli-responsive metal-containing polymers and supramolecular materials which exploit metal ion oxidation state.[32-36] Of particular relevance to our work are those systems that rely on redox-driven changes in coordination around the metal center. Iron, due to the accessibility and stability of the +2 and +3 oxidation states is one of the most widely used metals. Tong and co-workers have, for example, reported on the reversible sol-gel transitioning of poly(acrylic acid) (PAA) using the Fe^{2+}/Fe^{3+} redox couple as controlled by light, air oxidation,[37] or an applied potential.[38] The dynamic bonding of Fe^{3+} with carboxylate ligands has also been utilized for autonomous self-healing of crosslinked PAA hydrogels as reported by Wang and Nie.[39] Reduction is also intrinsic to the photodegradation of Fe^{3+}-crosslinked alginate gels for biocompatible scaffolds as reported by Melman and coworkers[40] and also by Ostrowski.[41]

Other transition metals have been utilized, including the cobalt-based supramolecular polymers by Terech and coworkers,[42] and the copper-based systems by the Rowan and Shinkai groups.[43-44] Also related is the Cu/Cu^{2+} ionoprinting methodology reported by Velev and coworkers.[45] Copper redox was also used to promote self-healing of hydrophobic gels as reported by Mashelkar and coworkers.[46]

1.3.1.2 Materials with intact complexes that undergo changes in oxidation state without changes in primary coordination sphere

Indirectly related, but also relevant, are systems that involve redox-promoted changes in the charge on intact metal complexes. Harada and coworkers have, for example, used a redox strategy to control the host-guest interactions between β-cyclodextrin and ferrocenyl moieties and have demonstrated in their materials reversible associations,[47] self-healing,[48] and mechanical motion.[49] Poly(ferrocenyl siloxanes) have been utilized to prepare color-tunable displays as reported by Manners[50-51] and redox-controlled actuators as demonstrated by Hempenius, Vancso and coworkers.[35] In another case, ferrocyanide was utilized to control reversibly the degree of swelling of polyelectrolyte multilayers.[52]

1.3.1.3 Other redox-based mechanisms which do not utilize metal ions or coordination complexes

Finally, there are some interesting examples of hydrogel materials that exploit redox as a stimulus but are not metal-based. Disulfide crosslinking, for example, has been utilized to control crosslink density in a variety of systems.[53-56] Electrochemical control of crosslinking has also been demonstrated by altering the charge on polyviologens incorporated in polyelectrolyte multilayers.[30] Quadruple hydrogen bonding motifs have also been used to prepare redox-responsive gelator systems.[57]

1.3.2 Electroplastic elastomers

The goal of this project was to develop and characterize a new class of polymeric materials, herein termed electroplastic elastomers (EPEs), whose mechanical properties can be reversibly switched on a macroscale using electricity. The functional mechanism of the material relies on metal ion redox-state controlled formation and breakage of polymer chain crosslinks (Figure 1.3). Redox-stimulated systems that exhibit reversible changes in mechanical properties have been reported in the literature, but these systems typically involve switching between solution and gel phases.[37-38] The Fe^{2+}/Fe^{3+} redox couple was chosen for developing these EPEs because this system is both well-behaved and well-understood; these two ions can be interconverted in a convenient potential window. As iron ions in different oxidation states have distinct coordination preferences—Fe^{3+} binds more strongly than Fe^{2+} to “hard” ligands—the change in oxidation state can be used to control the degree of crosslinking in a polymer bearing hard carboxylate side-groups (Figure 1.3). Given the correlation between crosslink density and the stiffness of polymeric materials as discussed above, it follows that the mechanical properties of the bulk material should be reversibly controlled by the interconversion of Fe^{2+} and Fe^{3+}.[58]

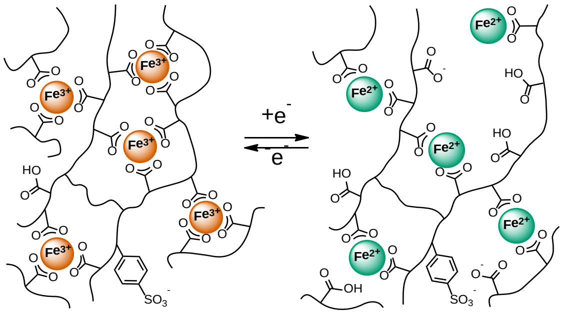

Figure 1.3 Representation of cross-linking in strongly cross-linked Fe^{3+} hydrogel (left), and weakly cross-linked Fe^{2+} hydrogel (right).

We have chosen to focus our attention on hydrogels as these materials allow for the preparation of bulk scale objects without the need for large quantities of synthetically challenging monomers. Polymeric hydrogels are a particularly suitable medium in which to create materials that respond to environmental changes. The aqueous environment is amenable to the establishment of equilibria that can be reversibly manipulated and the swelling/deswelling of the gel amplifies responses caused by changes in inter- and intramolecular interactions.[28, 59-60]

1.3.3 Hydrogels

Hydrogels are three-dimensional water-swollen chemically crosslinked polymeric networks typically prepared by free-radical polymerization from hydrophilic monomers.[61-62] The presence of permanent chemical crosslinks renders the network insoluble. Hydrogels can be prepared from one (homopolymer), two (copolymer), or three or more monomers and, depending on the nature and combination of the monomers used, the hydrogel can be neutral, anionic, cationic, or amphoteric.[61-62] A di-functional or multi-functional monomer can be added to crosslink the network, ideally crosslinking all chains (Figure 1.4a and b). Network structure and morphology is an important component in determining the mechanical and swelling properties of the gel. The mechanical properties of the system and the diffusion of molecules through the network are related to three key properties of the hydrogel: the molecular weight between crosslinks ($\overline{M}_c$), the degree of swelling, and the network mesh size. In addition to chemical crosslinks, physical chain entanglements are possible (Figure 1.4c). Defects such as unreacted monomer ends and loops (Figure 1.4d and e) can also occur. Loops and dangling ends do not contribute to the elastic properties since they are not connected to the network.[61-62]

Figure 1.4 Representation of network structure in hydrogels. (a) ideal network. (b) Multifunctional crosslinks. (c) Physical entanglements. (d) Unreacted dangling ends. (e) Loops.

Much research has been devoted to improving the mechanical properties of hydrogels since these gels are typically very weak and brittle, limiting their potential applications.[63] Tough hydrogels have been prepared in a variety of ways. Interpenetrating network (IPN) hydrogels have been synthesized by polymerizing a second network into a first, highly crosslinked network, resulting in increased entanglements.[64] Nanofillers such as clay platelets or graphene oxide have also been used to enhance the mechanical properties of hydrogel materials. (For reviews on the use of nanofillers in hydrogels, see Section 1.4).

1.3.3.1 Theory of rubber elasticity

Hydrogels behave similarly to rubber materials and will respond nearly instantaneously to an applied stress. When deformed to a small extent, (strain less than 20-30%),[65-66] the gel will typically recover to its initial state. Under these conditions, the response of the material can be approximated as elastic. From the classical equation of state for rubber elasticity, a relationship between the applied stress and the deformation under uniaxial compression or extension can be derived (1.1).[65, 67] From analysis of the stress-strain curve, important structural information about the hydrogel, in conjunction with swelling measurements, can be obtained, such as the molecular weight between crosslinks, the shear modulus (G), and the Young's Modulus (E = 3G for a material within its elastic regime).

For a polymer crosslinked in the solid state or without solvent, the stress-strain behavior can be predicted by

$$\sigma = \frac{\rho R T}{\overline{M}_c}\left(1 - \frac{2\overline{M}_c}{\overline{M}_n}\right)\left(\alpha - \frac{1}{\alpha^2}\right) \qquad (1.1)$$

where σ is the stress, ρ is the density of the polymer (kg/m^3), R is the ideal gas constant, T is the absolute temperature, $\overline{M}_c$ is the molecular weight between crosslinks, $\overline{M}_n$ is the number average molecular weight for a linear polymer prepared under the same conditions without crosslinker, and α is the extension ratio ($\alpha = L/L_0$) where L is the length of the sample at a given time and L_0 is the initial length). The second term is a correction for dangling chain ends and can be approximated as 1 when $\overline{M}_n \gg \overline{M}_c$.[66-67]

In the case of a network crosslinked in the solid state and then swollen in a solvent, the stress-strain relation becomes

$$\sigma = \frac{\rho R T}{\overline{M}_c}\left(1 - \frac{2\overline{M}_c}{\overline{M}_n}\right)\left(\alpha - \frac{1}{\alpha^2}\right)\left(\nu_{2,s}\right)^{1/3} \qquad (1.2)$$

where $\nu_{2,s}$ is the polymer volume fraction in the swollen state, and can be determined from buoyancy and swelling experiments,[61, 68]

$$\nu_{2,s} = \frac{V_P}{V_{g,s}} \tag{1.3}$$

$$V_P = \frac{W_{a,d} - W_{n,d}}{\rho_n} \tag{1.4}$$

$$V_{g,s} = \frac{W_{a,s} - W_{n,s}}{\rho_n} \tag{1.5}$$

where V_P is the volume of the polymer, $W_{a,d}$ and $W_{n.d}$ are the dry weight in air and in a non-swelling solvent (such as hexanes), $W_{a,s}$ and $W_{n,s}$ are the swollen weight in air and in a nonsolvent, and ρ_n is the density (g/mL) of the nonsolvent.

Finally, for the case of a polymer crosslinked in the presence of a solvent and then swollen to equilibrium (representative of most hydrogels), the stress-strain relation becomes

$$\sigma = \frac{\rho_{2,r} RT}{\overline{M}_c}\left(1 - \frac{2\overline{M}_c}{\overline{M}_n}\right)\left(\alpha - \frac{1}{\alpha^2}\right)\left(\frac{\nu_{2,s}}{\nu_{2,r}}\right)^{1/3} \tag{1.6}$$

$$\nu_{2,r} = \frac{V_P}{V_{g,r}} \tag{1.7}$$

$$V_{g,r} = \frac{W_{a,r} - W_{n,r}}{\rho_n} \tag{1.8}$$

where $\rho_{2,r}$ is the density of the polymer in the relaxed state, $\nu_{2,r}$ is the polymer volume fraction in the relaxed state after polymerization but before swelling, $W_{a,r}$ and $W_{n,r}$ are the weight in air and in a nonsolvent after crosslinking, respectively.[61, 68]

1.4 CLAY AND GRAPHENE OXIDE NANOCOMPOSITES

Incorporation of nanomaterials in hydrogels imparts unique features to these typically very soft materials. The nanofiller can have a pronounced influence on the mechanical properties of the system depending on the nature of its interaction with the monomers used and the resulting network structure. In the case of poly(acrylamide)/clay nanocomposite (NC) gels, the clay nanoplatelets act as multifunctional crosslink points (Figure 1.5).[69-70] Additionally, the polymer chains adsorb to the surface of the clay sheets, such that more energy is required to desorb the polymer from the sheets at high extensions ($\alpha \sim 3$). The combination of these characteristics improve the toughness and extensiblity (over 1400% strain) compared to gels prepared with organic crosslinker N,N′-methylenebisacrylamide (BIS) alone, which break at ~500% strain.[70]

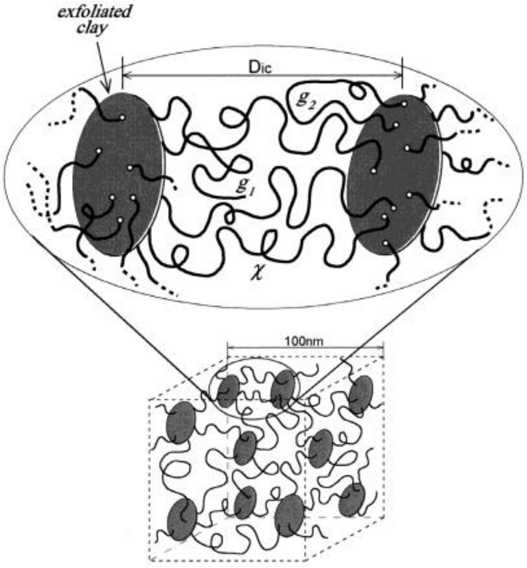

Figure 1.5 Schematic illustration of clay nanocomposite hydrogel. D_{ic} is the interparticle distance of exfoliated clay sheets. χ, g_1, and g_2 represent cross-linked chain, grafted chain, and looped chain. Reproduced with permission from Haraguchi, K.; Farnworth, R.; Ohbayashi, A.; Takehisa, T., Compositional Effects on Mechanical Properties of Nanocomposite Hydrogels Composed of Poly(N,N-dimethylacrylamide) and Clay. *Macromolecules* **2003**, *36*, 5732-5741. Copyright (2003) American Chemical Society.[71]

Graphene and graphene oxide (GO) have received a great deal of attention in recent years due to the excellent mechanical, thermal, and electrical properties of the one-atom thick graphene sheet.[72] Accordingly, because of the potential to imbue materials with graphene's extraordinary properties, the field of graphene and GO polymer composites has grown rapidly.[73-78] Due to the limited solubility of graphene in aqueous systems and the difficulty associated with obtaining large quantities of graphene, most hydrogel composites utilize GO as the nanofiller. Oxidation of graphite via Hummers' method[79] yields oxidized graphite which after exfoliation in water forms a stable dispersion of GO sheets. Oxidation significantly disrupts the π-conjugated network and introduces multiple oxygen-functionalities including epoxy and hydroxyl groups on the basal planes and carbonyl, carboxyl, and hydroxyl functionalities on the edges (Figure 1.6).[80]

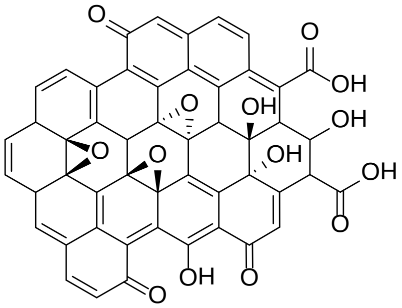

Figure 1.6 Graphene oxide with ether, hydroxyl, carbonyl, and carboxyl functional groups.

Stimuli-responsive GO hydrogel composites with improved mechanical properties have been made by including a small weight fraction of GO in the polymer mixture.[81-83] Hydrogels have also been prepared using surface-modified graphene oxide.[84] Relevant to this work, PAA GO-composite hydrogels crosslinked with BIS have been reported[82] and the authors hypothesized that GO functioned similarly to clay nanoplatelets as proposed by Haraguchi for NC gels.[85] A microstructure is formed by the GO sheets and organic crosslinker BIS (Figure 1.7). The ratio of BIS to GO influences the mechanical properties. If the ratio of BIS to GO is high, the network will be saturated with BIS and an organic crosslink network structure will form in addition to the microstructure. During elongation, stress is localized to the organic crosslinks and the gel will fracture at low elongations since only a small number of chains are available to dissipate the applied force. When the BIS to GO ratio is low, the crosslink architecture is dominated by the microstructure and contributes to the enhancement of elastic properties since the applied force can be distributed more effectively and evenly throughout the network.[82] Additionally, tough and stretchable GO-poly(acrylamide) hydrogels without any organic crosslinker have been prepared by standard free-radical polymerization[86] and using graphene peroxide (which functions as initiator and crosslinker).[87]

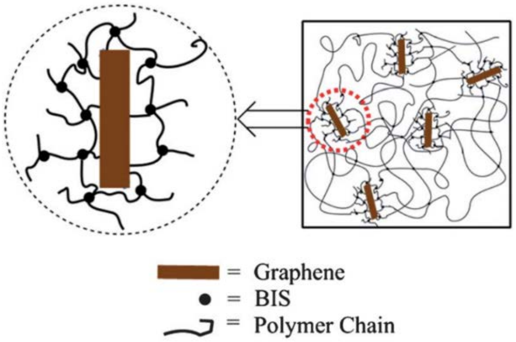

Figure 1.7 Proposed microstructure of graphene oxide in PAA hydrogel with BIS as crosslinker. Reproduced from Shen, J.; Yan, B.; Li, T.; Long, Y.; Li, N.; Ye, M., *Soft Matter*, **2012**, 8 (6), 1831-1836 with permission from The Royal Society of Chemistry.[82]

The synthesis of graphene oxide significantly disrupts the π-network rendering the material non-conductive. Restoration of the π-network can be accomplished by chemically or thermally reducing the oxygen functionalities on the basal plane of GO to form reduced graphene oxide (rGO). Varying levels of success have been attained depending on the reduction method, but the restored properties are typically less than those of pristine graphene.[73, 78, 88]

Another interesting property of GO is the response to multivalent cations. Shi and coworkers studied the effect of metal ion valency on the gelation of GO and found that monovalent cations (salts used: NaCl, KCl, and $AgNO_3$) did not induce gelation but that divalent and trivalent metal cations could (salts used: $CaCl_2$, $MgCl_2$, $CuCl_2$, $Pb(NO_3)_2$, $CrCl_3$, and $FeCl_3$). The authors attributed the response to metal ion coordination to carboxyl and carbonyl groups present on the GO sheets.[89] Similarly, Ruoff and coworkers reported on modified GO paper doped with less than

1 wt% Ca^{2+} or Mg^{2+} which enhanced the mechanical properties of the GO paper. Here, the authors specifically attributed the improvement in modulus to the coordination of metal ions to the carboxylate groups present on the edges of the GO sheets.[90] This property could be easily exploited in EPEs since binding of Fe^{3+} to carboxylate groups along the polymer backbone is utilized in forming crosslinks.

1.5 ELECTROAHESIVE LAMINATES WITH REVERSIBLE CHANGES IN FLEXURAL RIGIDITY

As an alternative to the direct control of bulk crosslink density within the material, our second strategy, as mentioned in the overview of this introduction, focuses on the use of electroadhesion to reversibly alter the rigidity of layered structures (Chapter 5). Note that this strategy does not rely on changes in the *modulus* of the polymer itself but on changes in the *rigidity* of structures composed of polymeric electroadhesive laminates. As shall be seen in Chapters 2,3, and 4, the materials presented therein undergo reversible changes in crosslink density but are inherently limited by diffusion, requiring minutes to hours to observe macroscopic changes in mechanical properties. Electroadhesion was pursued as a mechanism for reversibly bonding the layers of laminate structures as the adhesive force generation is both rapid and large in magnitude, allowing for a greater change in rigidity between on and off states.

A full introduction to electroadhesion and its application to laminate structures with alterable flexural rigidity will be given in Chapter 5. The fundamentals of electroadhesion and the two main forces, Coulombic and Johnsen-Rahbek, are detailed. The governing equations for the Coulomb force and Johnsen-Rahbek force are described. An introduction to beam theory and its application to multi-layered laminates is given with descriptions of the theoretical changes in flexural rigidity for multilayered structures.

1.6 THESIS OVERVIEW

This thesis is divided into two projects, the first of which is detailed in Chapters 2, 3, and 4 and the second of which is detailed in Chapter 5. Both of these projects involve tuning the mechanical properties of materials or structures using an electrical input.

Chapter 2 describes the creation of the first-generation EPE material using Fe^{2+}/Fe^{3+} chemistry. The conditions for electrochemical reversibility are described and presented. Transition times between hard and soft states required hours for bulk electrochemical conversion, as these systems are diffusion-limited.

Chapter 3 describes the copper-based EPE. The Cu-EPE could be reversibly cycled between hard and soft states using reducing agent and air exposure, allowing for a striking shape memory response. Electrochemical reduction resulted in the irreversible formation of Cu-metal on the electrode, resulting in only partial re-oxidation to Cu^{2+} and partial restoration of initial modulus.

Chapter 4 discusses in more detail the mechanism controlling the redox switching in the Fe^{2+}/Fe^{3+} system and presents a second-generation Fe-EPE with graphene oxide (GO) as nanofiller. Potentiometric titrations were performed and the binding constants of Fe^{3+} and Fe^{2+} for carboxylate ligands of the gel were determined. At the operating pH of 1-2, Fe^{3+} was found to bind strongly whereas Fe^{2+} did not show any coordination. Magnetic susceptibility measurements suggested the formation of multinuclear iron clusters in the Fe^{3+}-gel. The inclusion of GO enhanced the Young’s modulus and toughness of the as-prepared gels, allowing for preparation of thin, (80 - 100-µm thick) samples. While still diffusion-limited, these thin samples could be transitioned between hard and soft states within minutes.

Chapter 5 presents our work on the second project utilizing polymer-based electroadhesion to reversibly alter the flexural rigidity of laminate structures. Ionomers were prepared with a series of three tetraalkylammonium cations. Glass transition temperatures, electrical resistivities, elastic moduli, and coefficients of friction were measured and the effects on overall electroadhesion were determined.

2.0 MANIPULATING MECHANICAL PROPERTIES WITH ELECTRICITY: ELECTROPLASTIC ELASTOMER HYDROGELS

(Portions of this work were published previously and are reprinted with permission from Calvo-Marzal, P.; Delaney, M. P.; Auletta, J. T.; Pan, T.; Perri, N. M.; Weiland, L. M.; Waldeck, D. H.; Clark, W. W.; Meyer, T. Y. *ACS Macro Letters* **2012**, 1 (1), 204-208. Copyright 2012 American Chemical Society.)

This work was performed in collaboration with Dr. Percy Calvo-Marzal, Tianqi Pan, Nicholas Perri from the Meyer group. Mark Delaney from the Clark group helped with mechanical characterization. Catalina Achim from Carnegie Mellon University carried out the Mössbauer measurements.

2.1 OVERVIEW

Nature integrates phenomena on multiple length scales and energy domains to establish extraordinary ranges of functionality. Among the numerous chemo-electro-mechanical examples are the rapid pressure and stiffness evolution observed in the motion of the Venus flytrap and neurological muscle control in animals.[91-92] To create systems that exhibit responses in one domain or scale based on stimuli in another, Nature typically couples processes that transform the stimulus to a response through pathways or networks of mediating processes (Figure 2.1)[93-94] We report the creation of a new material that uses electricity as a stimulus to produce, reversibly, a change in bulk-scale stiffness as a response (Figure 2.2). We term this new class of materials electroplastic elastomer hydrogels (EPEs). Herein, we describe the synthesis, functional mechanism, and potential applications of this first-generation material.

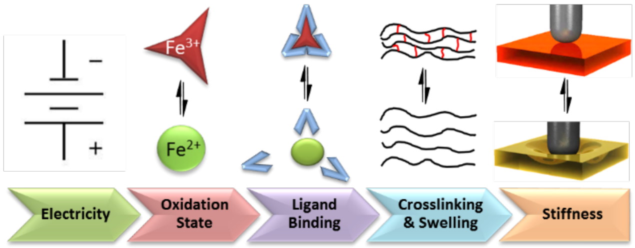

Figure 2.1 Electroplastic elastomer mechanism. Multi-step pathway that reversibly converts electricity to a change in bulk stiffness in iron-crosslinked electroplastic elastomer hydrogels.

We chose to utilize the Fe^{2+}/Fe^{3+} redox couple for developing these EPEs because this system is both well-behaved and well-understood; these two ions can be interconverted in a convenient potential window. As iron ions in different oxidation states have distinct coordination preferences—Fe^{3+} binds more strongly than Fe^{2+} to “hard” ligands—the change in oxidation state can be used to control the degree of crosslinking in a polymer bearing hard carboxylate side-groups. Given the known correlation between crosslink density and the stiffness of polymeric materials, it follows that the mechanical properties of the bulk material should be reversibly controlled by the interconversion of Fe^{2+} and Fe^{3+}.

Although the creation of materials that respond to external stimuli is one of the most active frontiers of current materials development,[95-101] EPEs display a unique and valuable *combination* of properties not found in any other system: 1) reversible changes in mechanical stiffness using only electrical input and 2) 3D-macroscale dimensions in all states. The mechanism that underlies the change in bulk mechanical properties of EPEs, forming and breaking polymer chain crosslinks, has been exploited by others. However, few of these materials are reversible and of those that are, all have stimulus-defined limitations not shared by EPEs. For example, many systems are not self-contained—they require manual addition and removal of solvents or chemicals for each response.[102-103] Other systems are stimulated by temperature[104-105] which, unlike electricity, is difficult to direct to a specific location in the material. Moreover, the required activation temperatures could prove impractical to access and/or implement for specific applications. A need exists for materials whose properties can be adjusted on-demand without requiring a change in the overall environment of the material. Electricity, which is employed as the stimulus for EPEs, satisfies these requirements and offers practical advantages including ease of access, portability, and a sophisticated technology infrastructure.

The second key property of the EPEs, one not shared by other electrically reversible systems, is the maintenance of a three-dimensional shape in all states. Electrically-stimulated polymeric materials that exhibit mechanical property changes other than osmotically-controlled mechanical actuation[106-108] are generally stimulated either as cast films (not macroscopic in all dimensions),[97, 109] or they undergo a transformation between sol and gel states (shape is neither controlled nor maintained).[28, 37-38, 44, 110-113] Tong and coworkers, for example, demonstrated that using either electrochemistry or light the Fe^{2+}/Fe^{3+} redox couple can be used to induce a sol-gel transition in poly(acrylic acid).[37-38] EPEs, in contrast, have macroscopic dimensions in all directions and maintain a non-zero stiffness in all states, which enables shape to be retained while compliance is tuned.

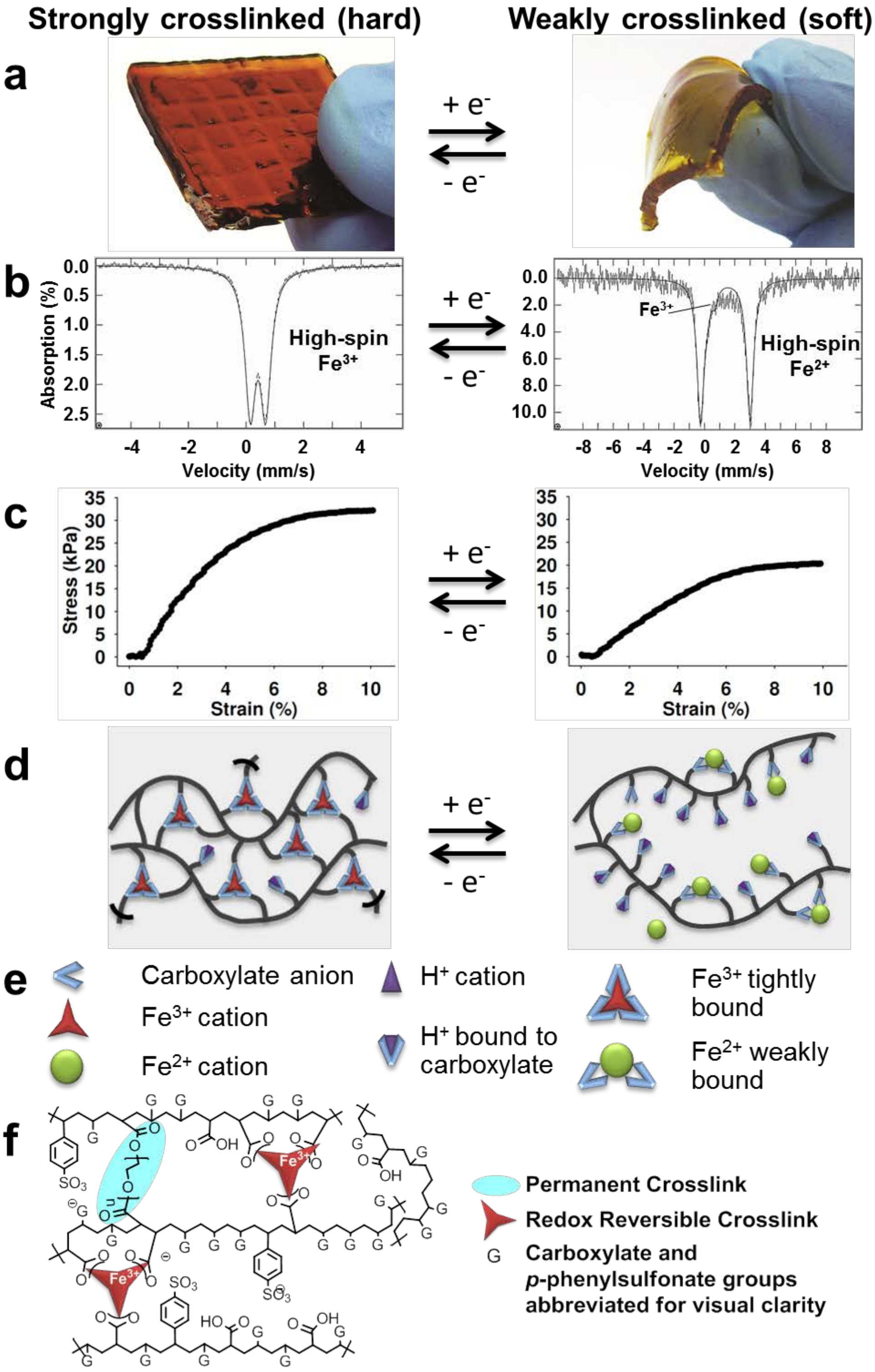

Figure 2.2 Redox-mediated switching between hard and soft states for iron-based electroplastic elastomer. Reversible electrochemical conversion of stiff Fe^{3+}-crosslinked hydrogel (left) to softer Fe^{2+} hydrogel (right). (a) Hydrogel in oxidized (left) and reduced (right) states held in gloved hand. (b) Mössbauer spectra of hydrogel samples in the oxidized and reduced states. (c) Mechanical stress/strain curves for EPEs in the oxidized and reduced states under compression. (d) Cartoons depicting differences in intra- and interchain crosslinking for Fe^{3+} and Fe^{2+}. (e) Key for d. (f) Representation of the chemical structure of the hydrogel in the oxidized state.

2.2 RESULTS AND DISCUSSION

2.2.1 EPE synthesis

EPE samples were prepared by simple free-radical copolymerization of commercially purchased monomers under standard conditions. Sodium acrylate, sodium (4-styrene sulfonate), and polyethylene glycol diacrylate (PEG-DA, M_n = 575) in a weight ratio of 12:8:1 were reacted in aqueous solution with an ammonium persulfate catalyst at 85 °C for 1.5 hours to give a soft, colorless hydrogel. The presence of the permanent PEG-DA crosslinks gives the hydrogels a baseline shape defined by the reaction vessel. Cation exchange of sodium ions for Fe^{2+} or Fe^{3+} was accomplished by submersion of the hydrogel in a solution of 2.0 M $FeCl_2$ or $FeCl_3$ and 0.5 M citric acid for a period of 20-48 hours. Exchange with Fe^{2+} produced samples that were pale yellow-green in color and slightly smaller than the original hydrogel, due to coordinative crosslinking (). Samples prepared with Fe^{3+} were orange-red and even more contracted in dimension—up to 50% smaller in thickness than the pre-doped samples (Figure 2.3). Hydrogels were transparent and appeared homogeneous throughout. Although the standard samples prepared for this article are relatively small, 2.5 x 2.5 x 0.2 cm after doping with Fe^{3+}, the procedure is inherently scalable to nearly any sample size.

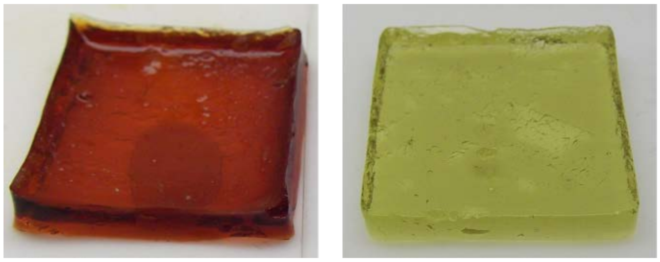

Figure 2.3 Iron-doped hydrogels. Initial appearance of an Fe^{3+}-doped hydrogel (left) and an Fe^{2+}-doped hydrogel (right).

2.2.2 Iron content

Samples prepared independently with comparable Fe^{2+} and Fe^{3+} ion content (Table 2.1, ca. 1.2 mmol/cm^3) exhibited more than an order of magnitude difference in modulus when subjected to mechanical testing using an indentation methodology. Compressive moduli of 0.06 and 2.1 MPa were measured for Fe^{2+} and Fe^{3+} samples that were prepared, measured, and analyzed for iron content using identical protocols. Moduli higher than 2.1 MPa can be achieved for Fe^{3+} samples by adjustments in doping conditions.

Table 2.1 Mechanical properties of Fe^{2+}- and Fe^{3+}-doped hydrogels.[a]

Dopant	Fe^{2+} (mmoles)	Fe^{3+} (mmoles)	Young's Modulus (MPa)	Fe:carboxylate
$FeCl_2$	2.116	–	0.06	1:2.6
$FeCl_3$	–	2.210[b]	2.1	1:2.5

[a]Sample size ca. 2.5 x 2.5 x 0.3 mm = 1.875 cm^3; [b] Fe^{3+} per volume of 1.2 mmol/cm^3.

2.2.3 Electrochemical transitioning of EPE and change in mechanical properties

The mechanical properties of the EPE samples are controlled by the electrolytic interconversion of the Fe^{3+} and Fe^{2+} within the same bulk sample. An EPE sample of standard dimensions was prepared directly on a glassy carbon electrode (Figure 2.4). After in-situ Fe^{3+} exchange the sample was protected from exposure to light and subjected to a reducing potential of -0.8 V for 18 hours in an electrolyte solution of 0.5 M citric acid and 2.0 M $FeCl_2$. The sample became softer to the touch, pale orange-yellow in color, and was visibly swollen relative to the initial state (Figure 2.2a-right). Exchange of the tightly bound Fe^{3+} with the Fe^{2+} present in the electrolyte solution (necessary for the reduction step in samples that will be cycled between states, *vide infra*) is not significant—a control submerged for the same period in the same solution without electrolysis, did not soften nor change color. It is important to note that the reduction occurs analogously when the electrolyte solution comprises only KNO_3 (0.2 M, pH 1). Also, leaching of hydrogel-bound Fe^{3+} into the electrolyte solution is negligible under these conditions. Mössbauer analysis of both the starting sample and the sample produced by reduction established unambiguously that a nearly complete conversion of the high-spin Fe^{3+} in the sample to high-spin Fe^{2+} occurred (Figure 2.2c). Air oxidation during Mössbauer sample preparation and/or incomplete reduction is responsible for the small Fe^{3+} shoulder (< 15%). The sample color for the reduced EPEH, which is orange-yellow rather than the yellow-green that is characteristic of freshly prepared Fe^{2+}-doped hydrogels, is likewise consistent with the presence of a small fraction of the more intensely colored Fe^{3+} crosslinks.

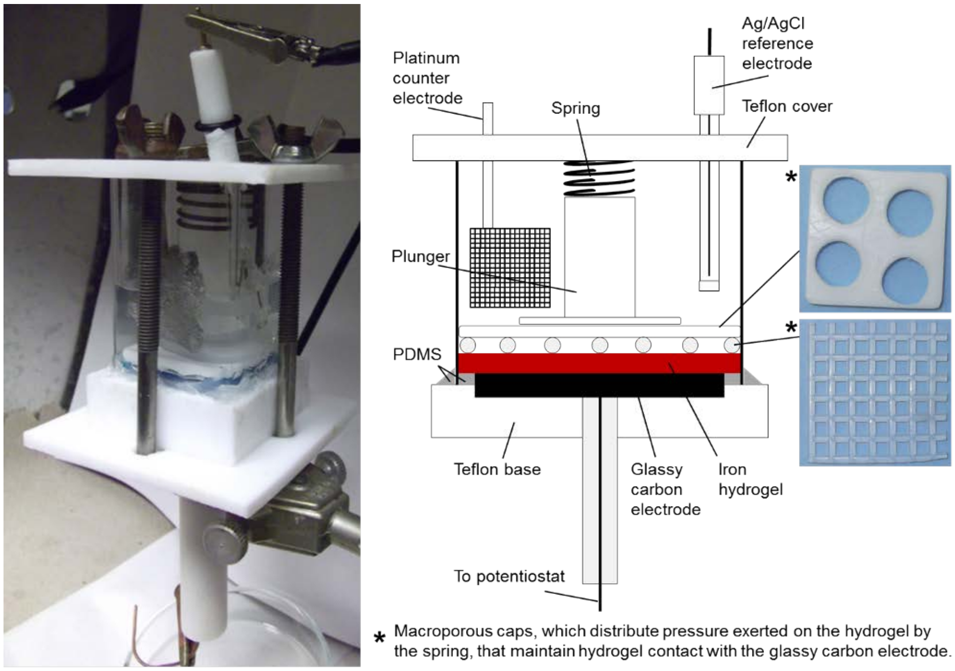

* Macroporous caps, which distribute pressure exerted on the hydrogel by the spring, that maintain hydrogel contact with the glassy carbon electrode.

Figure 2.4 Electrochemical cell design. Photograph of electrochemical cell (left). Schematic diagram of electrochemical cell design (right).

Oxidation of a freshly prepared Fe^{2+} EPE in 2 M $FeCl_2$, 0.5 M citric acid produced the opposite changes in color and mechanical properties. After oxidation at 1.2 V for a period of 14 hours (light excluded, N_2 atmosphere), the sample became darker orange in color, thinner, and stiffer (Figure 2.2a-left; grid pattern caused by macroporous pressure cap). The presence of $FeCl_2$ in the electrolyte facilitates the oxidation step because, as per the design of the system, Fe^{2+} is weakly bound and will, therefore, rapidly equilibrate with the external solution. Figure 2.2d shows stress strain curves that were acquired by indentation testing of electrode-mounted samples after oxidation (left) and reduction (right). Chemical oxidation of Fe^{2+} samples by treatment with ammonium persulfate gave analogous physical and optical changes. EPEs with Fe^{2+} crosslinks also slowly oxidize in air over the course of hours to days, as shown by changes in color and stiffness of samples stored in humid environments to prevent drying.

2.2.4 Reversible electrochemical oxidation and reduction

The oxidation/reduction is reversible as can be seen in Figure 2.5a. The compressive moduli for a single EPEH sample that was subjected to two cycles of reduction and oxidation switch reversibly between ca. 1.0 MPa and 0.6 MPa. At each stage the samples displayed the color profile and degree of swelling that is characteristic of the particular oxidation state. Although the changes are reproducible and the moduli are clearly distinct, the difference in modulus range is smaller than that observed for samples directly prepared from Fe^{2+} and Fe^{3+}. We attribute the differences to a combination of two factors: 1) iron equilibration between the sample and electrolyte under experimental conditions and 2) air oxidation of reduced samples during sample transport and mechanical measurement.

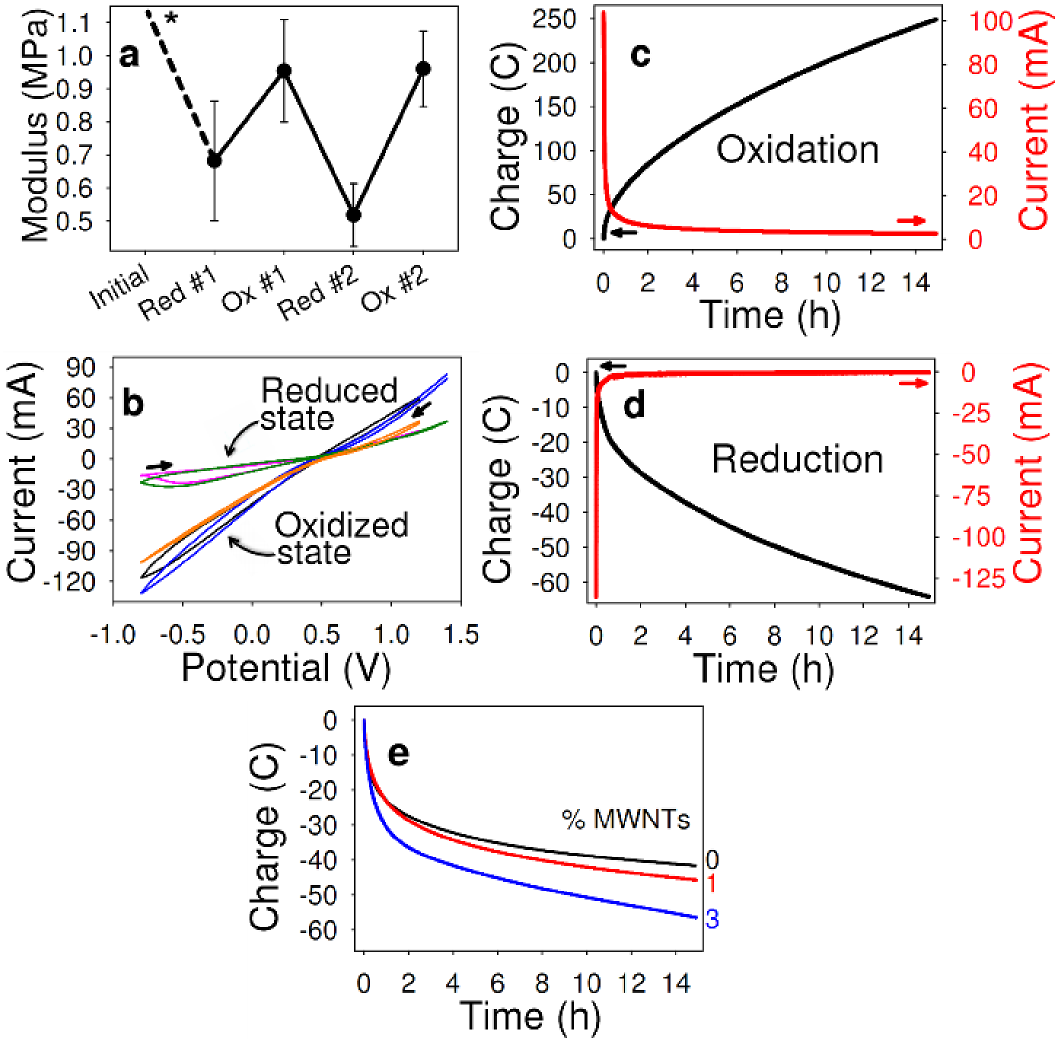

Figure 2.5 Mechanical and electrochemical characterization of redox-switched electroplastic elastomers. (a) Compressive moduli for oxidized and reduced samples. * Est. > 2 MPa. (b) Cyclic voltammograms before and after redox cycles. (c) & (d), Typical chronoamperometry and chronocoulometry for redox transitions. (e) Reduction of carbon-nanotube modified electroplastic elastomers. Improved charge transport for EPEH samples prepared with 0-3% by weight carbon nanotubes (MWNTs).

Figure 2.5 (b, c, & d) shows the electrochemical characteristics of the hydrogels used for these proof of concept experiments. In Figure 2.5b the cyclic voltammograms (CVs) acquired at each stable state represented in Figure 2.5a are plotted. The overlay demonstrates that the oxidized and reduced states are distinct and reproducible under cycling conditions. Example chronoamperometry and chronocoulometry plots (Figure 2.5c & d, see Figure A.1-A.4 for compilation of all data) establish that the redox process is slower than desired for applications. It should be noted that the total charge passed is much greater for the oxidation process because of the presence in the electrolyte solution of excess Fe^{2+}, which is maintained in constant excess within the system—not added or removed—for both the oxidation and reduction cycles.

Although the EPEs are new materials and have not been optimized, they already manifest a combination of features that suggest that they have an exceptional potential for further development and applications: scalability, reversibility, stability, tunability, and effective delivery of the stimulus. *Scalability is a key characteristic of the EPE materials.* Many intriguing nano- and subnanoscale phenomena have not successfully been translated into macroscale responses. By employing Nature's tactic of using multiple mediating steps it has been possible to translate an atomic scale phenomenon, metal-ion redox transformation, to a mechanical response that is readily observable on a macroscale. The coupling of the mediating steps was a non-trivial challenge, however, as it was necessary to create conditions in which all the relevant equilibria could operate in their functional regions. pH, for example, must be reasonably low to prevent the formation of insoluble metal oxidation products but maintained above the minimum threshold required for iron ions to compete effectively with protons for the carboxylate groups. Citrate ion, which facilitates iron mobility, is another necessary component of the system whose concentration must be strictly controlled because it assists some steps and hinders others. EPEs are also physically scalable. The hydrogels are prepared from non-exotic reagents and the same basic procedure is applicable to samples on larger scales—we have prepared samples with thicknesses up to 2.5 cm and length x width dimensions > 100 cm^2.

Reversibility and stability of the different states are also important features of the EPEs. The redox process cycles the metals between two states that are stable as long as the material is protected from environmental oxidants and reductants. The electrical power used to switch states is not necessary to maintain them. There is also no theoretical limit on the number of times that the electrochemical process can be repeated. It should be noted that the aqueous Fe^{2+} reservoir is an essential component since the uptake and exclusion of water and ions in the hydrogel is integral to the manifestation of oxidation-state dependent mechanical properties.

EPEs are highly tunable both in their preparation and in their implementation. By varying the percentage of carboxylate monomers or PEG-DA crosslinking agent relative to the other components, the fundamental stiffness can be adjusted within the limits of maintaining sample integrity and hindering ion migration. There is also the potential to adjust the stiffness through a full continuum of values within its range by partial redox.

The final characteristic of the system, delivery of stimulus, is still evolving. Although we have demonstrated that iron ions can be reduced and oxidized throughout the sample in the EPE hydrogels, the process is slow because the electrode is localized on one face. The chronocoloumetry data (Figure A.1-A.4) and direct observation suggest that the transformation is largely diffusion controlled (with possible contributions by electron exchange).[114] In a preliminary experiment, the effect of increasing the conductivity of the hydrogel on conversion time was probed. EPE samples prepared with the addition of 1-3% vinyl-functionalized multi-walled carbon nanotubes (MWNTs) were doped with Fe^{3+} and then subjected to reducing conditions. The charge vs. time response changed dramatically as shown in Figure 2.5e. The time to pass 40 Coulombs decreased from 11.9 h for hydrogel with no nanotubes to 3.2 h for 3%-MWNTs. Although the ratio of charge consumed by reduction of the nanotubes vs. Fe^{3+} under these conditions has not been determined, qualitative examination of the hydrogel color and behavior is consistent with a significant decrease in time for iron reduction. We hypothesize that the nanotubes improve conduction such that the distance that iron atoms must diffuse for reduction is decreased. These data are encouraging and suggest that conversions on the time-scale of minutes would be accessible with further refinements.

2.3 CONCLUSIONS

Throughout the history of design, the materials available to engineers have been predominantly fixed in their properties, with some exceptions mentioned above. EPEs represent the first of a novel class of materials that act in a self-contained system to change mechanical properties with electrical stimulus. The availability of materials of this type will potentially spawn new design paradigms that in turn lead to innovations in aerospace, manufacturing, consumer products, robotics, etc.

2.4 MATERIALS AND METHODS

All reagents were purchased from Sigma-Aldrich, unless otherwise noted, and were used as received. Poly(dimethylsiloxane) (PDMS) was commercially purchased locally, under the brand name GE Silicone II Kitchen & Bath. COOH-functionalized multi-walled carbon nanotubes (COOH-MWNTs, diameter: 8-15 nm, length: 10-50 μm, 2.56 % (w/w) functional content) were purchased from cheaptubes.com.

2.4.1 Typical hydrogel preparation

Sodium acrylate (4.8 g, 51 mmol) and sodium (4-styrene sulfonate) (3.2 g, 14.3 mmol) were combined with 36 mL of deionized water and gently heated (< 40 °C) until all solids were dissolved. Poly(ethylene glycol) diacrylate, (PEG-DA, $M_n = 575$, 400 μL, 0.78 mmol) was added and the mixture was purged with N_2 for 5 min. Ammonium persulfate (APS, 72 mg, 0.47 mol%) was added as a radical initiator for copolymerization. Note: adjustments in PEG-DA stoichiometry relative to the other monomers produced hydrogels that were qualitatively stiffer (increased PEG-DA) or softer (decreased PEG-DA).

2.4.2 Iron doping

Depending on the dimensions of the sample being prepared, 2 to 8 mL of the reaction mixture was pipetted into a mold. For electrochemical experiments the mold for the sample was created by temporarily affixing, using PDMS adhesive, a square glass cell to a Teflon base bearing a freshly polished glassy carbon electrode (GCE). The mold/sample combination was then heated at 85 °C for 1.5 h. After cooling to RT, the hydrogel was doped by simple submersion in either a solution of 2.0 M $FeCl_2$/0.5 M citric acid or 2.0 M $FeCl_3$/0.5 M citric acid for a period of 20-48 h (Figure 2.3). A 1:3 ratio by volume of doping solution to pre-polymer was used.

2.4.3 Incorporation of vinyl-functionalized MWNTs

Vinyl-functionalized MWNTs were synthesized as reported in the literature[115] from commercially purchased COOH-MWNTs. Prior to hydrogel polymerization MWNTs were suspended in DI-water and dispersed in an ultrasonic water bath for 30 min. The dispersed MWNTs were then added to the dissolved monomers (mixed in the same ratio as for simple hydrogels) and APS was added as a radical initiator. Polymerization and iron doping was performed as described above.

2.4.4 Mössbauer spectroscopy

The ^{57}Fe Mössbauer spectra were collected on constant acceleration instruments over the temperature range of 4.2-300 K in zero or 0.045 T applied fields. Samples were prepared by adding minced hydrogel (1-5 mm^2 pieces) to Teflon Mössbauer cups covered with lids. Spectral simulations were generated using WMOSS (WEB Research, Edina, MN). Isomer shifts are reported relative to Fe metal foil at room temperature.

The room temperature Mössbauer spectrum of a sample of the Fe^{3+}-doped hydrogel showed one quadrupole doublet with an isomer shift of $\delta = 0.41$ mm/s and a quadrupole splitting of $\Delta E_Q = 0.53$ mm/s. These Mössbauer parameters confirm the presence in the hydrogel of high-spin Fe^{3+}. They are also similar to Mössbauer parameters of high-spin Fe^{3+} ions in oxalates (δ between 0.35 mm/s and 0.41 mm/s and ΔE_Q between 0.38 mm/s and 0.75 mm/s).[116-119]

The 4.2-K Mössbauer spectrum of a similar sample of the iron-doped hydrogel that was electrochemically reduced to Fe^{2+} showed a quadrupole doublet with $\delta = 1.37$ mm/s and $\Delta E_Q = 3.26$ mm/s, which represents 85% of the iron in the sample. These parameters are typical of high-spin Fe^{2+} and are comparable, although at the high end, of the Mössbauer parameters of Fe^{2+} in oxalates.[116-119] This result confirms the efficiency of the reduction protocol. A small shoulder on the right side of the left line of the Fe^{2+} quadrupole doublet indicates the presence in the sample of a small amount of high-spin Fe^{3+}. Note: spectrum collected at low temperature to inhibit oxidation during data collection.

2.4.5 Mechanical measurements

The mechanical testing procedure, specifically developed for the case of testing thin EPE materials, was based on an indentation testing methodology.[120] A circular cylindrical indentation probe (diameter 6.2 mm) was fashioned to screw into the crosshead of an MTI-1K screw driven, table top load frame. A 10N Transducer Techniques load cell was employed to measure the force exerted on the EPE specimen by the indentation probe. Owing to the thin nature of the specimens tested (< 10 mm), as well as the small range of expected loading, the strain was calculated from the crosshead displacement as opposed to using an external extensometer. Additional experimental parameters such as strain rate and total strain were determined by referring to ASTM D1621-04A Standard Test Method for Compressive Properties of Rigid Cellular Plastics. Each indentation test yielded a single stress-strain curve, which contributed a single stiffness measurement (Young's modulus). In total, five indentation tests were performed on each 2.5 x 2.5 x 0.2 cm sample (one in each corner, and one in the center of the sample) and the mean value was reported. Per the standard, Young's modulus is measured by taking the slope of the linear portion of the curve.

2.4.6 Electrochemical methods

Cyclic voltammetry (CV) and amperometry measurements were carried out with a CH Instruments Electrochemical work station Model 430A (Austin, TX) at RT using a three-electrode system composed of a glassy carbon plate (GCE, 25 x 25 mm) working electrode, a Ag/AgCl reference electrode, and a platinum grid counter electrode (Figure 2.4). The GCE was polished with 0.3 µm Al_2O_3 paste and cleaned thoroughly in an ultrasonic water bath for 5 min prior to each use. The CV and amperometry experiments for reduction and oxidation were carried out in 15 mL of 2.0 M

$FeCl_2$/0.25 M citric acid, pH ~1.8. CV data were acquired at a scan rate of 100 mV/s over a voltage range of 1.2 to -0.8 V. Bulk electrolysis was performed in the same electrolyte solution for up to 40 h (reduction potential -0.8 V, oxidation potential +1.2 V). All electrochemical experiments were performed under N_2 atmosphere with careful exclusion of ambient light to prevent the photoreduction of Fe^{3+} ions in the presence of citric acid.[37]

2.4.7 Control experiments

Bulk electrochemical reduction at -0.8 V of Fe^{3+}-hydrogel in 15 mL of KNO_3 (0.2 M, adjusted to pH 1) electrolyte was performed for 16 h. Sample exhibited properties analogous to reductions performed under standard conditions (15 mL of 2 M $FeCl_2$/0.25 M citric acid, pH ~1.8, 16-20 h).

Fe^{3+}-hydrogel samples showed negligible leaching of Fe^{3+} when soaked in 15 mL of KNO_3 (0.2 M, adjusted to pH 1) over similar time periods without applied reduction potential. Fe^{2+}-samples showed dramatic leaching into the electrolyte under similar conditions.

Fe^{3+}-hydrogel samples showed negligible exchange when soaked in 15 mL of 2 M $FeCl_2$/0.25 M citric acid, pH ~1.8. The material retained both color and stiffness over periods >20 h.

A Fe^{2+}-doped sample was treated with 2M APS by a combination of submersion (< 1 hour) and intra-gel injection. The sample rapidly became dark-orange in color, smaller in dimension and qualitatively stiffer.

A Fe^{2+}-doped sample was exposed to atmospheric conditions in a closed container under moisture conditions (reservoir of free water, covered with damp towel) known to prevent sample dehydration. The sample became progressively orange in color and stiffer over a period of hours.

Consistent with increased Fe^{3+} crosslinking, some water loss from the gel occurs during this period, as indicated by sample shrinkage.

2.4.8 Chronoamperometry and chronocoulometry for redox cycling of Fe3+ hydrogel

The sample used for the redox cycling was initially doped for 47 h to yield an ~2 mm thick Fe^{3+} hydrogel. Due to a technical difficulty, the first reduction segment took place over 3 experiments totaling 80 h. The last segment is shown in Figure A.1. Redox cycles following the first reduction were carried out for 15-18 h and are shown in Figure A.1-A.4.

2.4.9 Quantification of iron

The method for quantifying the amount of iron in the EPEHs was based on the quantitative methods reported by both Viollier[121] and Peng[37]. 1,10-phenanthroline was the reagent used to bind Fe^{2+}. One variation from the two cited methods was the use of concentrated HCl to break down EPEH's in order to extract the iron contained within the gels. $FeCl_2$ standards (0.025 M) were prepared in concentrated HCl and diluted in sodium acetate buffer (0.1 M, pH=4). A Lambda 9 (Perkin-Elmer) UV/Vis/NIR spectrometer was used to create a calibration curve (Figure A.5).

Iron-doped hydrogels were digested for 2 h using concentrated HCl (5 mL HCl per 1 mL pre-polymer volume). Two 100 µL aliquots from the HCl-degraded hydrogel were diluted in parallel in sodium acetate buffer (0.1 M, pH=4) so that the absorbance was in the linear range of the instrument (10 mL final volume, denoted Samples A and B). To determine the Fe^{2+} content, a solution of 1,10-phenanthroline in water (2 mL, 0.0055 M) was added to Sample A and the absorbance was measured. To determine the total Fe content, Sample B was treated with an excess of the chemical reductant hydroxylamine·HCl (1.5 mL, 1.4 M in water). After reacting for 10 min a solution of 1,10-phenanthroline (2 mL, 0.0055 M) was added and the absorbance was measured. Fe^{3+} was determined by difference.

2.4.10 Mechanical properties of Fe2+ and Fe3+ doped hydrogels and Fe:carboxylate ratio

Mechanical measurements and quantitative analysis were carried out on Fe^{2+}- and Fe^{3+} -doped EPEs (ca. 2.5 x 2.5 x 0.3 mm after doping) that were prepared in parallel and the results are summarized in Table 2.1. The $FeCl_2$- and $FeCl_3$-doped hydrogels contained approximately the same amounts of total iron. When the parallel samples were mechanically tested an ~36-fold difference was observed between their moduli. The iron to carboxylate ratio was calculated assuming complete SA copolymerization (4 mL pre-polymer). It is important to note that the only difference between these samples is the oxidation state of the iron.

3.0 CHEMICAL AND ELECTROCHEMICAL MANIPULATION OF MECHANICAL PROPERTIES IN STIMULI-RESPONSIVE COPPER-CROSSLINKED HYDROGELS

(Portions of this work were published previously and are reprinted with permission from Harris, R. D.; Auletta, J. T.; Motlagh, S. A. M.; Lawless, M. J.; Perri, N. M.; Saxena, S.; Weiland, L. M.; Waldeck, D. H.; Clark, W. W.; Meyer, T. Y. *ACS Macro Letters*, **2013**, 2 (12), 1095-1099. Copyright 2013 American Chemical Society.)

This work was performed in collaboration with Rachel Harris and Nicholas Perri from the Meyer group. Mechanical characterization was carried out with help from Dr. Amin Motlagh from the Clark group. Matthew Lawless from the Saxena group performed and interpreted EPR spectra.

3.1 INTRODUCTION

Stimuli-responsive materials that exhibit significant property changes when exposed to an external trigger provide new approaches to challenges in diverse areas including energy, sensing, health, chemical synthesis, construction, and electronics.[97, 122-124] Polymers can be engineered to respond to specific stimuli including temperature, light, pH, ion concentration, chemical structure of additives, magnetic field, mechanical forces, and electricity and can respond with changes in dimension, shape, viscosity, healing, release of guest species, fluorescence, conductivity, permeability and mechanical properties.[28, 59-60, 93, 95-96, 100, 125-127] Moreover, as with natural materials, synthetic polymers can be designed to respond to multiple stimuli by producing either a unified response or a repertoire of stimuli-specific responses. These multi-responsive materials allow for greater flexibility in material design and a wider range of functionality and applications.[99, 128]

We are interested in exploring the use of redox stimuli to introduce changes in mechanical properties and shape.[129] Oxidation state is a powerful tool for manipulating metal-containing materials and a variety of responses have been shown to depend on metal oxidation state.[37-38, 43, 60, 108, 126, 130-131] Copper, which exhibits redox-state preferences in coordination number, geometry, and ligand type, has been exploited in the design of responsive molecules and materials.[43-45, 132-134]

Herein, we describe a new copper-based metallopolymer, an electroplastic elastomer (EPE), that is dual-responsive, undergoing both electrochemically and chemically-stimulated transitions between hard and soft states. Analogous to the Fe^{2+}/Fe^{3+} EPE that we reported previously, the Cu-EPE has two crosslinking systems: a stable, covalent system that maintains the hydrogel's basic shape and a dynamic system based on the coordination of side-groups to metal ions. This new copper system uses redox-specific coordination with hydrophobic pyridine groups to access higher moduli and larger differences in hard and soft moduli than those observed in the carboxylate-based iron system (Figure 3.1). Additionally, the unique redox characteristics of copper facilitate the demonstration of shape memory.

3.2 RESULTS AND DISCUSSION

The basic hydrogel was prepared by simple free-radical copolymerization of commercially purchased monomers. Sodium (4-styrene sulfonate), 4-vinylpyridine, and poly(ethylene glycol) diacrylate (PEG-DA, M_n = 575) in a weight ratio of 16:4:1 were reacted in aqueous solution with an ammonium persulfate catalyst at 85 °C for 1.5 hours to give a soft, pale yellow hydrogel. The presence of the permanent PEG-DA crosslinks gives the hydrogels a baseline shape defined by the reaction vessel.

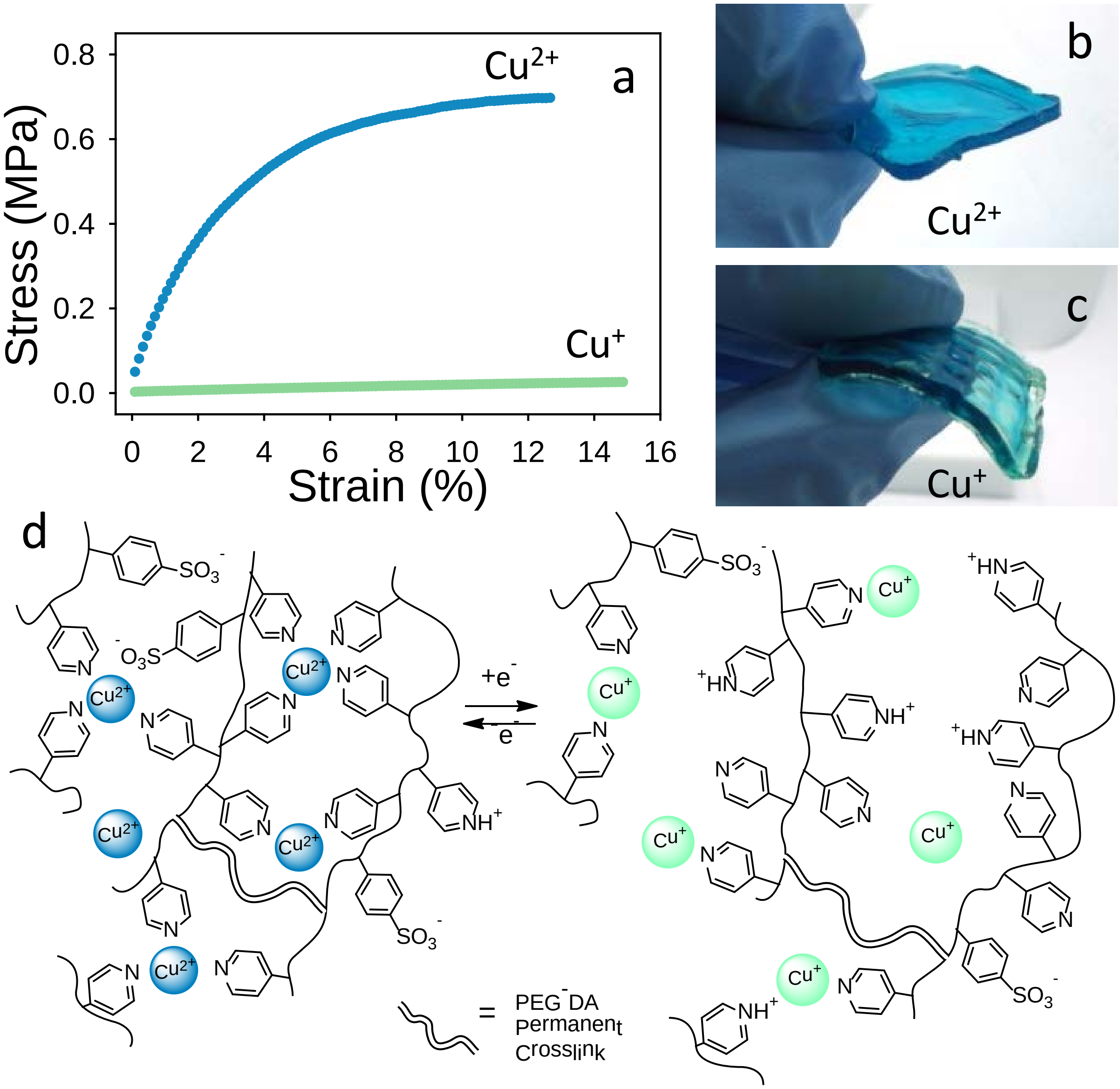

Figure 3.1 (a) Indentation modulus measurements of a sample at various stages of electrochemical cycling (Red = reduction, Ox = oxidation). Multiple moduli are a result of sample inhomogeneity as measured with an indentation probe. (b) Current vs. potential graphs showing oxidation and reduction peaks of the copper ion. (c), (d) Chronocoulometry and chronoamperometry for the oxidation and reduction processes.

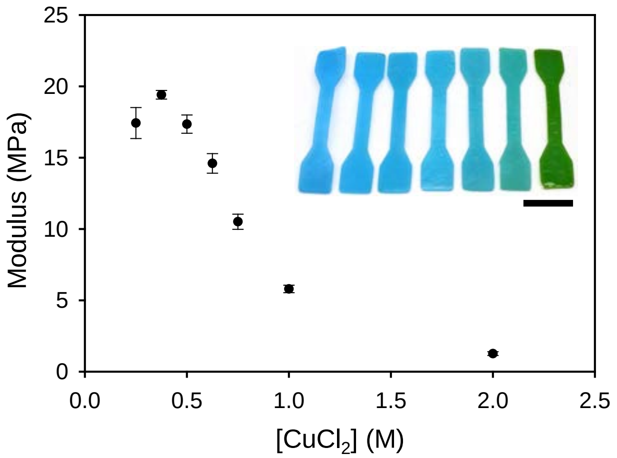

Figure 3.2 Dependence of mechanical stiffness on the concentration of copper in the doping solution (incl. 0.025 M urea). Inset shows dumbbell samples used for tensile testing. From left to right increasing copper concentration, scale bar 10 mm.

The Cu^{2+} hydrogel was produced by submersion of the undoped hydrogel in a solution of 0.5 M $CuCl_2$/0.025 M urea for a period of 20-48 hours. Qualitatively, the samples were bright blue in color, tougher, and stiffer than the original hydrogel. Consistent with the formation of metal-mediated crosslinks, the sample volume decreased with a concomitant loss of ~19% of the water content during this process (Table 3.1). Urea was used as a component of the metal solution in order to promote homogeneous doping by acting as a competitive ligand with the side-chain pyridine; use of pure $CuCl_2$ solutions gave samples with a hard shell and a soft interior because fast crosslinking of the exterior inhibits ion diffusion to the interior. The mechanical properties of the Cu^{2+}-EPE depended on the concentration of the dopant solution. The highest modulus, as determined by tensile testing, was obtained with a doping solution of 0.375 M $CuCl_2$/0.025 M urea (Figure 3.2). Both a deficiency of copper and an excess would be expected to decrease the crosslink density as too few ions should give high pyridine coordination numbers, e.g., $(py)_4Cu$ but a low number of crosslink points whereas a high concentration of copper would be expected to give a high number of potential crosslink sites but low pyridine coordination numbers, e.g. $(py)(OH_2)CuCl_2$. Supporting this interpretation is the change in absorption frequency with increasing copper from the blue (λ_{max} = 690 nm) color associated with donor ligands to the green color (λ_{max} = 840 nm) associated with chloride ligands (Figure 3.3 and Figure 3.4).

Table 3.1 Water content of Cu^+- and Cu^{2+} - doped hydrogels.

Sample Condition	Water Content (% by mass)
Undoped gel	76%
Cu (I)-doped	78%
Cu (II)-doped	57%
Cu (I)-doped; air oxidized to Cu(II)	69%

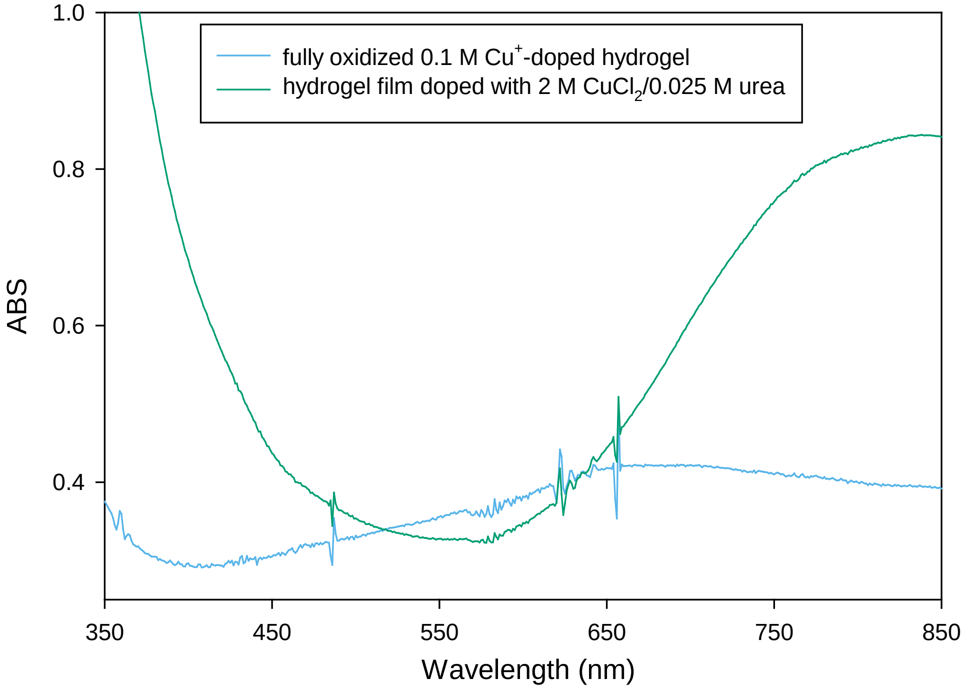

Figure 3.3 UV-Vis absorption spectra of fully oxidized Cu^+-doped hydrogel (blue) and hydrogel doped with 2 M $CuCl_2$/0.025 M urea (green).

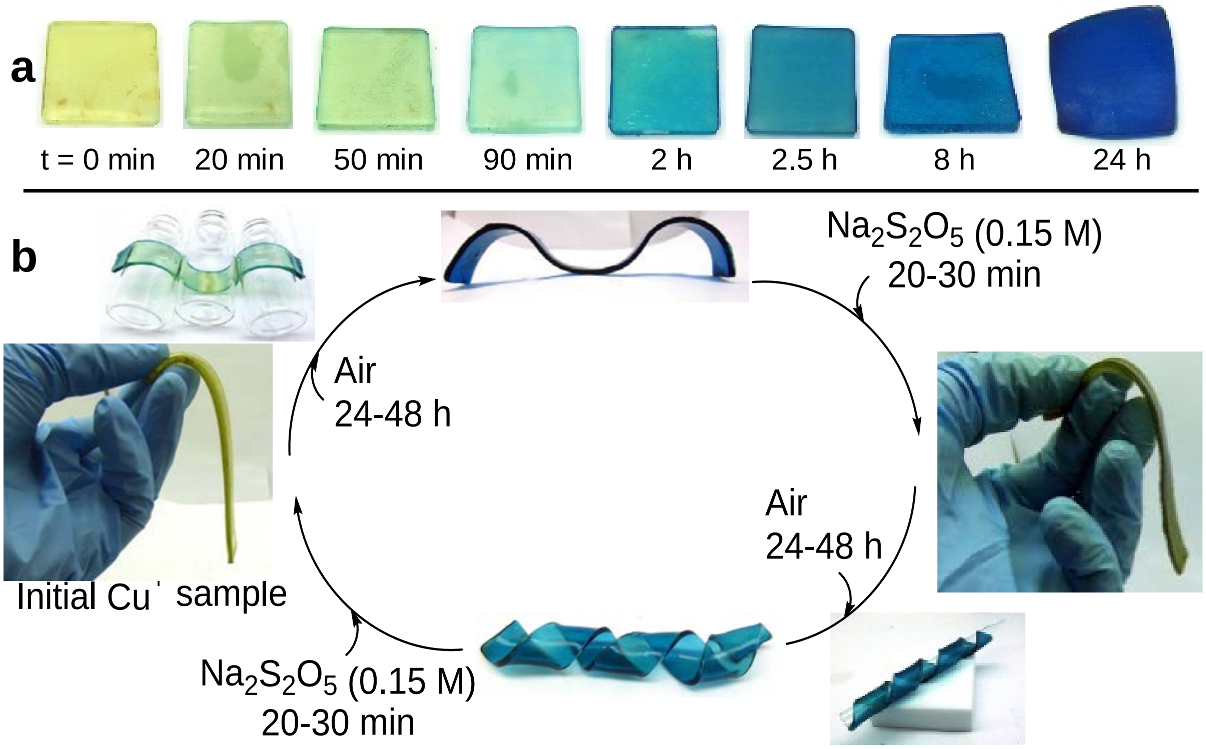

Figure 3.4 (a) Conversion of Cu^+-doped hydrogel to Cu^{2+} in air. (b) Demonstration of shape memory for copper-crosslinked hydrogels.

Both ESR and quantitative analysis of samples prepared with our standard doping concentration of 0.5 M $CuCl_2$ suggest that the copper coordination sphere contains both nitrogen (pyridine) and oxygen ligands (water/sulfonate). Specifically, ESR spectroscopy was consistent with four equatorial ligands, i.e., type II coordination with a 3N1O or 2N2O ligand distribution (Figure 3.5 and Figure 3.6) with possible contributions from axial ligands, most likely water in this case. Quantitative analysis of the copper in a sample at the 0.5 M CuCl2 level () gave a ratio of copper to pyridine of ca. 2.5:4 which is consistent with the mixed nitrogen/oxygen coordination determined by ESR spectroscopy. Access to higher pyridine coordination numbers is likely inhibited both by the presence of sulfonate groups as well as accessibility limitations arising from the connection of the coordinating ligands to the polymer backbone. It should be noted that although the urea co-dopant may also act as a ligand, the relatively low concentrations and weak binding strength should minimize any contribution.

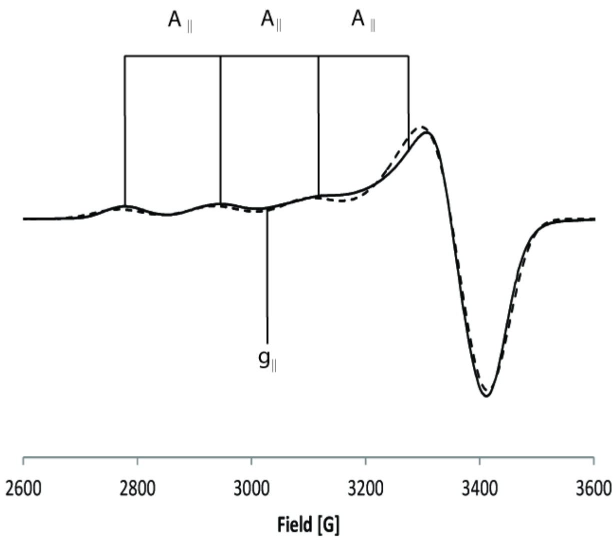

Figure 3.5 Experimental (solid black line) and simulated (dashed black line) CW spectrum of a 0.025 M Cu^{2+} hydrogel. Figure prepared by Matthew Lawless.

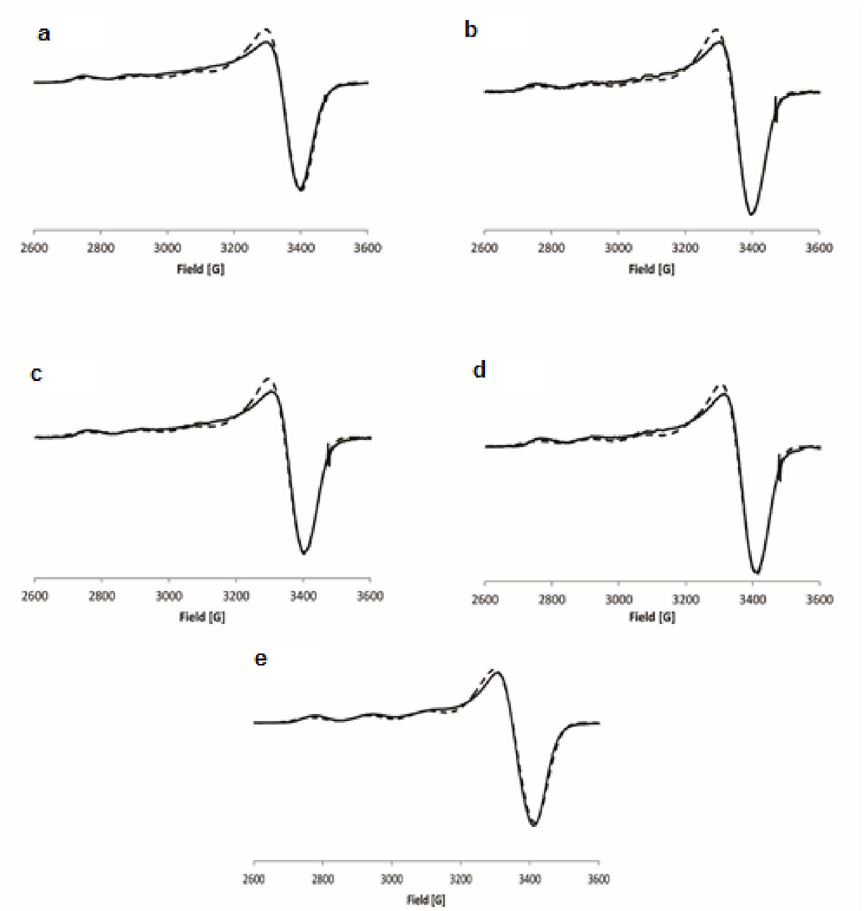

Figure 3.6 Experimental (solid black line) and simulated (dashed black line) CW spectra are shown. (a) 2.0 M Cu^{2+} hydrogel with $g_{\parallel}$=2.3125 $A_{\parallel}$= 158 G, (b) 0.75 M Cu^{2+} hydrogel with $g_{\parallel}$=2.3125 $A_{\parallel}$= 158, (c) 0.50 M Cu^{2+} hydrogel with $g_{\parallel}$=2.3125 $A_{\parallel}$= 158, (d) 0.25 M Cu^{2+} hydrogel with $g_{\parallel}$=2.3125 $A_{\parallel}$= 156.5 G and (e) 0.025 M Cu^{2+} hydrogel with $g_{\parallel}$=2.3000 $A_{\parallel}$= 165. Figure prepared by Matthew Lawless.

Table 3.2 Copper quantification results. Quantity of 4-vinylpyridine (VP) was assumed to be constant at 0.845 mmol, calculated from the mass of VP added to the hydrogel solution and assuming complete polymerization.

Dopant	mmol Cu	Cu : VP ratio
0.1 M CuCl*	0.289	1.4:4
0.5 M $CuCl_2$*	0.530	2.5:4
0.25 M $CuCl_2$	0.329	1.6:4
0.1 M $CuCl_2$	0.321	1.5:4

*Conditions reported in Materials and Methods

The softer Cu^+-EPEH was prepared by submersion of the hydrogel in a solution of 0.1 M CuCl/0.5 M NH_4OH in water or 0.1 M CuCl in acetonitrile for 24-48 hours under nitrogen. If the sample was to be handled in air after preparation, the copper could be stabilized in the +1 state by the addition of sodium metabisulfite to the doping solution. The poor solubility of copper (I) salts precluded the use of more concentrated solutions. Qualitatively, the Cu^+-doped hydrogels were pale yellow in color, modestly stiffer, and much tougher than the undoped gel. Water content decreased by a negligible amount during this doping process (Table 3.1), which was consistent with weak coordination between the Cu^+ ions and the pyridine ligands.

The Cu^{2+}-doped EPEHs exhibited significantly higher moduli than those observed for the iron system that we described previously.[129] Moduli obtained by indentation testing[135] ranged from 3.1-3.5 MPa, while those obtained using tensile measurements were as high as 10-18 MPa (Table 3.3). Indentation testing of Cu^+-doped EPEHs gave much lower moduli than those of Cu^{2+}, in the 0.29-0.73 MPa range (0.15-0.16 MPa, tensile). Moduli measured for comparable iron samples were 0.06 for Fe^{2+} and 2.1 MPa for Fe^{3+} by indentation.[129] It should be noted that the indentation testing method employed, which is easier to administer to samples that were not specifically prepared for mechanical testing, produces measurements that are useful for qualitative comparisons but not as accurate in our case as those acquired by tensile testing. Schubert and coworkers,[136] have reported previously that indentation tests present numerous challenges both in acquisition of accurate measurements and in the relationship of these measurements to those acquired by other methods.

Table 3.3 Mechanical properties of typical Cu^+- and Cu^{2+}-doped hydrogels.

Dopant	Ave Compressive Modulus (MPa)[a]	Compressive Modulus Range (MPa)[a]	Average Tensile Modulus (MPa)[b]	Tensile Modulus Range (MPa)[b]
0.1 M CuCl	0.46	0.29-0.73	0.16	0.15-0.16
0.5 M $CuCl_2$	3.3	3.1-3.5	13	10-18

[a]Determined by indentation method on a sample measuring 2.5 x 2.5 x 0.2 cm. [b] Determined by elongation of thick films measuring ca 9-10 x 1.5-2 x 0.1-0.2 cm.

The sample could be switched from the hard to soft state electrochemically (Figure 3.7, Figure B.1). Reduction of Cu^{2+} to Cu^+ was accomplished by the application of a -0.2 V potential (vs. Ag/AgCl) to the sample on a glassy carbon electrode in an electrolyte comprising 0.067 M KNO_3 in water saturated with acetonitrile (ca. 1:3). The extent of reduction could be monitored visually by the change in color from dark blue to lighter green-blue (Figure 3.1b and c). Indentation moduli measurements revealed a greater than one order of magnitude difference between the Cu^{2+}-doped state at 3.0 MPa and the reduced state at 0.11 MPa. In simple aqueous electrolyte, over reduction led to the formation of copper metal particles (Figure 3.8). Use of a mixed acetonitrile/water solution appears to prevent this problem. Cyclic voltammograms (CVs) of the gels in the oxidized and reduced states are distinct (Figure 3.7b, c, and d).

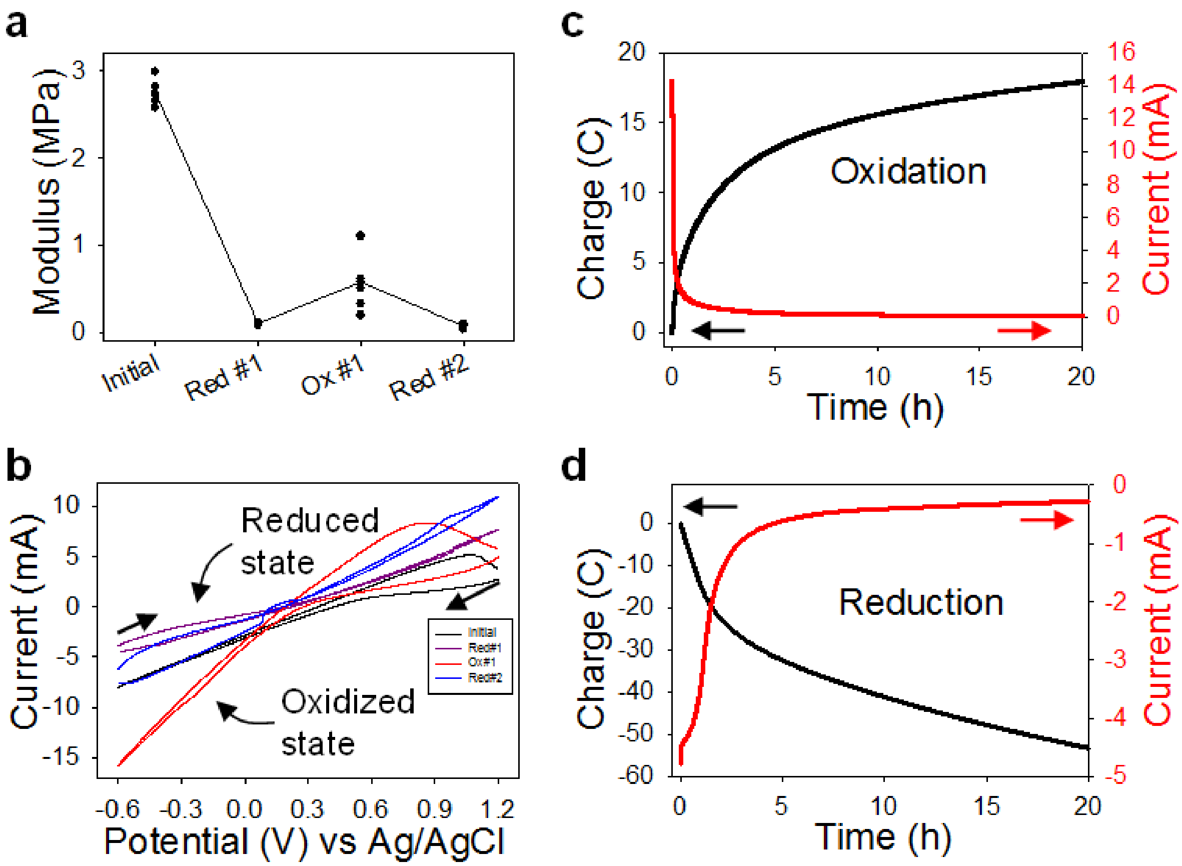

Figure 3.7 (a) Indentation modulus measurements of a sample at various stages of electrochemical cycling (Red = reduction, Ox = oxidation). Multiple moduli are a result of sample inhomogeneity as measured with an indentation probe. (b) Current vs. potential graphs showing oxidation and reduction peaks of the copper ion. (c), (d) Chronocoulometry and chronoamperometry for the oxidation and reduction processes.

Figure 3.8 A Cu^{2+}-doped hydrogel, after electrochemical reduction for 30 hours at -0.2 V in 0.1M KNO_3/0.1 M urea aqueous electrolyte shows over-reduction to Cu^0, likely due to the presence of Cu ions in the electrolyte.

The electrochemical oxidation of a freshly prepared Cu^+-gel to Cu^{2+} could be partially achieved by applying a +1.0 V potential to a Cu^+-doped hydrogel in 0.1 M CuCl (stabilized by sodium metabisulfite) in water saturated with acetonitrile. As shown in Figure 3.7a, the oxidation does not return the sample to the original level of stiffness and the sample is not homogeneous. Re-reduction, however, does give a hydrogel with a modulus similar to that observed after the first reduction. The electrochemical oxidation step appeared to be hindered by the formation of a hard Cu^{2+}-crosslinked shell on the hydrogel face that was in direct contact with the electrode (Figure 3.9). We hypothesize that the Cu^{2+}-shell was poorly permeable and inhibited the ion migration necessary for bulk oxidation. Also consistent with this observation was the relatively low amount of charge passed during the oxidation process.

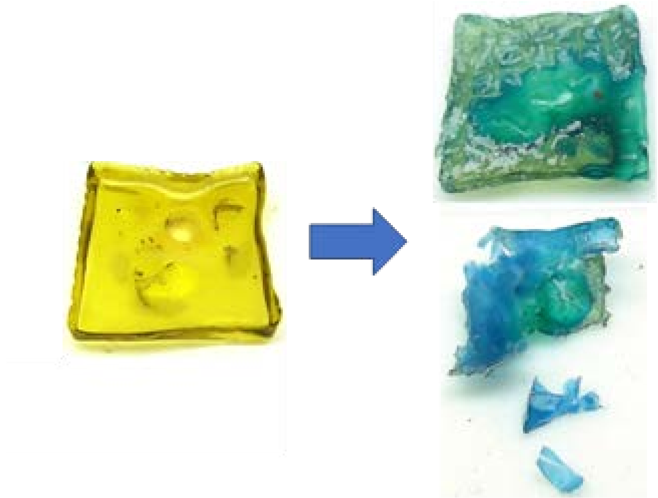

Figure 3.9 Partial electrochemical oxidation of a Cu^+ gel to a Cu^{2+} gel. The scraps of blue hydrogel are the impermeable shell that forms on the electrode during oxidation, separating from the rest of the bulk sample upon removal from the electrode.

Completely reversible switching between hard and soft states could be accomplished using chemical stimuli. Oxidation from Cu^+ to Cu^{2+}, which was challenging electrochemically, occurs through simple exposure to ambient oxygen (Figure 3.4). The sample rapidly changes color and becomes stiffer. UV-Vis spectra of films undergoing this oxidation process show a gradual conversion from the Cu^+ state which absorbs only weakly in the visible to the blue absorption (λ_{max} = 690 nm) associated with the Cu^{2+} crosslinks (Figure 3.10). Samples that were “shaped” prior to oxidation maintained the new shape after the transition. In contrast, samples doped with Cu^{2+} remained stable to air and retained their color, shape, and mechanical properties. The water content decreased by 12% during the air oxidation from Cu^+ to Cu^{2+} (Table 3.1). This decrease in water was not caused by sample drying—hydration was maintained during oxidation—but rather to the increased binding of Cu^{2+} to the polymer chains. Chemical reduction was also facile. Submersion of the stiffer Cu^{2+} samples in a solution of 0.15 M sodium metabisulfite gave a flexible, Cu^+ hydrogel in minutes.

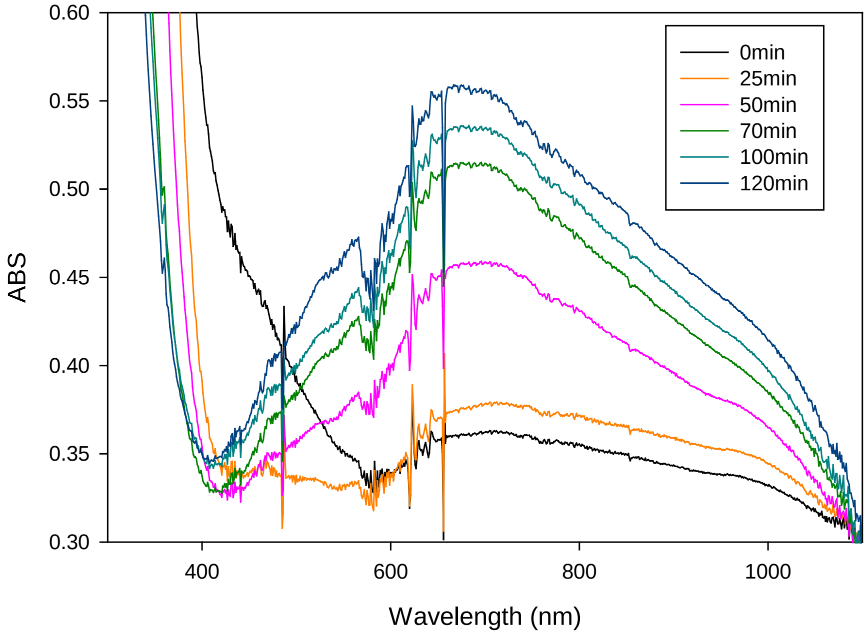

Figure 3.10 UV-Vis absorption spectra of Cu^+-doped hydrogel oxidized in air over 120 min.

The copper hydrogel materials also possess shape memory characteristics. A sample prepared in the +1 oxidation state, for example, was molded to form a flat, flexible strip (Figure 3.4). If the sample was then formed into a shape and allowed to air oxidize, the new stiffer Cu^{2+}-EPEH held the new profile. Reduction of the sample by immersion in a solution of sodium metabisulfite regenerated the original flat, flexible form, which could be recast into a new profile and hardened by oxidation. The cycle is repeatable, although recharging of the copper ions is necessary after several cycles as the poorly bound Cu^+ is prone to leaching. The fundamental shape of the hydrogel (2-3 mm thick rectangular prism) is determined by the original network formed with the non-reversible PEG-DA crosslinks. The secondary network that allows the material to hold a second shape is formed by the oxidized Cu^{2+} ions which crosslink the chains by coordination with pyridine. Reduction to Cu^{+} destroys the secondary network and restores the original shape.

3.3 CONCLUSIONS

The creation of a stable hydrogel system that selectively coordinates more strongly to copper in the +2 oxidation state than in the +1 oxidation state has been accomplished. The material properties of hydrogels containing Cu^{2+} are significantly different from those of hydrogels containing Cu^{+}. Cu^{2+}-containing hydrogels are bright blue and rigid, whereas hydrogels containing Cu^{+} are light yellow, soft, and pliable. The EPE material can reversibly transition between these two states using chemical stimuli and unidirectionally using electrochemistry. These Cu-based EPEs offer a multiresponsive paradigm for a self-contained, three-dimensional stimuli-responsive material that undergoes changes in mechanical properties.

3.4 MATERIALS AND METHODS

All reagents were purchased from Sigma-Aldrich, unless otherwise noted, and were used as received. Poly(dimethylsiloxane) was from GE Brand (GE Silicone II Kitchen & Bath).

3.4.1 Typical hydrogel preparation

Sodium (4-styrene sulfonate) (SS, 1.6g, 7.77 mmol), 4-vinylpyridine (VP, 0.41 mL, 3.80 mmol), and poly(ethylene glycol) diacrylate, (PEG-DA, M_n = 575, 100 µL, 0.194 mmol) were combined with 9 mL of deionized water and gently heated (< 40 °C) until all solids were dissolved. The mixture was purged with N_2 for 1 min. Ammonium persulfate (APS, 60 mg, 2.2 mol%) was added as radical initiator for copolymerization.

The reaction mixture was pipetted into a mold (Figure B.2 and Figure B.3). Typical sample dimensions were 2.5 x 2.5 x 0.3 cm. For electrochemical experiments the mold for the sample was created by temporarily affixing a square glass cell using poly(dimethylsiloxane) (PDMS) adhesive to a Teflon base bearing a freshly polished glassy carbon electrode (GCE). The mold/sample combination was then heated at 85°C for 1.5 h. After cooling to RT, the hydrogel was doped by simple submersion in aqueous 0.5 M $CuCl_2$/ 0.025 M urea solution. Samples were doped with 5 mL copper solution for every 2 mL hydrogel solution. For a typical doping solution, $CuCl_2$ (0.34 g, 2.5 mmol) and urea (0.008 g, 0.13 mmol) were combined with 5 mL deionized water and stirred until all solids were dissolved. Both sample and solution were covered and allowed to sit overnight.

3.4.1.1 Preparation of large PSS/PVP samples for shape memory and tensile testing

For a typical 12 mL hydrogel, sodium 4-styrenesulfonate (SS, 4.3 g, 20.6 mmol), 4-vinylpyridine (VP, 1.1 mL, 10.1 mmol), and poly(ethyleneglycol) diacrylate (PEG-DA, M_n = 575, 267 µL, 0.464 mmol) were combined with 24 mL of deionized water and gently heated to below 40 °C until all solids were dissolved. The mixture was purged with N_2 for 3 min. APS (160 mg, 2.2 mol%) was added as radical initiator for copolymerization. Aliquots (12 mL each) of the hydrogel solution were pipetted into two 5.0 cm x 12.5 cm Teflon wells. The samples were covered with aluminum foil and then heated at 85 °C for 1.5 h. The samples were then allowed to cool to room temperature over a period of several minutes. Samples were doped overnight with 0.5 M $CuCl_2$/0.025 M urea or 0.1 M CuCl/0.5 M NH_4OH/0.25 M sodium meta-bisulfite.

3.4.1.2 Preparation of large PSS/PVP samples for tensile testing (sheets)

Sodium (4-styrene sulfonate) (SS, 9.6 g, 42.8 mmol), 4-vinylpyridine (VP, 2.46 mL, 22.8 mmol), and poly(ethylene glycol) diacrylate, (PEG-DA, M_n = 575, 600 µL, 1.17 mmol) were combined with 54 mL of deionized water and gently heated (< 40 °C) until all solids were dissolved. The mixture was purged with N_2 for 15 min and 1200 µL of 300 mg/mL ammonium persulfate solution (APS, 360 mg, 2.2 mol%) was added as radical initiator for copolymerization. To prepare hydrogel sheets, 5 mL aliquots were transferred to glass molds (1 mm x 8.3 mm x 7.3 mm), covered with aluminum foil and placed in an oven at 85 °C for 1.5 h. The gels were cooled to RT, carefully removed from the molds and doped for 36 h using 12.5 mL of dopant solution per sample with increasing [$CuCl_2$] at 0.25, 0.375, 0.5, 0.625, 0.75, 1.0, and 2.0 M $CuCl_2$ with 0.025 M urea held constant throughout.

3.4.1.3 Hydrogel film preparation for UV-Vis measurements

Sodium (4-styrene sulfonate) (SS, 0.3556 g, 1.73 mmol), 4-vinylpyridine (VP, 91 µL, 0.85 mmol), and poly(ethylene glycol) diacrylate, (PEG-DA, Mn = 575, 22 µL, 0.043 mmol) were combined with 2 mL of deionized water and gently heated (< 40 °C) until all solids were dissolved. The mixture was purged with N_2 for 15 min. Ammonium persulfate aqueous solution (APS, 44 µL of 300 mg/mL, 13.2 mg, 2.2 mol%) was added as radical initiator for copolymerization. A hydrogel film was cast by sandwiching the monomer mixture between two glass plates using ≈120 µm spacers (Final size: 80 x 70 x 0.12 mm) and polymerizing in an oven at 85 °C for 1.5h. After cooling, the film was carefully removed and placed in 5 mL of freshly prepared dopant comprised of 0.1 M CuCl, 0.5 M NH_4OH, and 0.25 M $Na_2S_2O_5$ (sodium metabisulfite) and kept under N_2 for 15 min. The sample was removed from the dopant and a slice of Cu(I)-doped hydrogel was cut from the bulk film (≈5 mm x ≈30 mm) and placed on the side of a halved polystyrene cuvette. The UV-Vis spectrum of the hydrogel was recorded over time as shown in Figure 3.10. Between scans the hydrogel film was kept in a petri dish with a moist paper towel to prevent the sample from dehydrating.

3.4.2 Electrochemical measurements

Cyclic voltammetry (CV) and amperometric i-t curve measurements were carried out with a CH Instruments Electrochemical work station 430A Model (Austin, TX) at room temperature using a three-electrode system, composed of a glassy carbon (GC) plate (25 x 25 mm) coated with a copper-hydrogel film of 2 mm thickness as working electrode, a Ag/AgCl reference electrode and a platinum grid as counter electrode. The GC plate electrode was polished with 0.3 µm Al_2O_3 paste and cleaned thoroughly in an ultrasonic water bath for 5 min. The CV and amperometric i-t curves for reduction was carried out in 15 mL of electrolyte containing 0.067 M KNO_3 in water saturated with acetonitrile (ca. 1:3). Oxidation was carried out in 0.1 M CuCl (stabilized by the addition of sodium metabisulfite to the solution) in water saturated with acetonitrile. CV data were acquired at a scan rate of 100 mV/s over a voltage range of 1.2 to -0.6 V. Bulk electrolysis was performed in the same electrolyte solution for up to 30 h (reduction potential -0.2 V, oxidation potential +1.0 V). All electrochemical experiments were performed under N_2 atmosphere with careful exclusion of ambient light. See Figure B.1 for schematic.

3.4.3 Shaping experiments

A large Cu$^+$-hydrogel was prepared as described above. Depending on the desired final shape, the sample was trimmed to size before shaping. Shaping was performed by manipulating the soft gel into a desired shape, often using common lab objects (graduated cylinders, pipettes, scintillation vials) as a structural support. Once the gel was in place, hydration was maintained by wrapping the mold and gel with a dampened paper towel. The sample was then allowed to oxidize by exposure to air for at least 18 h.

Shape memory experiments: Shaped Cu^{2+} samples prepared as described could be returned to their original flat and flexible state by submersion in 0.15 M sodium meta-bisulfite for 20-30 minutes under stirring. Samples could then be re-formed into a different desired shape following the procedure described above.

3.4.4 Mechanical measurements (indentation modulus)

The mechanical testing procedure, specifically developed for the case of testing thin EPEH materials, was based on an indentation testing methodology.[137] A circular cylindrical indentation probe (diameter 5.7 mm) was fashioned to screw into the crosshead of an MTI-1K screw driven, table top load frame. A 75 lb. Transducer Techniques load cell was employed to measure the force exerted on the EPEH specimen by the indentation probe. Owing to the thin nature of the specimens tested (< 10 mm), as well as the small range of expected loading, the strain was calculated from the crosshead displacement as opposed to using an external extensometer. Additional experimental parameters such as strain rate and total strain were determined by referring to ASTM D1621-04A Standard Test Method for Compressive Properties of Rigid Cellular Plastics. For all samples, a

0.15 N preload force was applied prior to taking the measurement. Each indentation test yielded a single stress-strain curve from 0-15% strain, which contributed a single stiffness measurement (compressive modulus). In total, five indentation tests were performed on each 2.5 x 2.5 x 0.2 cm sample (one in each corner, and one in the center of the sample) and the mean value was reported. Per the standard, the modulus is measured by taking the slope of the linear portion of the curve from 10 to 12% strain.

3.4.5 Mechanical measurements (tensile modulus, strips)

Large PSS/PVP hydrogels were prepared and doped in 12.5 cm x 5 cm Teflon molds according to the procedures detailed above. Samples were cut to appropriate size (typically 9-10 cm x 1.5-2 cm) with a straight razor and measured in all dimensions precisely with a micrometer. Contrast markers were applied to the sample about 3 cm in from the location of the grips. Characterization of material stiffness was performed via tensile tests conducted at room temperature, utilizing an MTI-1K (Measurement Technology Inc.) screw driven load frame under displacement control. For all samples, a 0.15 N preload force was applied prior to taking the measurement. A 75 lb Transducer Technologies load cells was employed to measure stress and a Messphysik ME46-450 video extensometer was used to monitor strain. The strategy used adheres to ASTM Standard 882 for thin films, where typical sample thickness is 0.10 mm. Per the standard, the modulus is measured by taking the slope of the linear portion of the curve. In the case of the tensile tests, the modulus is measured by taking the slope of the curve from 1 to 3% strain.

3.4.6 Mechanical measurements (tensile modulus, dumbbells)

Large PSS/PVP hydrogel sheets 1 mm in thickness were prepared as detailed above. After doping with $CuCl_2$, samples were cut into dumbbell shapes using a cutter fashioned after ASTM D412-06a, with length 35 mm, gauge 14.75 mm, and width 3 mm. Sample thickness was measured using a micrometer and varied from 0.67 to 0.76 mm. Stress-strain curves were collected using an MTI-1K load frame with a 75 lb Transducers Techniques load cell at a loading rate of 10 mm/min and the strain was calculated from the crosshead displacement. The modulus was calculated from the slope of the stress-strain curve from 1 to 3 % and the average was reported from 7 to 8 tests per sample per concentration of $CuCl_2$ dopant used, as detailed above.

3.4.7 Multi-well experiment to determine optimum concentration of $CuCl_2$ and urea for doping

SS (3.2 g, 15.5 mmol), VP (0.82 mL, 7.61 mmol), and PEG-DA (M_n = 575, 200 µL, 0.348 mmol) were combined with 18 mL of deionized water and gently heated to below 40 °C until all solids were dissolved. The mixture was purged with N_2 for 3 min. APS (120 mg, 2.2 mol%) was added as radical initiator for copolymerization. Aliquots (2 mL each) of the hydrogel solution were pipetted into nine 2.5 cm x 2.5 cm Teflon wells. The samples were covered with aluminum foil and then heated at 85 °C for 1.5 h. The samples were then allowed to cool to room temperature over a period of several minutes. Samples were doped with solutions that varied in concentration of urea and $CuCl_2$. Urea concentrations were 0.05 M, 0.025 M, and 0.01 M. $CuCl_2$ concentrations were 2.0 M, 1.0 M, and 0.5 M. In a 3 x 3 array, samples were doped with 5 mL doping solution, with $CuCl_2$ concentration decreasing to the right and urea concentration decreasing down as shown in Figure B.2 and Figure B.3. Finally, samples were covered and allowed to sit overnight.

3.4.8 Water content measurements

All measurements were performed in quadruplicate. Hydrogel samples were prepared according to the procedures described above. To calculate water content of the undoped hydrogels, samples were weighed before and after drying 18 h in an 85 ˚C oven, and the mass loss was calculated. To determine the water content of Cu^{2+} and Cu^{+} doped samples, the mass was taken before doping, after doping overnight, and after drying 18-36 h in an 85 ˚C oven; the mass loss was calculated from these values. To obtain the water content of a Cu^{+}-doped sample oxidized in atmospheric conditions, samples were prepared and doped with Cu^{+} as described above. The samples were weighed after doping and allowed to oxidize for 48 hours. Masses were taken for the oxidized samples. The oxidized samples were dried in the oven for 18 h, and a final mass was obtained.

3.4.9 Copper quantitation

The method for quantifying the amount of copper in the EPEHs was based on the quantitative methods reported by Gahler.[138] 2,9-dimethyl-1,10-phenanthroline (neocuproine) was the reagent used to bind Cu^{2+}. $CuCl_2$ standards (0.00148 M) were prepared in concentrated HCl. A Lambda 9 (Perkin-Elmer) UV/Vis/NIR spectrometer was used to create a calibration curve (Figure B.4).

Analysis: HCl was used to break down EPEH’s in order to extract the copper for quantification. Copper-doped samples were digested in 10 mL of concentrated HCl for a period of 18-24 hours. A 200 µL-aliquot of the digested sample solution was diluted in 10 mL water to create a sample stock solution with an absorbance in the range of the instrument. The following reagents were added to a 60-mL separation funnel: 2 mL sample stock solution, 5 mL 100 g/L hydroxylamine hydrochloride, 10 mL 300 g/L sodium citrate, 10 mL 1g/L neocuproine (2,9-dimethyl-1,10-phenanthroline) in absolute ethanol and 10 mL chloroform. The separation funnel was shaken vigorously for 30 seconds, and the contents were allowed to separate. The chloroform layer was collected and the aqueous layer was washed with an additional 5 mL of chloroform. The organic layers were combined and diluted with EtOH to 25 mL in a volumetric flask. The absorbance of the solution was measured at 457 nm and quantified using the calibration curve shown below (Figure B.4).

3.4.10 Electron spin resonance (ESR) spectroscopy

Contributed by Matthew Lawless

The hydrogel was frozen in liquid nitrogen, crushed with mortar and pestle and added into a 50 mM N-Ethylmorpholine (NEM) buffer at pH 7.4 which contained 25% glycerol. Aliquots of the final solution were transferred into a quartz tube with an inner diameter of 3 mm. All electron spin resonance experiments were performed using a Bruker ElexSys E580 which utilized a Bruker ER4118X-MD5 resonator. All experiments were run at a temperature of 80 K which was controlled by an Oxford ITC503 temperature controller with an Oxford CF935 dynamic continuous flow cryostat linked to an Oxford LLT 650 low-loss transfer tube. The samples were frozen in a bath of liquid nitrogen prior to placement into the precooled sample cavity.

All continuous-wave (CW) experiments were performed at X-band. The magnetic field was swept from 2300 to 3900 G for a total of 1024 data points. A conversion time of 20.48 ms, a time constant of 10.24 ms, a modulation frequency of 100 kHz, a modulation amplitude of 4 G and a microwave power of 0.1993 mW were used for all experiments. Simulations of experimental spectra were performed using Bruker Simfonia.

CW-ESR experiments were performed in a NEM buffer (pH 7.4). At pH 7.4, free Cu^{2+} does not contribute to the ESR signal in this buffer. The magnetic $g_{\parallel}$ and $A_{\parallel}$ values are within the range found for type-II Cu^{2+} complexes, indicating that the Cu^{2+} has four equatorial ligands. Furthermore, the values of the $g_{\parallel}$ and $A_{\parallel}$ are consistent with a Cu^{2+} ion coordinating to either three nitrogen and one oxygen (3N:1O) or 2N:2O according to the Peisach-Blumberg plot.[139] The EPR data specifically rule out $[Cu(OH_2)_4(OH)_2]$, which typically yields $g_{\parallel}$ and $A_{\parallel}$ values of 2.42 and 125 G respectively. Note, that the ESR data on these hydrogels did note yield $g_{\parallel}$ and $A_{\parallel}$ values consistent with $[Cu(OH_2)_4(OH)_2]$, even in the absence of NEM (data not shown).

4.0 STIMULI-RESPONSIVE IRON-CROSSLINKED HYDROGELS THAT UNDERGO REDOX-DRIVEN SWITCHING BETWEEN HARD AND SOFT STATES

(Portions of this work were published previously and are reprinted with permission from Auletta, J. T.; LeDonne, G. J.; Gronborg, K. C.; Ladd, C. D.; Liu, H.; Clark, W. W.; Meyer, T. Y. *Macromolecules*, **2015**, 48 (6), 1736-1747. Copyright 2015 American Chemical Society.)

This work was performed in collaboration with Gregory LeDonne, Kai Gronborg, Colin Ladd from the Meyer group. We also thank Prof. David Swigon, Prof. Anna Vainchtein, Hang Nguyen, and Prof. David Waldeck and Prof. Haitao Liu for helpful discussions and feedback.

4.1 INTRODUCTION

We report herein the synthesis and extensive characterization of a unique class of stimuli-responsive hydrogels, which we term electroplastic elastomers (EPEs). These iron-crosslinked hydrogels can be transitioned through a continuum from soft to hard by the application of an electrochemical stimulus that reversibly switches the iron between +2 and +3 oxidation states. A portion of this work has been previously communicated.[140]

As has been established in the last few decades, stimuli-responsive hydrogels are attractive candidates for a broad range of applications such as tissue engineering,[1] drug and protein delivery,[2-3] sensors,[4] actuators,[5] and energy storage.[33] A variety of stimuli, including light,[6] temperature,[7] pH, ionic strength, electric field,[8] magnetic field,[9] enzyme-catalysis,[10] and redox reactions,[11] have been utilized to elicit changes in one or more properties of these materials, with typical responses being degradation, reversible swelling/de-swelling, actuation, sol-gel transition,[54] change in wavelength of diffracted light, changes in mechanical properties,[56] and self-healing.[141] Amongst these many stimuli, we have chosen to focus our attention on electricity because the addition or removal of reagents or heat, which is particularly suitable for some applications, is not always desirable or achievable.

In our responsive EPE hydrogels we harness the unique ability of metal ions to act as reversible crosslinks in polymeric systems. There are numerous examples of the exploitation of this characteristic in previously reported stimuli-responsive metal-containing polymers and supramolecular materials.[32-36] Of particular relevance to our work are those systems that rely on redox-driven changes in coordination around the metal center. Iron, due to the accessibility and stability of the +2 and +3 oxidation states is one of the most widely exploited metals. Tong and co-workers have, for example, reported on the reversible sol-gel transitioning of poly(acrylic acid) PAA using the Fe^{2+}/Fe^{3+} redox couple as controlled by light, air oxidation,[37] or an applied potential.[38] The dynamic bonding of Fe^{3+} with carboxylate ligands has also been utilized for autonomous self-healing of crosslinked PAA hydrogels as reported by Wang and Nie.[39] Reduction is also intrinsic to the photodegradation of Fe^{3+}-crosslinked alginate gels for biocompatible scaffolds reported by Melman and coworkers.[40]

Copper can also be used to promote redox-controlled transitions.[43, 142-144] We have recently communicated the discovery of a copper-based EPE.[145] Rowan and coworkers have described the redox-promoted polymerization/de-polymerization of supramolecular metallopolymers.[43] Mashelkar observed healing in copper-based hydrophobic gels.[46] A copper-based redox system has also been utilized for ionoprinting in poly(sodium acrylate) crosslinked hydrogels as reported by Velev.[146]

Indirectly related, but also relevant, are systems that involve redox-promoted changes in the charge on intact metal complexes. Harada and coworkers have, for example, used a redox strategy to control the host-guest interactions between β-cyclodextrin and ferrocenyl moieties and have demonstrated in their materials reversible associations,[47] self-healing,[48] and mechanical motion.[49] Poly(ferrocenyl siloxanes) have been utilized to prepare color-tunable displays as reported by Manners[50-51] and redox-controlled actuators as demonstrated by Hempenius, Vancso and coworkers.[35] In another case, ferrocyanide has been utilized to control reversibly the degree of swelling of polyelectrolyte multilayers.[52] In these systems, unlike the EPEs described herein, the metal coordination sphere is not changed.

Finally, there are some interesting examples of hydrogel materials that exploit redox as a stimulus but are not metal-based. Disulfide crosslinking, for example, has been utilized to control crosslink density in a variety of systems.[53-56] Electrochemical control of crosslinking has also been demonstrated by altering the charge on polyviologens incorporated in polyelectrolyte multilayers.[30] Quadruple hydrogen bonding motifs have also been utilized to prepare redox responsive gelator systems.[57]

In this report, we also describe the effects of incorporation of graphene oxide (GO) filler into the EPEs, which both reinforced the materials and enabled faster electrochemical transition times between hard and soft states. The mechanical reinforcing ability of GO has been utilized in other polymer hydrogel composites,[83-84, 147-149] specifically in poly(AA),[150] poly(acrylamide) (p(AAm)),[86, 151-153] and poly(acrylic acid-co-acrylamide)[81] hydrogels to varying degrees of success. Differentiated from these systems are GO nanocomposite hydrogels with high extensibility and toughness prepared using PAAm without crosslinker[86] and with peroxide functionalized GO,[151] which acts as both initiator and polyfunctional crosslinker. Only a few reports exist on the utilization of the closely related fillers, graphene,[154] graphite,[155-158] or reduced graphene oxide (rGO),[159] in polymer hydrogel materials.

4.2 RESULTS

4.2.1 Synthesis

As described previously, the basic organic hydrogel (**OR-gel**) is a random copolymer of sodium acrylate (SA), sodium (4-styrenesulfonate) (SS), and polyethylene glycol diacrylate (PEG-DA, M_n = 575) in a weight ratio of 12:8:1 (Figure 4.1).[140] Formed under standard free radical polymerization conditions, the resulting water-swollen hydrogel assumed the shape of the vessel in which the polymerization was conducted. The colorless **OR-gel** was relatively soft and fragile. To introduce reinforcing GO filler, the monomers and initiator were added to an aqueous dispersion of GO prepared by a modified Hummers' method.[160] The addition of the monomers, two of which are salts, destabilized the suspension to some degree as has been reported by others.[89] However, if the polymerization was initiated soon after the addition of the monomers, gravity-induced settling of the GO prior to gelling was minimized. The GO-filled hydrogel (**GO-gel**) was dark brown in color and was significantly tougher than the **OR-gel.**

Iron in either the +2 or +3 oxidation state was introduced by submerging either the **OR-gel** or the **GO-gel** in a solution of the selected metal ion for a period of hours to days. Prior to doping, the **OR-gel** or **GO-gel** was washed multiple times with 1 M HCl to ensure that all carboxylate groups were protonated. This washing replaces the need for the citric acid co-dopant that we employed previously.[140] The introduction of iron in the +3 state to gels at pHs > 2 results in non-uniform doping as the outer edges of the sample become crosslinked and inhibit iron penetration. To facilitate doping efficiency, the iron-doping levels were controlled by timed exposure to a high concentration solution of $FeCl_3$ (2 M). The samples were purposely removed from the doping solutions before complete equilibrium with the doping solution was reached. If the samples were submerged at this high concentration for periods of longer than 24-48 h the combination of iron-induced crosslinking and high ionic strength resulted in hydrogel collapse. Iron penetration appeared both visually and by the determination of mechanical properties to be uniform throughout the gel under the conditions employed, despite the non-equilibrium procedure. Quantitative analysis of the iron content in individual gels was accomplished by first extracting the iron from the gel into solution by exposure to a large excess of HCl. Iron concentration was then determined by UV-Vis spectroscopy.[140]

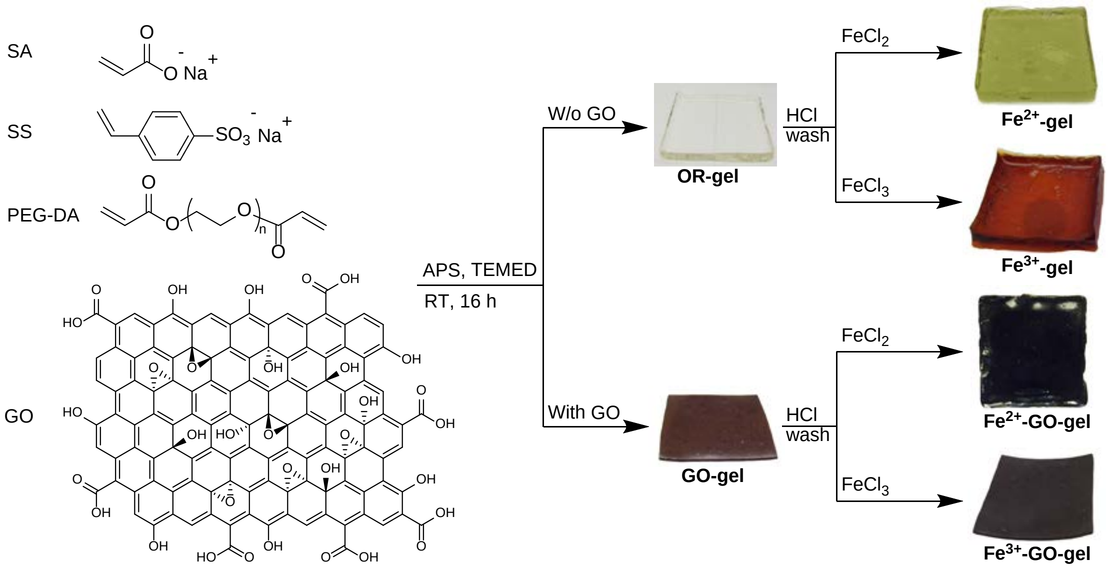

Figure 4.1 Synthesis of OR-gel, GO-gel, and Fe-GO-gels.

Qualitatively, the **Fe^{3+}-gels** produced by direct doping were red in color and dramatically stiffer than the **OR-gel**. The gels also exhibited some deswelling (79% → 44% H_2O, w/w) due to the combination of increasing ionic strength within the gel and the volume minimizing introduction of crosslinks. In contrast, the **Fe^{2+}-gels**, which were pale green in color, while slightly stiffer than the **OR-gel**, remained pliable and lost less water (79% → 52% H_2O, w/w). It should be noted that the carboxylate/styrene sulfonate ratio (12:8) and the amount of the PEG-DA crosslinking agent incorporated was chosen with the goal of maximizing modulus without deswelling the hydrogel significantly. Higher ratios of carboxylate to styrene sulfonate produced gels that did not dope uniformly and/or collapsed from deswelling when doped.

The **GO-gel** was doped in an analogous fashion to the **OR-gel**. Although the inherent color of the metal dopant was masked by GO, a distinct difference in the initial color of the **GO-gel** (brown) and the **Fe^{2+}-rGO-gel** (black, *r*-GO = partially reduced GO) was apparent. The color change observed from brown to black in the case of Fe^{2+} doping is consistent with some degree of GO reduction to give *r*-GO. It has been established previously that Fe^{2+} is a competent reductant for GO and that *r*-GO thus produced is more conjugated.[161-162] As observed in the doping of the **OR-gels**, **Fe^{3+}-GO-gel** is visibly stiffer than **Fe^{2+}-GO-gel.**

4.2.2 Electrochemical transitioning between soft and hard states

As we had previously communicated,[140] the iron-doped EPEs can be electrochemically switched between hard, Fe^{3+}, and soft, Fe^{2+}, states. In particular, we observed that **Fe^{3+}-gel** and **Fe^{2+}-gel** samples (25 x 25 x 3 mm^3), when held with modest pressure on a glassy carbon electrode in an electrolyte comprising 0.5 M citric acid and 2.0 M $FeCl_2$ could be cycled between oxidation states at potentials of -0.8 V (reduction) and 1.2 V (oxidation). The iron EPEs, which were handled under nitrogen and with minimal exposure to light to prevent any possibility of competing light-initiated reduction, exhibited the expected changes in color. Mössbauer spectroscopy confirmed the change of iron oxidation state from high spin Fe^{2+} to high spin Fe^{3+} (Figure C.6).[140] The compressive moduli (Young's) of the samples varied between 1.0 MPa and 0.6 MPa when followed over 2 complete cycles with electrolysis times of ca. 12-16 h (Figure 4.2). It should be noted that the sample was not exhaustively oxidized and therefore did not recover the original modulus. The presence of Fe^{2+} in the electrolyte was necessary to maintain the iron concentration within the gel when the sample was in the reduced state. As the Fe^{2+} interacts only weakly with the hydrogel, the primary consequence of the ion's presence during oxidation cycles is an increase in total charge passed as some of the excess ions are converted to Fe^{3+}. Citric acid was included as a component of the electrolyte early on in these studies because of its perceived role in facilitating homogenous distribution of iron throughout the sample (see earlier discussion of iron doping). Although later experiments demonstrated that the presence of the added ligand was not necessary to enable electrochemical redox switching, it was included in later switching studies so that all data and calculations would be consistent.

Treatment of **Fe^{2+}-gels** with ammonium persulfate as well as exposure to air in a humidity-controlled environment produced physical and optical changes equivalent to those observed in the bulk electrolysis. Chemical reduction of the **Fe^{3+}-gels** proved more challenging as all reagents examined caused noticeable degradation of the gels.

The **Fe-GO-Gels**, which could be prepared and handled as thinner samples (25 x 25 x 0.08 mm^3) due to their enhanced toughness, could be electrochemically cycled more rapidly than the thicker unfilled gels (Figure 4.2). After only 15 min at 1.2 V, the gel stiffened from ~ 1 to 2.4 MPa. Reduction at -0.8 V over for the same time period, however, did not allow for complete recovery. In the next cycle, the oxidation was allowed to proceed for a longer period (30 min) and a higher modulus (3 MPa) was achieved. Reduction for 45 min was required to restore the sample to approximately the cycle 2 starting modulus. A third cycle of 60 min oxidation and 75 min of reduction brought the sample modulus to 3.8 MPa and back to approximately the cycle 2 starting point. Overall, three redox cycles of the sample required only 135 min of electrolysis time and gave a range of moduli of 1-3.8 MPa. These results represent a significant improvement over the times and moduli range observed for the thicker, non-GO-filled gels. When thicker (2-3 mm) **Fe-GO-gel** samples were subjected to electrochemical cycling the switching times were similar to those observed for the **Fe-gels**.

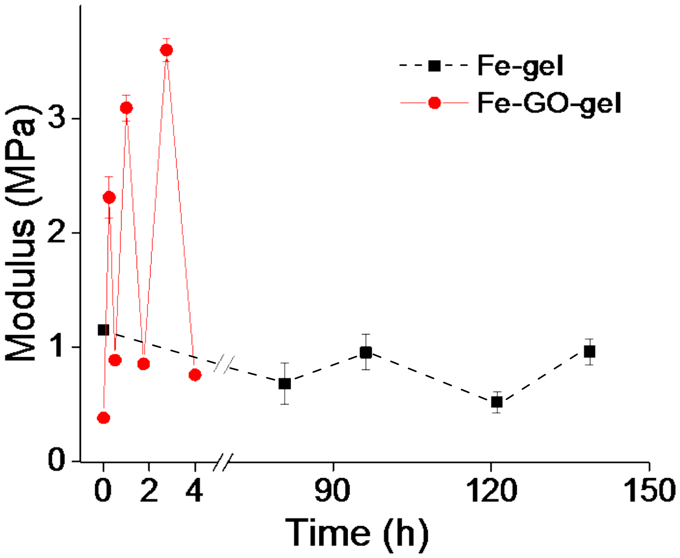

Figure 4.2 Electrochemical switching of Fe-gel and Fe-GO-gel between hard and soft states.

4.2.3 Potentiometric titrations of hydrogels of Fe-gel and OR-gels

In order to determine the mechanism by which iron controls the hydrogel properties, we undertook a series of studies aimed at understanding the nature of the hydrogel and the coordination environment of iron in both oxidation states. The base **OR-gel** polymer, as discussed earlier, formally comprises two potential ligand types, carboxylates and sulfonates. The pK_a of the parent sulfonic acid is, however, very low (-2.8) and the ligand has negligible affinity for the Lewis acidic iron atoms. In control experiments, crosslinked poly(4-stryrene sulfonic acid) did not exhibit deswelling or stiffening in the presence of Fe^{3+}. Interaction between metal and polymer must, therefore, be primarily mediated by the carboxylate groups, which under the low pH conditions within the samples (typically 1-2), are largely present prior to coordination in their protonated form.

The concentration of carboxylic acid groups per volume of hydrogel was determined by potentiometric titration of the gel and the data were analyzed by the Gran plot method (See Appendix C.2 Gran Plot Method).[163] The pH of a fixed volume of aqueous solution in equilibrium with the finely divided gel (prepared by cryomilling) was monitored in all titrations. The data established that the actual ratio of carboxylic acid to sulfonate groups in the polymer prepared from a 12:8 ratio of SA to SS is 9.4:8 which is consistent with high, but not complete, monomer conversion, and the known reactivity ratios of these monomers, 0.34 for SA and 2.3 for SS.[164]

The degree of dissociation of carboxylate ligands, α, as a function of pH was characterized from pH 1.8 to 12.3 by potentiometric titration. All titrations were started by initial addition of excess acid to ensure complete protonation of the carboxylate groups, followed by base addition to the $\alpha = 0$ point. Further base addition produced the expected titration curve. The total acid content of the system during titration is given by

$$h = [H]_{SA} + \alpha[A_t] - [B]_{tot} + oh \tag{4.1}$$

where h is the concentration of hydronium ions, $[H]_{SA}$ is the total concentration of strong acid initially added to the solution, α is the degree of dissociation of the gel carboxylic acid groups, $[A_t]$ is the concentration of all carboxylic moieties (in eq. L^{-1}), $[B]_{tot}$ is the total concentration of base added to the solution, and oh is hydroxide ion concentration calculated from the auto ionization of water.[165] The degree of neutralization (α without metal or α_M in the presence of metal) is then given by

$$\alpha = \frac{h + [B] - [H]_{SA} - oh}{[A_t]} \tag{4.2}$$

The effective pKa of the carboxylic acid substituents was also determined as a function of pH. Although a simple carboxylic acid exhibits a unique pKa of ca. 4.8, the pKa of a particular polycarboxylic acid in a chain of many depends on the state of protonation of its neighboring groups. The ratio of protonated to deprotonated groups varies significantly for pHs near the pK_a. In this regime, the pK_a can be estimated using the extended Henderson-Hasselbalch equation eq.(4.3) where pK_m^H is the apparent dissociation constant at half-dissociation ($\alpha = 0.5$) and n is an empirical constant related to the degree of charging along the polymer backbone and the ionic strength of the medium in which the titration was performed.[165-167]

$$pH = pK_m^H + n \cdot \log\left(\frac{\alpha}{1-\alpha}\right) \tag{4.3}$$

At higher and lower pHs, where nearly all neighboring groups are either protonated or deprotonated, the pK_a stabilizes relative to pH. By considering each acid group as a simple monoprotic acid, the apparent dissociation constant, K_{app}^H, can be calculated from

$$K_{app}^H = \frac{h[A]}{[HA]} = \frac{h\alpha}{1-\alpha} \tag{4.4}$$

In our system a lower and upper limit for the pK_{app}^H of ca. 4.87 (pH of 3.9) and 6.58 (pH of 7.8), respectively, was observed (Figure 4.3).

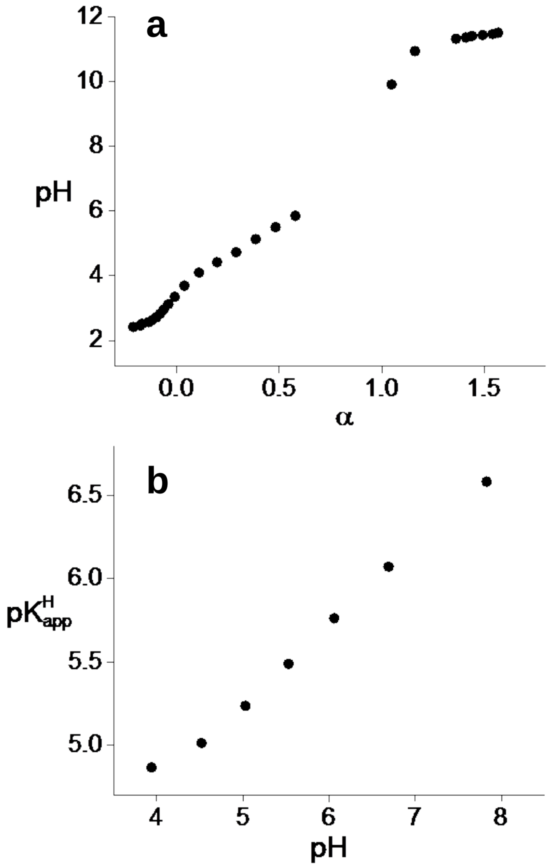

Figure 4.3 (a) Degree of neutralization, α, of hydrogel with pH. Values of α < 0 indicate excess acid present while α > 1 indicate presence of excess base; (b) apparent acid dissociation constant, $\boldsymbol{pK_{app}^{H}}$, of hydrogel variation with pH.

The pH rise from 4.4 to 6.1, corresponding to $\log\left(\frac{\alpha}{1-\alpha}\right)$ of -0.6 to 0.3, can be fit with the extended Henderson-Hasselbalch equation yielding pK_m^H = 5.51 and n = 1.95 (Figure 4.3). These results agree well with previous reports on linear and crosslinked poly(AA) of various molecular weights for titrations performed at similar ionic strengths.[165-167]

To determine the average number of carboxylates bound to each iron center, potentiometric titrations were carried out at various ratios of ligand to metal, R = $[A_t]/[M_t]$. The average number of ligands per metal, $\bar{n}$, could then be calculated from

$$\bar{n} = \frac{[A_t] - [HA] - [A]}{[M_t]} = \frac{[A_t] - [A_t](1-\alpha) - [A]}{[M_t]} \tag{4.5}$$

In this expression, [A] is the concentration of unbound ligand, [HA] is the concentration of protonated ligand, and [M_t] is the total metal ion concentration. As metal coordination is in competition with the binding of protons to the carboxylate moieties, the bound metal can be determined through the measurement of the concentration of the displaced protons. The data collection was conducted by first adding sufficient acid to protonate all the carboxylate moieties and then titrating with base to reach $\alpha = 0$. At this point, the metal was added in a single addition and the pH change was recorded. The mixture was then titrated further with base. The data are plotted in Figure 4.4 below. On the x-axis, the value of $p\left(\frac{[HA]}{h}\right)$ reflects the preference of the ligand for metal ion or protons: a positive value indicates *less* HA than free protons (metal ion displacement of protons on ligand is favored); a negative value indicates *more* HA than free protons (metal ion does not displace protons of ligand). It should be noted that it was not possible to collect data in our normal working pH range of 1-2, as the pH changes due to metal addition were too small to measure accurately in this regime. We propose, however, that a linear extrapolation provides an accurate upper limit and crude estimate for $\bar{n}$ in the pH range of interest because the observed material changes, i.e. modulus, were approximately linear between pH 1 and 3.5. We further extend the extrapolation to $\bar{n} = 1.5$ for the complexation constant calculation described below.

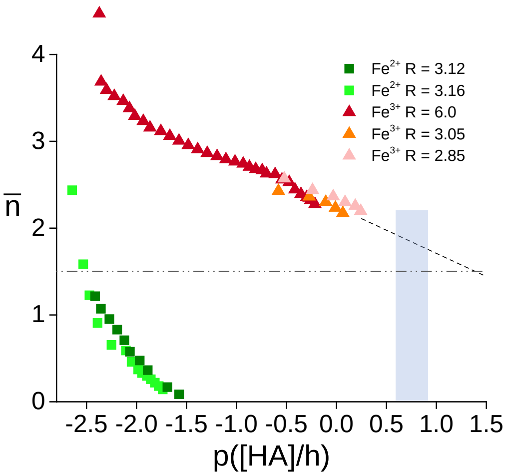

Figure 4.4 Formation curves for Fe^{2+} (■), and Fe^{3+} (▲) with hydrogel at various ligand to metal ratios, R. Dashed line represents extrapolation to pH regime of interest relevant to electrochemical transitioning of material and to $\bar{n}$ = 1.5, which is used to calculate β_3.

Table 4.1 pH as a function of added iron ions[a]

Metal ion	R[b]	pH, initial	pH, Fe^{x+} added	ΔpH
Fe^{3+}	-[c]	2.65	2.54	0.11
Fe^{3+}	6	3.60	2.72	0.88
Fe^{3+}	3	1.82	1.77	0.05
Fe^{3+}	3	2.89	2.38	0.51
Fe^{3+}	3	3.78	2.51	1.27
Fe^{3+}	1	3.61	2.26	1.35
Fe^{2+}	3	3.69	3.66	0.03

[a]pH of solution in equilibrium with hydrogel particles before and after metal ion addition [b]R = [COOH]/[Fe^{x+}], [COOH] = 4.75 to 5.20 meq/L; [Fe^{x+}] = 0.83 to 4.89 mM; [c]Iron only, no gel present.

As shown in Figure 4.4, the behavior of Fe^{2+} and Fe^{3+} differed significantly. The Fe^{2+} data were shifted further to the left and approach zero as p([HA]/h) increases, indicating weak or no binding to carboxylate groups when the concentration of H^+ is high. The calculated $\bar{n}$ values for Fe^{3+}, in contrast, ranged from ca. 1.5 to 3 which is the expected value based on charge balance considerations alone. It is also important to note that at R = 3, the addition of Fe^{2+} ion to the gel at $\alpha = 0$ resulted in only a slight decrease in pH from 3.69 to 3.66 (Table 4.1). In contrast, the addition of a similar concentration of Fe^{3+} gave an immediate pH drop of 3.78 to 2.51, consistent with immediate coordination. From control studies, it was determined that the contribution to the pH drop due to the addition of the Lewis acidic Fe^{3+} ion to an aqueous solution at pH 2.65 was only 0.11.

Binding for both metals did increase with the addition of base but the data clearly establish that the binding of Fe^{2+} at low pH can be considered negligible even when the carboxylate ligands are present at R =3 (which is an excess if one considers only charge balance arguments). Obviously, this experiment does not eliminate the possibility of weak association of the protonated acid groups with the metal ions. It simply establishes that the Fe^{2+} cannot displace the weakly bound protons which make this class of crosslink significantly weaker and less likely to contribute to bulk modulus.

In contrast with Fe^{2+}, binding for Fe^{3+} was found to be very strong even at low pH. Addition of Fe^{3+} to the gel at $\alpha = 0$ caused an immediate and dramatic change in the pH. The magnitude correlated with R; addition of larger concentrations of Fe^{3+} produced more solvated protons.

The calculation of these average coordination numbers and the determination of the relevant complexation constants is based on the following rationale, which has been used by others for similar systems.[166, 168] We can consider the overall complexation reaction, in general, as

$$M + nHA \rightleftharpoons MA_n + nH \tag{4.6}$$

where M is the metal ion, HA is the carboxylic group in protonated form, and *n* is the number of carboxylates attached to the metal. The overall complexation constant can then be expressed as in eq. (4.7),

$$B_n = \frac{[MA_n] \cdot h^n}{[M][HA]^n} \tag{4.7}$$

The concentration of bound ligands can be expressed as the sum of all coordinated species (eq. (4.8)) and can be rewritten in terms of the complexation constant by substitution of the expression for [MA$_n$] from eq. (4.6) (eq. (4.9)).

$$[A_{bound}] = \sum_{n=1}^{N} n[MA_n] \tag{4.8}$$

$$= [M]\sum_{n=1}^{N} nB_n\left(\frac{[HA]}{h}\right)^n \tag{4.9}$$

Total metal ion concentration [M$_t$] can then be written as the sum of all species that include metal ions as shown in eq. (4.10).

$$[M_t] = [M]\left[1 + \sum_{n=1}^{N} B_n\left(\frac{[HA]}{h}\right)^n\right] \tag{4.10}$$

Average coordination can be calculated as the ratio of ligands bound to total metal ion concentration as in eq. (4.11).

$$\bar{n} = \frac{[A_{bound}]}{[M_t]} = \frac{\sum_{n=1}^{N} nB_n\left(\frac{[HA]}{h}\right)^n}{1 + \sum_{n=1}^{N} B_n\left(\frac{[HA]}{h}\right)^n} \tag{4.11}$$

Moreover, as described by Gregor and coworkers,[166, 168] the maximum number of ligands per metal ion can be estimated at a given pH by plotting the average number of ligands per metal, $\bar{n}$, against p([HA]/h). The complexation constants can then be estimated in the case of a divalent metal ion at $\bar{n}$ = 1.0, where $\log\left(\sqrt{B_2}\right) = p([HA]/h)$ and $\beta_2 = B_2/{K_a}^2$ and in the case of a trivalent metal ion at $\bar{n}$ = 1.5, where $\log B_3 = 3p([HA]/h)$ and $\beta_3 = B_3/{K_a}^3$ (Table 4.2).[168]. In this case, the B values, which reflect the pH conditions under which the measurements were acquired, are of more interest than the absolute formation constants, β.[169] The log B_2 of -4.24 measured at pH 4.69 demonstrates the extremely poor coordination of the Fe^{2+} ions under even mildly acidic conditions; Fe^{2+} binding decreases further as pH is lowered). In contrast, the log B_3 for the Fe^{3+} ions of 4.18 determined at pH 0.74 shows that coordination is significant even at low pH.

Table 4.2 Displacement (B's) and formation constants (β's) for Fe^{2+} and Fe^{3+} with OR-gel

Metal ion	R, equiv. COOH/[M]	pH	pK_a^H	log B_2	log β_2	log B_3	log β_3
Fe^{2+}	3.12	4.69	5.13	-4.24	6.0[b]	-	-
Fe^{3+}	-	0.74[a]	4.87	-	-	4.18[a]	18.8[a]

[a]Estimated by extrapolation to $\bar{n}$ = 1.5; [b]log $\beta_2 \cong 0$ at pH < 3.5

It is also of interest to estimate the percentage of the total iron that is bound to the hydrogel. Although we know from quantitative analysis that excess iron is present, we were not able to distinguish or independently measure the relative concentrations of the various iron species in solution. Based on simple stoichiometry, however, an upper limit of 57% of unbound iron can be determined by assuming $\bar{n}$ = 3. The actual number of $\bar{n}$ = 0 iron ions present would be expected to be substantially lower, however, as there will be a distribution (n = 1 – 3) of complexes present.

4.2.4 Mechanical properties of Fe-gels

Initially, we were interested in exploring the relationship between Fe^{2+} and Fe^{3+} crosslinking as we believed Fe^{2+} would contribute to crosslink formation, albeit to a lesser extent than Fe^{3+}. In this light, **Fe-gels** with varying ratios of Fe^{3+}:Fe^{2+} were prepared by doping **OR-gels** in solutions containing both ions, with $[M^{x+}]_{total}$ fixed at 0.5 M. As detailed above, however, it was found that Fe^{2+} does not bind with the gel at low pH. Thus, the modulus was determined and plotted as a function of the ratio of Fe^{3+} to carboxylate ligand (Fe^{3+} determined for each by quantitative analysis, Figure 4.5). At a ratio of Fe^{3+}:L of ca. 0.15, the modulus increased steeply, consistent with significant Fe^{3+}-crosslink formation. The highest Young's modulus (E) observed at Fe^{3+}:L of ca. 0.45 was 2.7 MPa. Although, higher moduli may be obtained by increasing the overall Fe^{3+} doping level, the hydrogel samples eventually collapse under the osmotic pressure differential induced by the high ionic strength of the dopant solution. Moreover, the samples become brittle and unsuitable for redox switching.

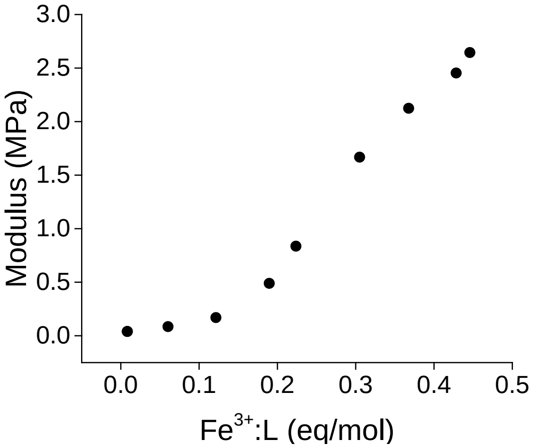

Figure 4.5 Modulus of Fe^{3+}-gels as a function of metal:carboxylate ratio

4.2.5 Graphene-oxide hydrogel composites (GO-gels)

From our previous report, a major limitation of the material was the long switching times between hard and soft states. As electrochemical and diffusion studies (vide infra) suggested that the source of the slow switching was diffusion limited ion migration within the gel, we were interested in preparing thinner samples with a potential for enhanced ion and electron conductivity. As the simple **OR-gels** are quite fragile and could not be easily manipulated (necessary for doping) if their thickness was reduced below ~1 mm, a variant base of the base gel was prepared by incorporation of GO as filler. The tougher **GO-gels** could be easily cast as 100 micron thick films, which represented a factor of 20 decrease in maximum diffusion distance.

The mechanical properties of **GO-gels** were investigated under tensile and compressive load. The Young's modulus was calculated according to the theory of rubber elasticity

$$\sigma = G(\alpha - \alpha^{-2}) \tag{4.12}$$

by plotting the stress against α-α^{-2}, where α is the extension ratio ($\alpha = \Delta L/L_0$), and the slope of the line was taken as the shear modulus, G, with E = 3G. Figure 4.6 shows the stress-strain curves under tensile load for **GO-gels** with 0 to 5% GO (w/w) up to 30% strain. A 2-fold improvement in Young's modulus was found at 1% GO loading. The modulus increased with higher GO loading and showed a maximum of 3.4-fold improvement over the original **OR-gel** at 4% GO, but decreased at 5% GO, consistent with classic filler effects. **GO-gels** were also subjected to cyclic compression loading up to 50% strain and the energy dissipated during the loading/unloading cycle was calculated from the area of the hysteresis loop, U_{hys} (Figure 4.6, Table 4.3). As the fraction of GO was increased, the **GO-gels** withstood higher stresses and dissipated more energy. Even though the Young's modulus fell upon increasing the GO fraction from 4 to 5%, the trend of increased toughness was followed and the sample at 5% GO dissipated more of the applied energy.

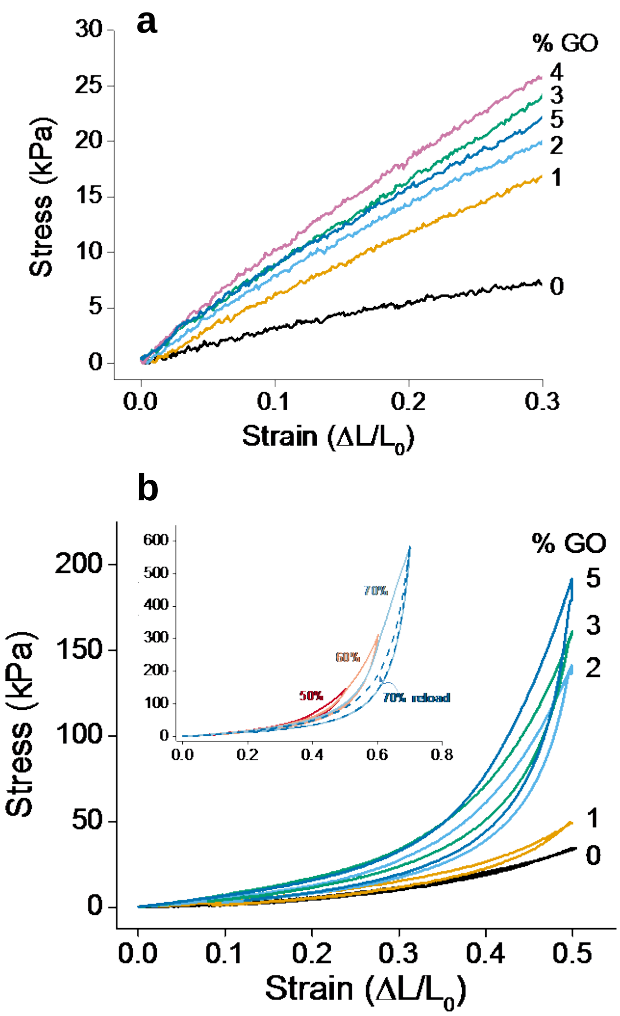

Figure 4.6 (a) Stress-strain plots of OR-gel and GO-gels with 1 to 5 % GO under tensile load; (b) Stress-strain plots of OR-gel and GO-gels with 1 to 5% GO under cyclic compressive load to 50% maximum strain; Inset: Cyclic loading to progressively higher strain, 50, 60, 70, and re-loaded to 70% maximum strain.

Cyclic loading under compression to progressively higher strains was also examined (Figure 4.6, inset). Here, the **GO-gel** stress-strain curves exhibited features characteristic of the Mullins Effect.[170] During the second loading and all subsequent cycles, the stress-strain curve followed the prior unloading curve and then deviated as the historical maximum strain was exceeded, finally following the path expected if the sample were not subjected to cyclic loading at all. This behavior is likely due to the adsorption of polymer chains on the GO surface and desorption upon mechanical loading. Contributions from the mechanical deformation of GO filler and bond rupture of polymer chains covalently and/or physically grafted to GO cannot be ruled out.

Table 4.3 Young's modulus of OR-gel and GO-gels and energy dissipated (U_{hys}) during cyclic compression

% GO	E (kPa)^a	E (kPa)^b	U_{hys} (kJ/m3)^c
0	46.4	33.9	0.47
1	79.6	72.9	1.29
2	106	82.5	4.80
3	129	104	4.76
4	-	116	-
5	95.9	92.7	7.75

^{a}Measured by compression test; ^{b}Measured by tensile test; ^{c}Dissipated energy during cyclic compression loading to 50% strain

Scanning electron microscopy images of the fracture surface of the **OR-gel** and **GO-gel** showed significantly different features (Figure 4.7). The fracture surface of the **OR-gel** was found to be relatively flat and smooth, consistent with the brittle nature of the gel where crack propagation can proceed unhindered. The **GO-gel**'s fracture surface, however, was found to be rough and uneven, suggesting that crack propagation may be dampened by the presence of the GO filler.[153] No clear distinction between GO-filler and polymer network was found in any **GO-gel** SEM images, suggesting that the GO filler was completely coated by polymer.

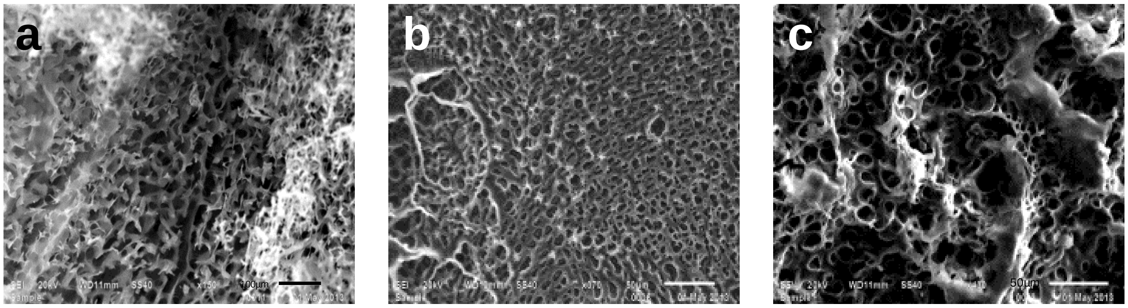

Figure 4.7 SEM images of fracture surface of, (a) lyophilized graphene oxide (from 12.5 mg/mL aqueous dispersion, scale bar 100 µm), (b) OR-gel (scale bar 50 µm), and (c) GO-gel (1 % w/w GO, scale bar 50 µm).

4.2.6 Mechanical properties of Fe-GO-gels

The effect of iron doping on the mechanical properties of **GO-gels** was also examined and the Young's modulus was determined as discussed above (Table 4.4). Upon doping with Fe^{2+}, the modulus increased from 0.068 MPa for **GO-gel** to 0.214 MPa for **Fe^{2+}-GO-gel,** a significant improvement over the **Fe^{2+}-gel** modulus of 0.073 MPa. A more modest enhancement was found for Fe^{3+} doping, with the **Fe^{3+}-gel** modulus increasing from 2.71 MPa to 3.87 MPa for **Fe^{3+}-GO-gel**. Given that GO possesses many different oxygen-containing surface functionalities, including carboxyl groups, it is not surprising that iron doping enhances the mechanical properties, as has been reported elsewhere.[89] While the modulus difference between oxidation states decreased slightly for **Fe-GO-gels**, the enhanced toughness as demonstrated for **GO-gels** above represents a significant improvement.

Table 4.4 Young's modulus of Fe-GO-gels as determined by tensile testing

Fe^{x+}	% GO	E (MPa)
-	-	0.038
-	1	0.068
Fe^{2+}	-	0.073
Fe^{2+}	1	0.214
Fe^{3+}	-	2.71
Fe^{3+}	1	3.87

4.2.7 Magnetic susceptibility

The magnetic susceptibility of Fe^{3+}-gels was investigated as a function of iron content (Figure 4.8). Although subtle, μ_{eff} appears to slowly decrease from ~5.3 to ~4.3 with increased L:Fe^{3+}. Considering a mononuclear Fe^{3+} complex with five unpaired electrons would theoretically give μ_{eff} ~5.92, it is likely that polynuclear Fe^{3+} clusters are present. Cluster formation has also been implicated in the interaction of Fe^{3+} with the homopolymer of acrylic acid.[171] In non-polymeric systems, reactions of Fe^{3+} with monomeric carboxylate ligands produces clusters that have been characterized spectroscopically and crystallographically.[172-176]

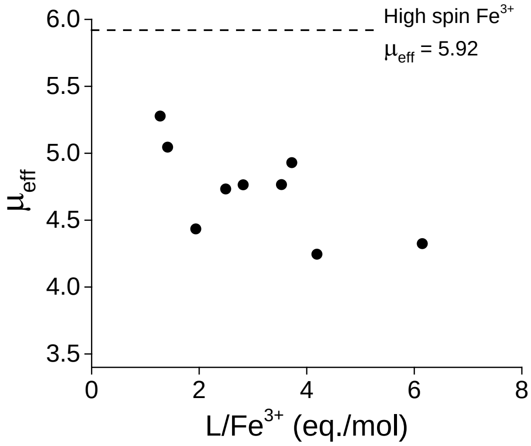

Figure 4.8 Magnetic susceptibility of Fe^{3+}-gels at various metal:ligand ratios.

4.2.8 The role of pH and proton diffusion

(Contributed by Colin Ladd and Kai Gronborg)

We independently determined the rate of proton diffusion in the **Fe^{3+}-gels** for two reasons: 1) the mechanical properties depend strongly on pH so it was important to understand the time required for equilibration between external solutions and the hydrogel in cases where an initial pH differential existed, and 2) proton diffusion is an essential component of restoring charge balance within the hydrogels during the electrochemical redox switching.

The proton diffusion coefficient for a typical **Fe^{3+}-gel** was measured using a simple diaphragm cell. A circular sample cut from a **Fe^{3+}-gel** (~0.7 mm thickness) was used as the diffusion membrane and the two chambers contained solutions of 0.1 M $FeCl_3$ adjusted to pH 1 and 1.75, respectively. The pH change over time was monitored as the solutions equilibrated.

From Fick's laws of diffusion, the proton diffusion coefficient, *D*, can be calculated from the known pH change in each cell,

$$D = \frac{1}{\beta t} \ln\left(\frac{C_1(t) - C_2(t)}{C_1^0 - C_2^0}\right) \tag{4.13}$$

where t is the instantaneous time of record, $C_1(t)$ and $C_2(t)$ are the instantaneous concentrations of the tanks, higher and lower concentrations respectively, C_1^0 and C_2^0 are the initial concentrations of the tanks, higher and lower, respectively, and β is a geometric constant related to the design of the diaphragm cell and hydrogel dimensions.[177] Explicitly, β is given by

$$\beta = \left(\frac{A_H}{W_H}\right)\left(\frac{1}{V_1} + \frac{1}{V_2}\right) \tag{4.14}$$

where A_H is the area of the hydrogel, W_H is the gel thickness, and V_1 and V_2 are the volumes of tanks 1 and 2, respectively. The diffusion coefficient was determined from the slope of the line from the plot shown in Figure 4.9, *D* = 1.04 x 10^{-8} ± 0.03 x 10^{-8} cm^2/s (n = 3). The value is on the same order of magnitude for Fe^{3+} diffusion coefficients measured during the electrochemical reduction of an **Fe^{3+}-gel** (≈ 10^{-8} cm^2/s),[140] but is significantly lower than diffusion coefficients typically measured for swollen hydrogels (≈ 10^{-6} cm^2/s).

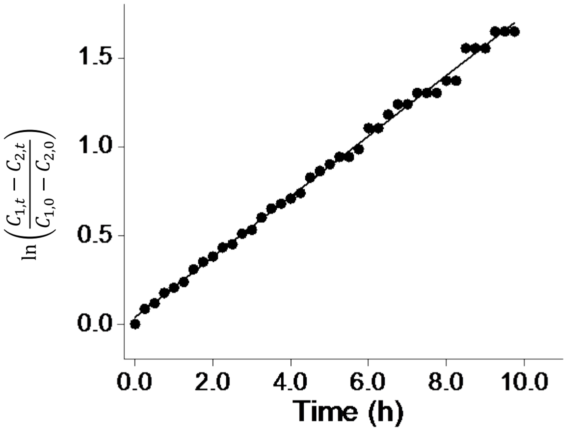

Figure 4.9 Determination of proton diffusion coefficient in Fe^{3+}-gel.

Knowing the time frame for diffusion in these samples, we are able to explain originally perplexing experimental observations and correct for the problem. Specifically, we had noted that **Fe^{3+}-gels** that had been reduced to Fe^{2+} and then re-oxidized to Fe^{3+} often exhibited moduli much higher than that observed for the original gel prior to exposure to the electrochemical set-up. The issue appears to be the differential between the electrolyte solution (2.0 M $FeCl_2$/0.5 M citric acid) which has a pH of 1.72 vs. that of the doping solution used in the preparation of the Fe^{3+} samples (2.0 M $FeCl_3$/0.5 M citric acid) which has pH of 0.95. Although this pH differential is not large, control experiments on hydrogel doped with Fe^{3+} at this higher pH produced moduli of similar magnitude. The enhanced moduli of the redox-switched Fe^{3+} samples can be attributed to an increase in pH inside the gel due to proton diffusion out of the hydrogel into the higher pH electrolyte. To nullify the pH effect in the electrochemical switching process all such experiments were subsequently started, therefore, with samples in the Fe^{2+} state.

4.3 DISCUSSION

The EPE hydrogels described herein undergo a redox-promoted transition from soft to hard states. Using multiple techniques we have developed an understanding of the mechanism and characteristics of this response. It is clear from the observed changes in color, the Mössbauer spectra, and the parallel behavior of the chemically reduced samples, that bulk electrolysis occurs within the hydrogels when they are subjected to the appropriate potentials within an electrochemical cell. The iron is converted reversibly from a +2 to a +3 state within the entirety of the hydrogel even though only one surface of the gel is in contact with the electrode.

Potentiometric titration established that this change in oxidation state had a profound effect on the ability of the iron ions to form crosslinks by complexation with the polyelectrolyte backbone. As expected, based on simple hard-soft acid base reasoning, the Fe^{+3} ions bind more tightly to the hard carboxylic groups than do the soft Fe^{2+} ions. Specifically, we found evidence that under the low pH conditions at which these samples are optimally manipulated, the binding of Fe^{2+} is negligible. The coordination of Fe^{3+}, in contrast, continued to be significant at low pHs, as can be seen by both the obvious change in properties of the samples and the drop in measured solution pH that is observed when protons are liberated upon introduction of Fe^{3+} to the hydrogel. Quantitative analysis of the titration data gave an upper limit estimate of the formation constants. Although these simple experiments do not produce a full picture of the number, types and distribution of metal complexes formed, it is clear that the Fe^{3+} is competent as a crosslinking agent. Additional insight into the nature of the complexes can be found in the magnetic moment measurements, which are consistent with the presence of iron clusters. As this type of cluster formation has been postulated before in systems involving poly(acrylic acid), and as clustering is well-established in the reaction of iron with monovalent carboxylate ligands, we expect that the metal-crosslinks consist of a complex mixture of iron coordination motifs, some of which are multi-nuclear. Clusters would be expected to form particularly effective crosslink structures with a potential for binding a larger number of chains than could an isolated metal ion.

The modulus of the hydrogel samples could be tuned by adjusting the iron concentration within the hydrogel. The measured modulus of the **Fe^{3+}-gels** increased linearly with increasing iron concentration. While simple complexation behavior would predict that at sufficiently high concentrations saturation of the modulus and even an eventual decrease due to a disruption of the crosslinking should be expected, this behavior was not observed in practice because of the competing collapse of the hydrogel structure at high ionic strengths.

The introduction of graphene into the **OR-gels** increased their modulus by a factor of ~2 from ~0.04 MPa to ~0.07 MPa. The **Fe-GO-gels** are also significantly stiffer, giving moduli in the range of ~0.2 to 3.9 MPa for the 2.5 x 2.5 x 3 mm^3 samples. With this increase in modulus, the practical preparation and handling of thinner samples was facilitated. These samples, which had dimensions of 2.5 x 2.5 x 0.08 mm^3, exhibited moduli in the 0.1 to 5 MPa range. While the nature of the interaction between the GO and the hydrogel could not be fully characterized there is potential, in addition to the intrinsic physical interactions between the network and the filler, for both direct attachment of the chains to the surface and interaction of the peripheral carboxylic acid groups with the iron ions. It was somewhat surprising, given the many possible network-filler interactions and the high aspect ratio of GO,[178] that the reinforcement measured was relatively modest.[179-180] We suggest that GO aggregation is one likely reason for the lower-than-predicted filler effect. Since we know that GO precipitates in the presence of the charged monomers over long periods, it seems likely that some aggregation of the GO sheets has begun before the polymerization gels. The larger GO particles would have lower aspect ratios and their performance as fillers would be diminished.

The GO also underwent chemical change in the presence of the reducing Fe^{2+} dopant. The change in color of the sample was consistent with some degree of reduction, although there was no overall change in the bulk conductivity measured. The reduction, which would be expected to decrease the functionality of the GO particles, should also affect the interaction with the network and increase the hydrophobic attraction between nearby *r*-GO particles. Although we could not directly characterize the changes in the GO/*r*-GO filler, we did note that the color of samples that had been re-oxidized to Fe^{3+} did not revert to the original brown. We hypothesize, therefore, that the GO is present in a partially reduced form once it has been exposed to Fe^{2+}.

As described in the preliminary communication,[140] the chronocoulometry exhibited a current profile consistent with diffusion control which has significant implications on the bulk electrolysis kinetics and mechanism for these unstirred hydrogel samples. In the electrochemical experiment, in which the samples are situated such that one face is in contact with the working electrode and the other with the electrolyte in which is submerged the counter electrode, the electrons must migrate between the electrode surface and iron ions located in complexes located up to 3 mm away (Figure C.5). We propose the following mechanism for the electrolysis. The abundant iron ions, ca. 60% of the Fe^{3+} ions and nearly 100% of the Fe^{2+} ions, which are not bound to the polymer, diffuse to and from the electrode surface to undergo redox. These unbound ions in various stages of oxidation are available to either exchange with bound metals, thereby freeing them to diffuse to the electrode, or to act as electron-transfer intermediates, delivering or receiving electrons from metals that are firmly chelated. It should be noted that the unbound irons are not present in the electrochemical experiment as simple ions, but are at least partly chelated by the citric acid added to the electrolyte. Although we have observed electrochemical transitioning of the EPEs in electrolytes without the added ligand, all studies reported herein were conducted in the presence of the citric acid to maintain consistency with data collected at earlier time points.

Consistent with this proposed mechanism, the conversion of thinner (ca. 100 micron) samples doped with GO was much faster. These samples transitioned in minutes rather than hours. It should be noted that we did initially hope that the GO would, in addition to reinforcing the materials, facilitate the redox process by acting as a distributed electrode. We did not see any evidence for this behavior, however. Thicker (2-3 mm) samples required similar transition times to those observed for the **Fe-gels** without GO filler.

The role of protons in this system is complex. The EPEs, like nearly all hydrogels, are extremely sensitive to pH. In this case, however, these effects are minimized by the low pH range (1-2) at which the EPE system is optimally operated. There are several reasons that this pH range is ideal: 1) the formation of insoluble iron oxides, which form at higher pHs, is prevented; 2) The coordination differential between the Fe^{3+} and Fe^{2+} ions is maximized; 3) the sample has a water-swollen hydrogel structure with a significant number of mobile iron ions, which we believe is intrinsically important for homogeneous doping and for the electrochemical conversion as described above; 4) the high mobility of the protons facilitates the migration of protons in and out of the gel which is necessary for charge balance; and 5) the high Lewis acidity of the iron ions necessarily produces acidic aqueous solutions. Despite the relatively narrow pH range that was employed, pH effects were still apparent and extreme care was required to obtain reproducible mechanical data. Consistent with the potentiometric titrations, even slightly higher pH’s lead to tighter binding of the Fe^{3+} ions, which in turn, produced materials with higher moduli.

4.4 CONCLUSION

In conclusion, we have developed the first example of an electroresponsive hydrogel that can be tuned reversibly between hard and soft states via electrochemical tuning of the coordination affinity of metal crosslinks. Unlike purely supramolecular systems, these materials maintain a 3-dimensional shape rather than becoming a sol when the iron-based crosslinks are disrupted. The mechanism of the response involves the reversible formation of iron-based crosslinks, where the +3 states has been shown to interact strongly with the carboxylate groups on the polymer chains while the +2 state iron is largely dissociated. The electrochemical conversion, which is apparently diffusion controlled, can be accelerated from hours to minutes by the incorporation of a GO filler into the hydrogel which increases the base modulus of the material and thereby enables a decrease in sample thickness from 3 mm to ca. 100 microns.

4.5 MATERIALS AND METHODS

4.5.1 Materials

Sodium acrylate (SA), sodium 4-styrene sulfonate (SS), poly(ethylene glycol) diacrylate (PEG-DA, $M_n = 575$), ammonium persulfate (APS), N,N,N′,N′-tetramethylenediamine (TEMED), $FeCl_3$, $FeCl_2 \cdot 4H_2O$, citric acid, sodium citrate, and ascorbic acid were purchased from Sigma Aldrich. Poly(dimethylsiloxane) (PDMS) was commercially purchased locally, under the brand name GE Silicone II Kitchen & Bath. Flake graphite was from Sigma (product number 332461).

4.5.2 Hydrogel prep using APS/TEMED catalysis without graphene oxide

SA (4.8 g, 51 mmol) and SS (3.2 g, 14.3 mmol) were combined with 36 mL of deionized water and gently heated (< 40 °C) until all solids were dissolved. PEG-DA, (400 μL, 0.78 mmol) and an aqueous solution of TEMED (10% (v/v), 236μL) were added and the mixture was purged with N_2 for 10 min. An aqueous solution of APS (90 mg/mL, 800 μL, 0.47 mol%) was added as a radical initiator for copolymerization.

4.5.3 Preparation of graphene oxide

Graphite oxide (GtO) was prepared following a modified Hummers' method.[79] For a typical preparation, flake graphite (1.0 g) was added to conc. H_2SO_4 (46 mL) that had been cooled to 0 °C. $NaNO_3$ (1.0 g) was added to the stirring suspension. $KMnO_4$ (6.0 g) was then added slowly to prevent vigorous reaction. The mixture was heated to 35°C for 1 h, diluted with dH_2O (80 mL) and stirred for an additional 30 minutes. H_2O_2 (3 mL of 3 % v/v) was added, the reaction mixture was stirred for 30 minutes, and sonicated for 1 h. Large particulates were separated by centrifugation at 1000 rpm for 1 min. A wet pellet of the product graphite oxide was then collected by centrifugation of the supernatant at 10,000 rpm for 90 min. The pellet was treated with HCl (1 M x 45 mL) and subjected to repeated dH_2O/centrifugation cycles until the pH of the supernatant was ~ 7. The final dry sample (1.69 g) was obtained by lyophilization of the wet pellet. GO was characterized by SEM, TGA, and FTIR (See Appendix C.1 Graphene Oxide Characterization, Figure C.1-C.3).

4.5.4 Preparation of graphene oxide doped hydrogels

Exfoliation of the GtO to form stable dispersions of GO in water was accomplished by ultrasonication (Branson 2200) of the dry GO powder (1 to ~ 125 mg, depending on the desired suspension concentration) for 1-2 h in 2 mL of dH_2O. At higher loadings, the suspensions were also subjected to vortex mixing before beginning sonication to break up large chunks of GtO and ensure homogeneous dispersion. SA (0.267 g, 2.84 mmol), SS (0.178 g, 0.79 mmol) and PEG-DA (22 µL, 0.043 mmol) were dissolved in the GO dispersion by stirring and vortexing. TEMED (26 µL x 5.0 % (v/v)) was added, the mixture was vortexed for several seconds and then purged with N_2 for 10 min. APS solution (90.0 mg/mL, 44 µL, 3.96 mg, 0.47 mol%) was added and the mixture was briefly vortexed. To remove bubbles introduced during the preparation, the vial was evacuated briefly and allowed to stand under static vacuum for ~1 min. The pre-polymer mixture was transferred to glass tubes (5.9 mm in diameter and ~50 mm length) or sandwiched between two glass slides (25 mm x 75 mm) separated by 100-110 µm spacers and allowed to polymerize overnight at RT.

The films were removed from between the glass slides by swelling the samples in dH_2O and floating/peeling the films from the substrates. The hydrogel films obtained were allowed to equilibrate in dH_2O and washed/rinsed 3x with copious dH_2O. **Fe^{2+}-GO-gels** were prepared by immersing the films in 20 mL of 2 M $FeCl_2$/0.5 M citric acid for 3-5 days. Similarly, **Fe^{3+}-GO-gels** were prepared by immersing the gel in 20 mL of 2 M $FeCl_3$/0.5 M citric acid overnight. The **Fe^{2+}-GO-gels** became black in color during this time period due to reduction of the GO by Fe^{2+}.[161] The films were cut to 5 mm x 25 mm strips or 25 mm x 25 mm squares and used for subsequent electrochemical and mechanical characterization.

Cylindrical samples for mechanical testing were prepared independently as described below.

4.5.5 Mechanical testing: indentation, compression, tensile

The mechanical testing procedure, specifically developed for the case of testing thin EPEH materials, was based on an indentation testing methodology.[120] A circular cylindrical indentation probe (diameter 6.2 mm) was fashioned to screw into the crosshead of an MTI-1K screw driven, table top load frame. A 10N or 333N Transducer Techniques load cell was employed to measure the force exerted on the EPEH specimen by the indentation probe. Owing to the thin nature of the specimens tested (< 10 mm), as well as the small range of expected loading, the strain was calculated from the crosshead displacement as opposed to using an external extensometer. Additional experimental parameters such as strain rate and total strain were determined by referring to ASTM D1621-04A Standard Test Method for Compressive Properties of Rigid Cellular Plastics. Each indentation test yielded a single stress-strain curve, which contributed a single stiffness measurement (Young's modulus). In total, five indentation tests were performed on each 25 x 25 x 2 mm^3 sample (one in each corner, and one in the center of the sample, Figure C.7) and the mean value was reported. Per the standard, Young's modulus is measured by taking the slope of the linear portion of the curve (Figure C.8).

Samples for compression testing were cast in glass tubes 5.9 mm in diameter and cut to 5-6 mm in length and compressed at a loading rate of 1-5 mm/min. Force and crosshead displacement was recorded and the stress-strain curves were analyzed by assuming 0.05 N of force were needed to make good contact with the sample where this point was set equal to zero strain. The Young's modulus (E) was then calculated after plotting the stress-strain data according to eq. (4.12) in the main text and the slope was taken as the shear modulus, G = 3E.

Fe-GO-gels for electrochemical cycling were cast either as films (80-110 µm thick, cut to dimensions of 25 mm x 25 mm), or as bulk samples, 5.9 mm diameter and 50 mm length, gauge length ~20mm. Force and crosshead displacement were recorded at a velocity of 10 mm/min. Young's modulus was calculated as done for compression testing using eq. (4.12) with the slope of the linear portion of the curve taken as the shear modulus, G = 3E.

4.5.6 Electrochemical methods

Cyclic voltammetry (CV) and amperometry measurements were carried out with a CH Instruments Electrochemical work station Model 430A (Austin, TX) at RT using a three-electrode system composed of a glassy carbon plate (GCE, 25 mm x 25 mm) working electrode, a Ag/AgCl reference electrode, and a platinum grid counter electrode. The GCE was polished with 0.3 µm Al_2O_3 paste and cleaned thoroughly in an ultrasonic water bath for 5 min prior to each use. The CV and amperometry experiments for reduction and oxidation were carried out in 15 mL of 2.0 M $FeCl_2$/0.25 M citric acid, pH ~1.8. CV data were acquired at a scan rate of 100 mV/s over a voltage range of 1.2 to -0.8 V. Bulk electrolysis was performed in the same electrolyte solution for up to 40 h (reduction potential -0.8 V, oxidation potential +1.2 V). All electrochemical experiments were performed under N_2 atmosphere with careful exclusion of ambient light to prevent the photoreduction of Fe^{3+} ions in the presence of citric acid.[37]

Fe^{2+}-GO films were prepared as described above and cut to 25 mm x 25 mm squares for electrochemical cycling. Prior to beginning a redox cycle, -0.8 V was applied overnight to the

Fe^{2+}-GO-gel to reduce any Fe^{3+} formed during the doping process to Fe^{2+}. The initial modulus was determined and taken as the beginning of a redox cycle after this point.

4.5.7 Hydrogel preparation

OR-gel samples were prepared according to the procedure given above. After polymerization, the samples were washed with copious dH_2O for 3 days, (multiple dH_2O changes per day) to remove unreacted monomers, oligomers, and impurities. The swollen, washed hydrogel pieces were transferred to a drying dish and placed in an oven at 85 °C for three days until a constant mass was obtained. The dried pieces were then ground using an electric grinder and finally crushed into fine powder using a mortar and pestle. The finely crushed, powdery hydrogel was dried in the re-dried in an oven overnight at 85 °C to ensure complete removal of water, and finally stored in a desiccator at RT.

4.5.8 Potentiometric titrations

Potentiometric titrations were performed using a VWR SB20 SympHony pH meter equipped with a Vernier tris-compatible flat pH sensor.

Potentiometric titrations were carried out according to a modified protocol adapted from Mouginot[167] and Morlay.[165] (See Appendix C.2 Gran Plot Method). Sodium hydroxide stock solution (NaOH, 0.1 M) was standardized using a weighed amount of potassium monohydrogen phthalate (KHP). The flask containing NaOH was kept free of carbonate using a CO_2 trap of NaOH beads attached to the opening of the flask. Nitric acid (HNO_3, 0.1 M) was standardized against the 0.1 M NaOH stock solution. Sodium nitrate (1.0 M stock) was used throughout. The stock solutions of iron(II) chloride and iron(III) chloride were 0.2 M (actual concentration determined by UV-vis analysis as previously reported[140]).

For a typical titration, 200 mg ± 5 mg of dried hydrogel were placed in a 250 mL Erlenmeyer flask with a stir bar. 160 mL of Millipore dH_2O were added and the hydrogel pieces were allowed to swell for 20 min. The pH probe was then inserted into the flask. 20 ml of 1.0 M $NaNO_3$ (0.1 M $NaNO_3$ final) were added and stirred for 20 min, followed by 20 mL of 0.1 M HNO_3, and the mixture was purged with N_2 for 15 min, after which the solution was kept under nitrogen for the duration of the titration. Aliquots of 0.1 M NaOH (50 µL to 1000 µL) were added to the stirring hydrogel and the pH was recorded after equilibrium was reached. In the absence of iron, and before the deprotonation of hydrogel ligands, equilibrium was achieved in < 1 min. Once deprotonation began (~pH 3.7, absence of iron), equilibrium took from 5 min to 30 min. In the presence of iron, equilibration time varied from 5 min to 1 h (total titration time from 2 to 12 h. pH measurements were corrected for the eventual drift of the pH probe during the course of titration by recording the measured pH change of standards used to calibrate the probe at the start and end of the titration (typically 0.01 to 0.02 pH units).

The total acid content of the hydrogel was determined by the Gran plot method[163] (Figure C.4). Briefly, the strong acid and total acid content for a given titration as descried above were determined. The difference between strong and total acid was taken as the weak acid content of the system and set equal to the carboxylic acid content of the hydrogel.

4.5.9 Magnetic susceptibility

Magnetic susceptibility measurements were made using a Johnson Matthey Magnetic Susceptibility Balance MSB Mk1. **Fe^{3+}-gels** were prepared by doping with various concentrations of $FeCl_3$ from 0.002 M to 2.0 M (the OR-gel was washed with 1 M HCl prior to iron doping). **Fe^{3+}-gels** (~0.5 g) were flash frozen in liquid nitrogen and ground into small pieces with a mortar and pestle while submerged under liquid nitrogen. The crushed **Fe^{3+}-gel** pieces were then transferred to a 1 dram vial, the headspace flushed with N_2, and then allowed to warm to RT before transferring to MSB tubes. A portion of the crushed hydrogel was reserved for iron quantitative analysis and determination of water content by mass.

4.5.10 Scanning electron microscopy

Scanning electron microscopy (SEM) was performed using a JEOL JSM-6510LV. Hydrogel samples were flash frozen in liquid nitrogen, fractured while frozen, and lyophilized. The dried fracture surfaces were imaged without sputtering or painting, so the sample stage was tilted several degrees while imaging to minimize charge accumulation.

4.5.11 Fourier transform infrared spectroscopy

Fourier Transform Infrared Spectroscopy (FTIR) was performed using a Thermo Nicolet Avatar FTIR from 500 to 4000 cm^{-1} at 4 cm^{-1} resolution. A dispersion of graphene oxide in ethyl acetate (~1 mg/ml) was drop cast onto KBr disks to collect the spectra.

4.5.12 Proton diffusion coefficient determination

An **OR-gel** was prepared by polymerizing approximately 6mL of a monomer solution (as described above) between two glass plates separated by 1mm spacers under an N_2 atmosphere.

Polymerization was allowed to progress for at least 12 hours. The glass plates were first coated with Rain-x to facilitate extraction from the mold. After removing the sample from the mold, it was soaked in 0.5M NaCl (~30 minutes) to swell and remove excess unreacted monomer. Gels were washed (soaked for ~15 minutes) with 50mL of 1M HCl three times followed by doping in 50mL of 0.1M $FeCl_3$ (pH ~1.75) for 16 hours. The **Fe^{3+}-gel** thickness was measured using a micrometer (to ± 0.01 mm).

PVC tubing with a ¾ inch (~2cm) internal diameter was purchased to construct a water-tight diffusion cell. Two 90° elbow joints were connected to a union with Teflon tape lining the threads to ensure a seal. The **Fe^{3+}-gel** was then positioned inside the union such that a seal was created between the O-ring and the gel.

Solutions of 0.1M $FeCl_3$ (to prevent iron from leeching out of the gel) were mixed at pHs of ~1 and ~1.75. Vernier tris-compatible flat pH sensors were calibrated using pH 4.00 acetate buffer and pH 7.00 phosphate buffer. pH values for the buffers were recorded before and after the experiment to correct for any instrument drift. Approximately 12mL (measured to 0.1mL) of the pH adjusted $FeCl_3$ solutions were added to either side of the diffusion cell with a stir bar in each compartment, the pH probes inserted and the compartments sealed with Parafilm. The solutions were stirred throughout the duration of the experiment to eliminate contributions from bulk diffusion and to ensure that $[H^+]$ at the gel surface was equal to $[H^+]$ of the bulk. pH values were collected for each solution every 15 minutes using Vernier Software & Technology's LoggerPro software.

After ~8 hours, the experiment was stopped. Bulk volumes were measured to ensure no volume change due to evaporation. Each pH probe was used to measure the pH of the buffers to determine any instrument drift. Data was exported as an Excel file and used to calculate the diffusion coefficient of protons through the Fe^{3+} doped hydrogel.

5.0 INFLUENCE OF COUNTERION IDENTITY ON THE PROPERTIES OF IONOMERS FOR USE IN ELECTROADHESIVE LAMINATE STRUCTURES WITH REVERSIBLE BENDING STIFFNESS

This work was performed in collaboration with Colin Ladd and Emily Barker from the Meyer group. Carlos Arguero and Eliot George from the Clark group contributed to theoretical discussions, programming, instrument design, and mechanical measurements. We thank Prof. Susan Fullerton for helpful discussions on impedance spectroscopy. We also thank Abhijeet Gujrati from the Jacobs group for help with optical profilometry.

5.1 INTRODUCTION

The ability to switch a material between rigid and flexible states is intrinsically important as it is central to a variety of applications. A material may, for example, be converted from a solid to a liquid and back again during molding, or alternatively the properties may be adjusted to improve the interaction with another material. There are many stimuli that can be used to change the mechanical properties of a material including temperature, chemical additives, solvation, and electricity. Although each of these methods are valuable and appropriate for certain applications, electricity offers particular benefits for systems in which heating/cooling are impractical and for systems in which the addition and removal of chemical reagents is not desirable. In considering how electricity can be used in this context, there are two fundamental approaches: 1) electrochemical, or the use of electrons to induce redox transitions in chemical species and 2) electrostatic, or the use of an electric field to induce changes in the distribution of charge within a material. We have previously investigated and reported the synthesis and characterization of a hydrogel system that undergoes soft-hard transitions using the first mechanism (Chapters 2,3, and 4).[145, 181-182] In this chapter, we shift our focus to the study of materials whose behavior is controlled by electroadhesion, which falls under the second mechanism.

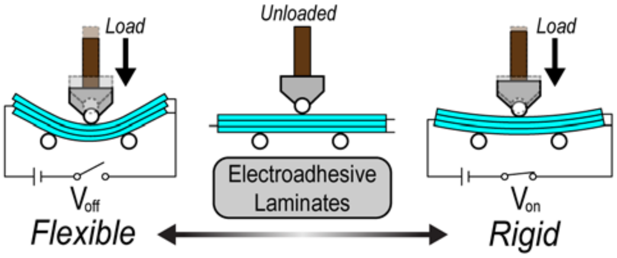

Figure 5.1 Application of an electric potential induces an adhesive force between the layers of the laminate, switching the structure between flexible and rigid states.

Our objective is to use electricity to tune the flexural rigidity of laminates comprising polymer-coated electrodes. The electroadhesive force that develops between these layers will pin the layers such that they will behave as a single beam. It should be noted that, on the macroscopic level, these laminates will not act as actuators; the voltage-induced differences will be primarily in the degree of interaction of the layers. Significant bending of these structures is not expected without the application of an external force.

Electroadhesive laminates of this type have a wide range of potential applications including armor/protective gear with adjustable flexibility,[183] components whose geometry can be redefined as needed (shape-memory),[184] and vibration damping. Electroadhesion has been investigated previously for applications such as climbing[185-186] and perching robots,[187] flexible grippers,[188] haptic feedback systems,[189] wafer chucking,[190-194] and Poisson's ratio[195] structures. More closely related to our goals, however, are the reports of electroadhesion as a tool for tuning rigidity in laminates.[196-198]

5.2 COULOMBIC AND JOHNSEN-RAHBEK FORCES

There are two fundamental mechanisms that can result in electroadhesion of the type required to make functional electroadhesive laminates, Coulomb and Johnsen-Rahbek. When an electric potential is applied across two materials in apparent contact (Figure 5.2), the coulombic electrostatic force generated depends on the identity of the material and the physical characteristics of the interface. For an ideal parallel plate geometry the electrostatic force is given by:

$$F_C = \frac{A\varepsilon_0}{2}\left(\frac{\varepsilon_s}{d}V\right)^2 \tag{5.1}$$

where A is the apparent area of contact, d is the thickness of the dielectric material, ε_0 is the permittivity of free space, ε_s is the dielectric constant of the substrate, and V is the applied voltage. The degree of attraction between the oppositely charged surfaces depends not only on the charge at the interface but also on the gap, g, between the layers (Figure 5.2a).[199-200] As noted by Qin and McTeer for ceramic materials[190] and Strong and Troxel[189], the gap-attenuated force may be modeled as two capacitors in series, assuming a uniform spacing and no surface roughness.

$$F_C = \frac{A\varepsilon_0}{2}\left(\frac{\varepsilon_g\varepsilon_s}{d\varepsilon_g + g\varepsilon_s}V\right)^2 \tag{5.2}$$

where ε_g is the dielectric constant of the gap (typically air, ε_g = 1) and g is the gap thickness with $g \ll d$.

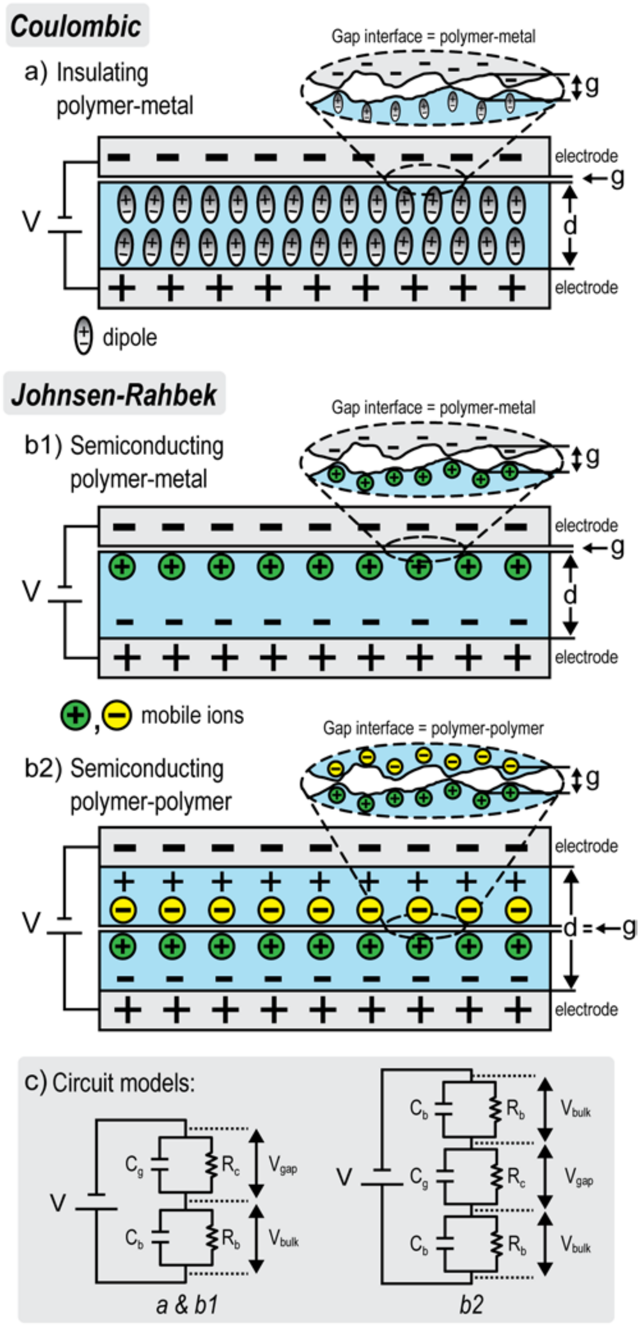

Figure 5.2 Generation of electrostatic attraction between two surfaces depending on resistivity of material and contact resistance. (a) Coulombic attraction and Johnsen-Rahbek (JR) attraction (b1) at metal-polymer interface, and (b2) JR attraction at polymer-polymer interface; (c) Circuit models for (a) where $R_c < R_b$, (b1) where $R_c > R_b$, and (b2) where $R_c > R_b$.

When the dielectric material is imperfect or contains mobile charge carriers, a second electrostatic force, termed the Johnsen-Rahbek force (JR-force), can become dominant (Figure 5.2b).[201] This force, which is intrinsically greater at the same applied potential relative to the coulombic force, typically manifests in dielectric materials with lower resistivities (ρ ≈ 10^6-10^{10} Ω·cm) compared to those found in coulomb-only systems (ρ > 10^{13} Ω·cm). The presence of mobile ions in JR-active ionomers allows the build-up of a sufficiently high surface charge under an applied potential that the adhesive force depends increasingly on the magnitude and profile of the gap, rather than the thickness of the dielectric. To define the force of this interaction, a more realistic description of the gap is necessary. Due to surface irregularities the interaction is non-uniform and consists of a relatively small number of contacts and a distribution of gap areas and distances (Figure 5.2).

The voltage drop across the dielectric, in this case, will depend on the relative magnitude of the contact resistance (R_c) experienced by the points at the interface in actual contact and the bulk resistance (R_b) of the dielectric. Where the materials contact one another, electrical conduction becomes possible. If however, R_c is significantly greater than R_b, the JR-force will be observed. The voltage at the interface can be modeled as a resistive divider (5.3)and the JR-force expressed as shown in (5.4)

$$V_{\text{eff}} = V\left(\frac{R_c}{R_b + R_c}\right) \tag{5.3}$$

$$F_{JR} = \frac{A_{\text{eff}}\varepsilon_0}{2}\left(\frac{\varepsilon_g}{g}V_{\text{eff}}\right)^2 \tag{5.4}$$

where A_{eff} is the effective area of contact and V_{eff} is the effective voltage at the interface.

The circuits formed in Figure 5.2a and b may be modeled as two (or three) parallel RC circuits in series (Figure 5.2c). In all cases, the gap voltage (V_{gap}) is given by a simple voltage divider, eq. (5.3). For a Coulombic material, V_{gap} is significantly lower than the applied voltage since $R_b \gg R_C$ and much of the voltage drop occurs through the material itself (V_{bulk}). For a JR material, where $R_c \gg R_b$, V_{gap} is nearly equal to the applied voltage, V. Thus, most of the voltage drop occurs at the interface of the two materials. This is the origin of the high force generated by the JR-effect: a large voltage drop across as small gap, g.

Since the initial work by Johnsen and Rahbek,[201] the bulk of JR reports have focused on the use of ceramic materials to clamp and hold flat silicon wafers during elaboration. Watanabe, who was among the first to report the use of the JR-effect for wafer chucking, investigated the influence of changing relative humidity on the chuck performance and found that at higher relative humidity contact resistance is lowered, thereby decreasing the electrostatic force generated.[202] Qin and McTeer investigated the influence of the wafer thickness on the chucking and de-chucking response time.[190-191] Shim and Sugai also investigate chucking and de-chucking response.[192] Kanno, et al., proposed a model based on surface roughness to describe the contact resistance and the electrostatic force generated between non-ideal surfaces.[203] Balakrishnan also considered the effect of moisture on the system.[204] Theoretical considerations were furthered by Stuckes[205] who investigated the JR-force for use in an electrostatic clutch and Atkinson who put forth a model encompassing field emission at contacting asperities.[206] More recently, Watanabe investigated the effect of transition metal oxide additives in alumina-based electrostatic chucks.[207]

For polymer dielectrics, little has been reported about the use of ionomers to generate JR-force based adhesion—instead the studies have focused on materials without mobile charges that exhibit only Coulomb-mechanism behavior. Of particular relevance, however, are prior reports in which Coulomb-based electroadhesion was used to control the stiffness of composite or laminate structures. Bergamini reported a sandwich beam with an electrostatically tunable bending stiffness using poly(vinylidene fluoride) (PVDF) and poly(tetrafluoroethylene) (PTFE) at the interfaces[196] and a glass fiber reinforced-carbon fiber reinforced plastic beam with tunable bending stiffness utilizing PVDF at the interface.[197] Di Lillo investigated the use of several different polymers for electrobonded laminates, including fluorinated ethylene propylene (FEP), perfluoroalkoxy copolymer (PFA), Mylar (polyester; BoPET), and polyimide (Upilex 25RN).[208] Di Lillio also mentions the importance of layering and highlights the ratio of flexural modulus between on and off states as the number of layers squared, and extends this theory to layered materials of dissimilar mechanical properties (i.e. multiple polymer-electrode layers).[209] As it is known that the shear stress transfer between layers depends on the coefficient of friction, Ginés investigated the frictional behavior of polymeric films (FEP, PFA, PVDF, and polyimide) under mechanical and electrostatic loads.[210] Layered systems have been reported by Tabata, who prepared a microfabricated construct with 200 layers x 27 µm/layer[211] and Heath, who explored the use of electroadhesion in bonding fiber-reinforced composites under mechanical loading.[212]

5.3 IONOMERS AS MATERIALS FOR THE JR-EFFECT

We are intrigued by the possibility of designing high-performing ionomer-based electroadhesive materials for laminates with electrically controlled JR-force-based adhesion. The idea is to use electricity to turn on and off the adhesion between layers such that the mechanical properties of the layered structure depends on the voltage applied. We are choosing to focus on ionic materials that will express JR-force for multiple reasons: 1) as discussed above, these lower resistivity materials have the potential for generating higher forces with lower input voltages in comparison with the non-ionic dielectrics; 2) optimization of these ionic materials for specific applications by altering the chemical structure will be facilitated by the larger pool of materials that fit the JR-criteria (mobile ions, moderate resistivity, high contact resistance) relative to those that are appropriate for coulomb-only electroadhesion; and 3) creation of structures with application-relevant dimensions and responses is more easily accomplished for JR materials because the force generated is not inversely dependent on the polymer layer thickness as it is for Coulomb-based systems. The layer thickness may, therefore, be chosen to address other design considerations.

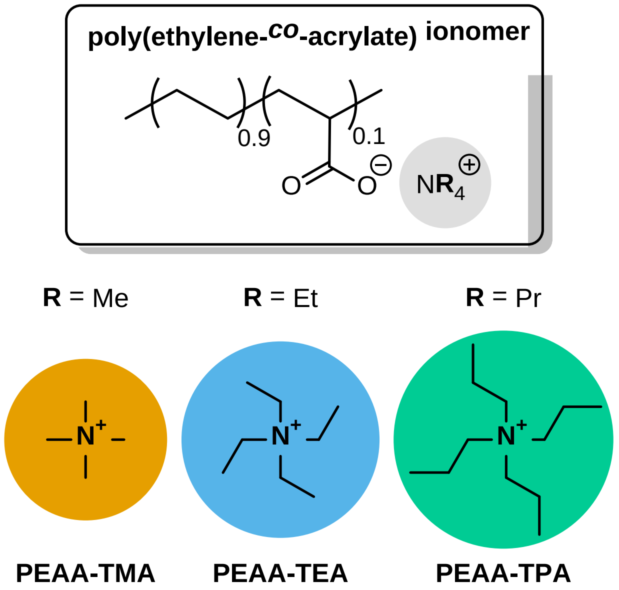

Figure 5.3 Structure of neutralized PEAA ionomer.

In the current study, we begin our examination of structure and function in JR-type ionomers by characterizing the counterion effects on the performance of a series of poly(ethylene-*co*-acrylic acid) ionomers (PEAA, Figure 5.3). Tetraalkylammonium cations were investigated because the diffuse nature of their charges lend themselves to weak association to the polymer backbone. The effect of increasing alkyl chain length of the alkyl substituent was investigated and correlated with a variety of intrinsic properties.

5.4 LAMINATES AND THE JR-FORCE

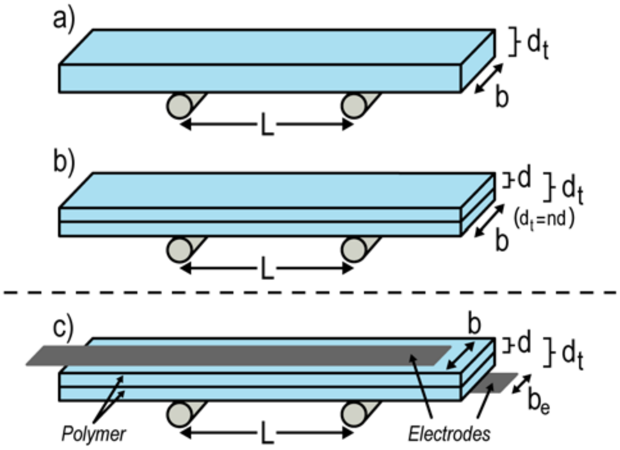

Figure 5.4 Beam structures: a) solid beam; b) solid beam divided into *n* layers of equal thickness (bilayer structure shown); c) bilayer structure with electrodes.

The flexural modulus of the layered laminate structures incorporating these polymers will be determined using a classic three-point bending analysis (See Appendix D.3 Elastic Beam Theory). If we consider a simple beam as shown in Figure 5.4a, the force required to displace the beam at small strains is given by eq. (5.5) and, accordingly, the flexural modulus of the beam is given by eq. (5.6)

$$F = \frac{4E_\mathrm{f} b d_t^3}{L^3} D \tag{5.5}$$

$$E_\mathrm{f} = \frac{L^3 F}{4 b d_t^3 D} \tag{5.6}$$

where E_f is the Young's modulus of the material, b the width, d_t the total thickness, L the span of the beam, and D is the displacement at the midpoint of the structure. If the beam is divided into *n* unbonded layers of equal thickness *d* (Figure 5.4b,c), the force required to displace the structure now depends on the number of layers as in (5.7) and the flexural modulus of an individual layer will be given by (5.8)

$$F = \frac{4E_\mathrm{f}bd_t^3}{L^3n^2}D \tag{5.7}$$

$$E_\mathrm{f} = \frac{n^2L^3F}{4bd_t^3D} \tag{5.8}$$

Note that both equations (5.6) and (5.8) yield the same result for the flexural modulus of the material, assuming no interaction between layers; it is the force required to displace the structure a given distance which varies with the number of layers. As we are interested in using electroadhesion to alter the mechanical properties of the entire laminate structure, we assume the number of layers to be $n = 1$ and use the entire structure thickness d_t to find the effective flexural *rigidity* of the structure, E_R, for all applied voltages.

$$E_\mathrm{R} = \frac{L^3F}{4bd_t^3D} \tag{5.9}$$

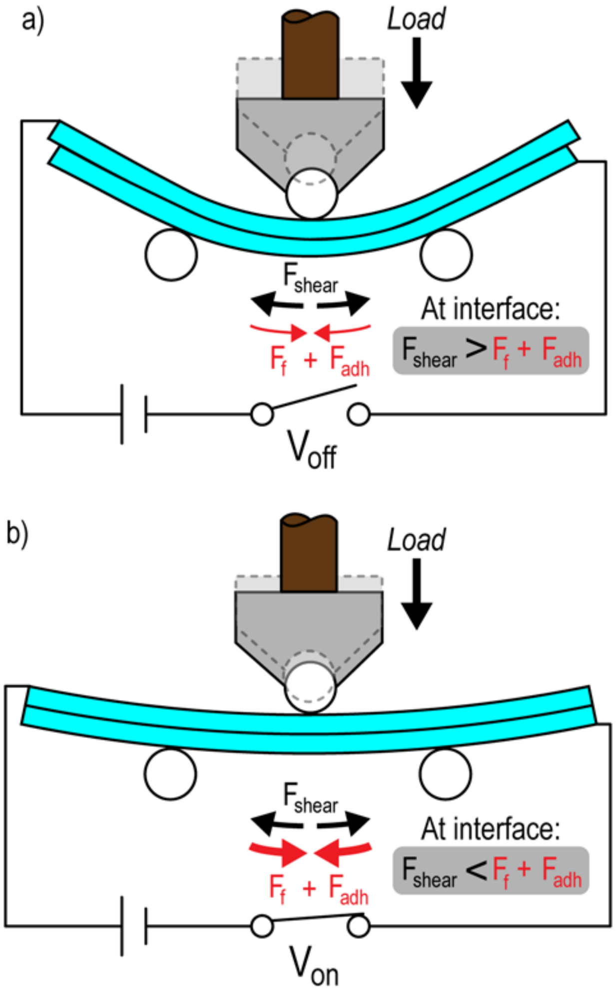

Figure 5.5 Partial and complete bonding of layers due to electroadhesive and friction forces. a) Interfacial forces are weaker than shear force due to displacement of midpoint of structure and layers may slide (Case 1 when $\boldsymbol{F_f} + \boldsymbol{F_{adh}} = \mathbf{0}$, Case 2 otherwise); b) Interfacial forces are greater than shear forces and layers cannot slide (Cases 3 and 4).

In this simple model, no additional contribution from friction or adhesion between the layers is considered. However, a far more complicated picture arises when considering bonding or partial bonding between the layers (Figure 5.5). Several different cases may be considered: 1) **Unbonded and uninteractive**: assuming no interaction between layers, the plies will act individually—this is the case described in eq. (5.8); 2) $\boldsymbol{F_{shear}} > (\boldsymbol{F_f} + \boldsymbol{F_{adh}})$**:** both friction and static friction are present – sliding of layers may occur during displacement of midpoint of structure once the shear force at the interface overcomes the shear forces due to friction and adhesion (Figure 5.5a); 3) $\boldsymbol{F_{shear}} < (\boldsymbol{F_f} + \boldsymbol{F_{adh}})$: near the areas of intimate contact, shear force due to electroadhesion is greater than the shear force during the displacement of the midpoint of the structure (Figure 5.5b). No sliding occurs at these contact points. Sliding may occur at other regions where the electroadhesive force is less than the shear force. *At a critical adhesive force, the structure will behave as a solid beam of the same total thickness*. This is the case that is described in eq. (5.9); 4) $\boldsymbol{F_{shear}} \ll (\boldsymbol{F_f} + \boldsymbol{F_{adh}})$: hypothetically, the total of all adhesive forces could be greater than the force required to shear a solid beam of the same total thickness during displacement if the adhered interfaces, which have a finite but unknown thickness, are stiffer than the base material. The E_{R} of the laminated construct would then exceed the modulus of the base material.

5.5 RESULTS

5.5.1 Synthesis of poly(ethylene-*co*-acrylic acid) tetraalkylammonium ionomers

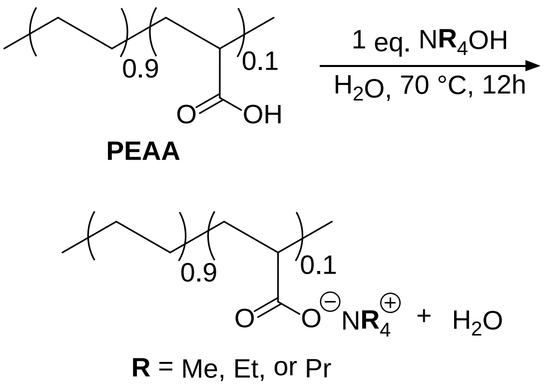

Scheme 5.1 Neutralization of poly(ethylene-*co*-acrylic acid) (PEAA) with tetraalkylammonium hydroxides.

PEAA is a random free-radical copolymer of ethylene and acrylic acid repeat units with a weight ratio of 8:2. The molecular weight (M_n) of the material as purchased from Sigma-Aldrich was determined by size-exclusion chromatography to be 41 kDa, relative to polystyrene standards. To prepare the tetraalkylammonium derivatives, PEAA, which is nearly insoluble in water, was suspended in a solution of the tetraalkylammonium hydroxide prepared with 1:1 mole ratio of the desired ion to acrylic acid. The neutralized ionomer dissolved to form a translucent solution. When cast as free-standing samples, the ionomers were flexible, elastic solids. Qualitatively, the ionomers became tackier and more flexible as the ion increased in size. PEAA-X derivatives are named by appending the counter ion abbreviation (methyl = TMA, ethyl = TEA, propyl = TPA).

5.5.2 Relative humidity influence on water uptake of ionomers.

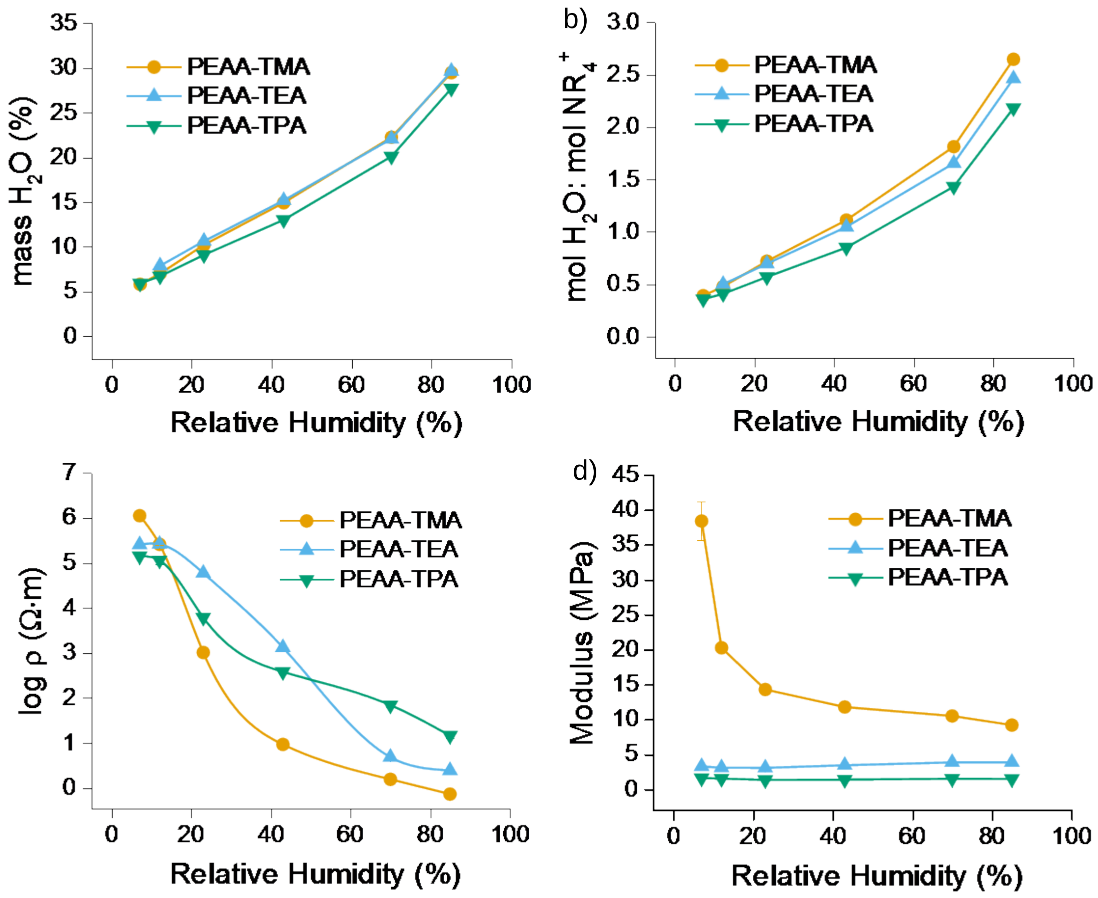

Figure 5.6 a) Water content, b) mole ratio of water to counterion, c) resistivity, and d) Young's Modulus of PEAA-TMA, PEAA-TEA, and PEAA-TPA at 7, 12, 23, 43, 70, and 85% relative humidity and 23°C.

The water content of the ionomer series was studied at six relative humidities (RH) from 7-85%. Water content was monitored during drying by both mass (Figure 5.6a) and FTIR spectroscopy (Figure 5.7). The mass percent of water was found according to eq. (5.10):

$$m_{H_2O} = \frac{m_t - m_0}{m_t} \times 100\% \tag{5.10}$$

where m_t is the hydrated sample mass and m_0 is the dry sample mass. Water uptake follows the trend TMA>TEA>TPA corresponding to less water uptake for the larger, more hydrophobic counterions, both by weight (Figure 5.6a) and when normalized for ion content (Figure 5.6b). FTIR confirmed water loss during drying by decreasing absorbance of the water O-H stretch at 3000-3600 cm^{-1} between wet and dry states (Figure 5.7).

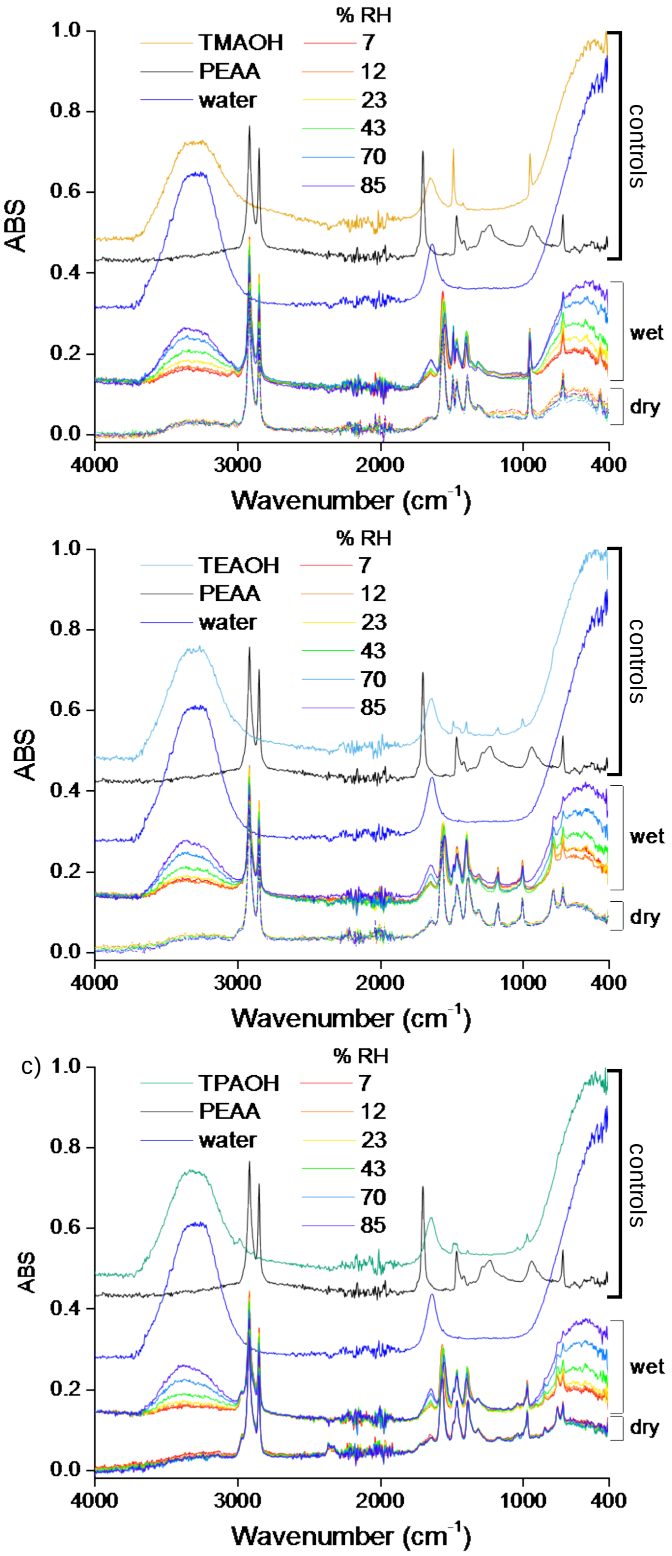

Figure 5.7 FTIR spectra of ionomers after conditioning at 7, 12, 23, 43, 70, and 85 %RH for three weeks (wet) and after vacuum oven drying at 45 °C for three days (dry) for a) PEAA-TMA, b) PEAA-TEA, and c) PEAA-TPA.

5.5.3 Thermal behavior

The thermal behavior of the materials was determined by differential scanning calorimetry (Table 5.1, Figure 5.8). Interestingly, virgin PEAA exhibited a glass transition temperature of 38 °C, which is higher than previous reports. The deviation is likely due to either block length differences in the copolymer or variations in water content.[213,214] PEAA, which is a semicrystalline polymer, exhibited both crystallization and melting peaks at 50 °C and 56 °C, respectively. The tetraalkylammonium derivatives are amorphous with T_gs that decreased, as would be expected, with increasing ion size.

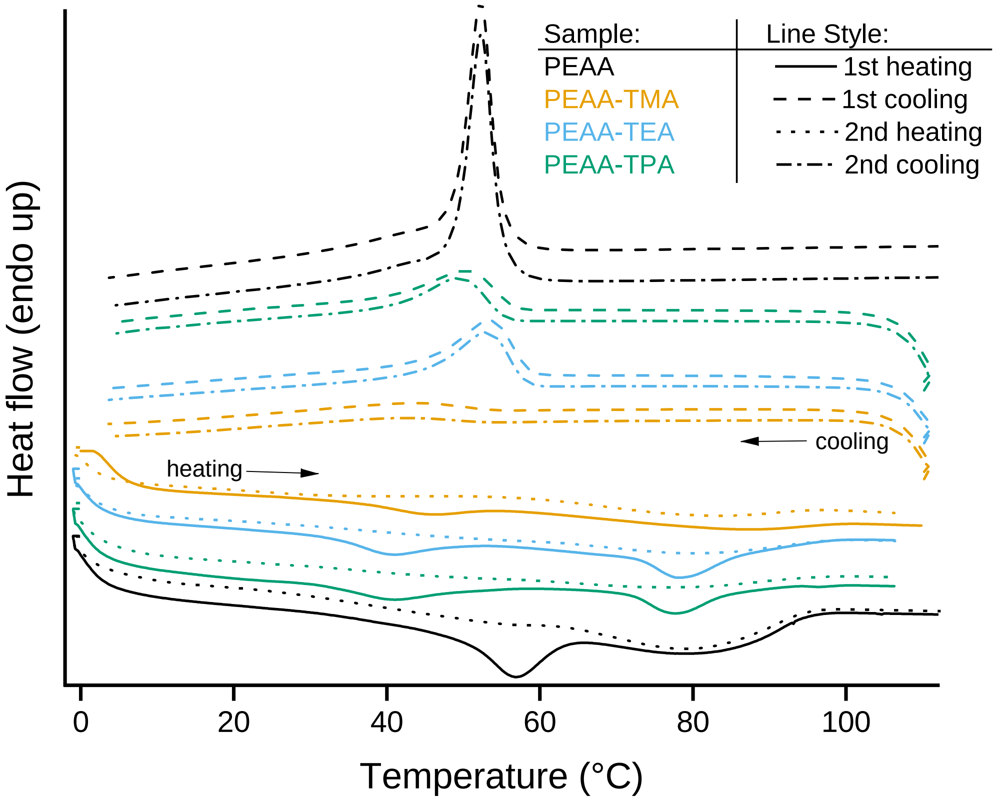

Figure 5.8 DSC thermograms of starting material PEAA, and ionomers PEAA-TMA, PEAA-TEA, and PEAA-TPA. All samples dried in vacuum oven before data collection.

Table 5.1 Influence of counterion identity on ionomer properties and laminate structure response

Polymer*	T_m (°C)^{a,b}	T_d (°C)^{b}	w_{H_2O}^{c}	$H_2O{:}NR_4^{+}$^{d}	log ρ (MΩ·cm)	μ_s	μ_k	E (MPa)	E_R, 0V (MPa)	E_R, 450V (MPa)	ΔE_R (%)^{e}
PEAA	38	–	–	–	>10	–	–	38.1	80.7	71.7	89
PEAA-TMA	43	140	7.0	0.48	5.38	0.8	0.8	20.3	71.5	107	154
PEAA-TEA	39	120	7.9	0.50	5.47	1.2	1.0	3.1	43.1	86.1	200
PEAA-TPA	37	115	6.7	0.41	4.98	1.5	1.3	1.5	30.4	74.1	244

[*] All samples conditioned at 12% relative humidity unless otherwise noted; [a] Determined from half Δc_p; [b] samples dried in vacuum oven at 45 °C; [c] Weight fraction of hydrated sample; [d] moles of water:moles of NR_4^+ ion; [e] Calculated by dividing flexural modulus at 450 V by flexural modulus at 0 V.

The counterion also affected the thermal stability of the polymers. By thermogravimetric analysis it was determined that virgin PEAA was stable to 200 °C (See Appendix D.1 Thermal Data). The deprotonated derivatives, in contrast, showed significant decomposition below 150 °C, where the decomposition temperature decreased with increasing ion size.

5.5.4 Impedance spectroscopy

The resistivity was calculated as a function of frequency from 40 Hz – 110 MHz from the real and imaginary components of impedance as measured using an Agilent 4294A dielectric impedance analyzer. Samples, 170 – 250 µm in thickness, were sandwiched between two polished circular brass electrodes. The real component of conductivity, σ', was calculated from the magnitude of impedance and the phase angle at each sampled frequency as

$$\sigma' = \frac{d\cos\theta}{A|Z|} \tag{5.11}$$

where d is the sample thickness, A is the sample area, θ is the phase angle, and $|Z|$ is the magnitude of impedance (see Appendix D.2 Dielectric Impedance Spectroscopy – derivation and calculations for full derivation). The resistivity was then calculated as the inverse of conductivity, $\rho = (\sigma')^{-1}$. Additionally, the DC resistivity was measured by determining where the slope of resistivity versus frequency is zero, *i.e.*, where resistivity becomes frequency independent (Figure 5.9, black squares).[215]

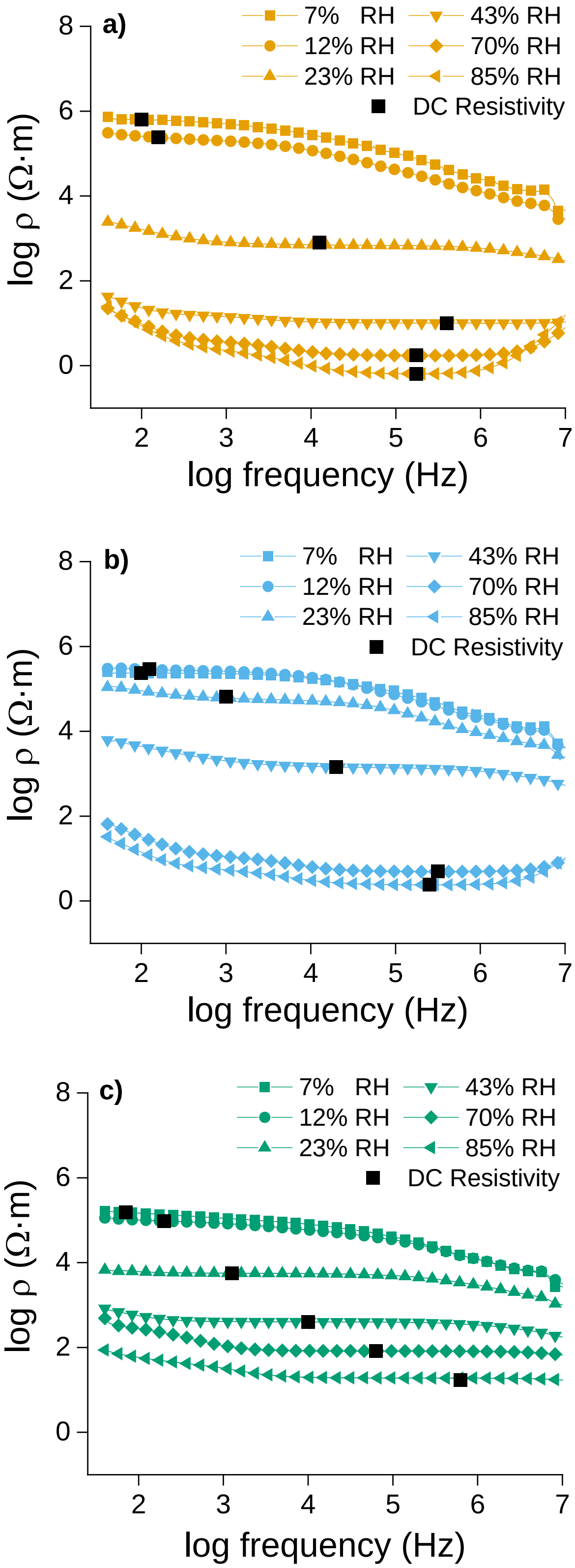

Figure 5.9 Frequency-dependent resistivity of a) PEAA-TMA, b) PEAA-TEA, and c) PEAA-TPA, from 40 Hz to 10 MHz conditioned at various controlled relative humidities.

Relative humidity was found to influence ρ of the ionomers to varying degrees depending on the counterion identity (Figure 5.6b). Although the trends are not simple, it can be seen that all materials experience a dramatic drop in resistivity between the initial humidity value of 7% and 40% which is expected to affect the ability of these polymers to express the JR effect without arcing. The material with the least hydrophobic counterion, PEAA-TMA, showed the fastest decrease in resistivity with increasing relative humidity. Interestingly, the most hydrophobic polymer, PEAA-TPA, after an initial loss of resistivity (between 7 and 40%), proved less sensitive than the other materials to further increases in RH.

5.5.5 Mechanical properties of ionomers

Stress-strain curves were obtained for each of the polymer samples by stretching them in the tensile mode at a constant rate (Figure 5.12). Young's moduli (E) were calculated from the stress-strain curves acquired for each polymer as

$$E = \frac{FL_0}{A_0 \Delta L} \tag{5.12}$$

where F is the applied extensional force, L_0 is the initial gauge length, A_0 is the initial cross-sectional area, and ΔL is the elongation of the sample. The elastic moduli of the polymer samples depended strongly on the identity of the counterion and relative humidity (Figure 5.6c). The decrease in modulus varied proportionally with the size of the counterion with TMA impacting the modulus the least and TPA yielding the softest samples. Not surprisingly, absorbed water plasticized the polymers, causing the most dramatic decreases at low humidities for the least hydrophobic system, PEAA-TMA.

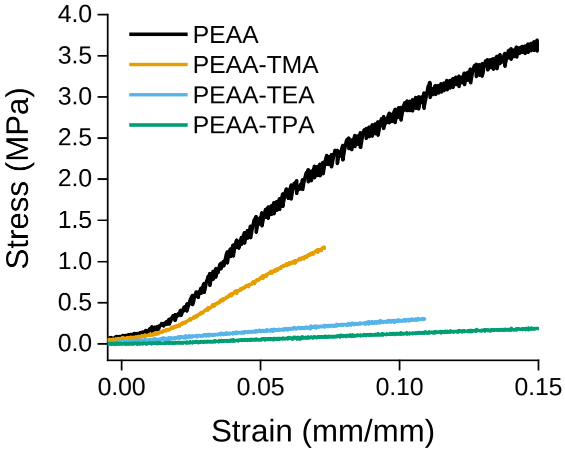

Figure 5.10 Stress vs. strain curves for PEAA, PEAA-TMA, PEAA-TEA, and PEAA-TPA shifted to begin at the origin to account for slack in the sample prior to tension. Slopes from the first two to three strain percent were used for calculation of the elastic moduli and the average and standard deviation of multiple runs were calculated (n = 3-9).

5.5.6 Kinetic coefficient of friction

The kinetic coefficient of friction, μ_k, for polymer-on-polymer surfaces was determined by sliding at a rate of 3.3 mm/min at various applied normal loads from 0-2.5 N after conditioning at 12% relative humidity (Table 5.1, Figure 5.11). The kinetic coefficient of friction increased with increasing counterion size, μ_k = 0.78, 0.98, and 1.33 for PEAA-TMA, PEAA-TEA, and PEAA-TPA, respectively. Increasing alkyl chain length, consistent with plasticizing effects of a larger counterion and resulting softer ionomer, resulted in an increase in the kinetic coefficient of friction with increasing counterion size.

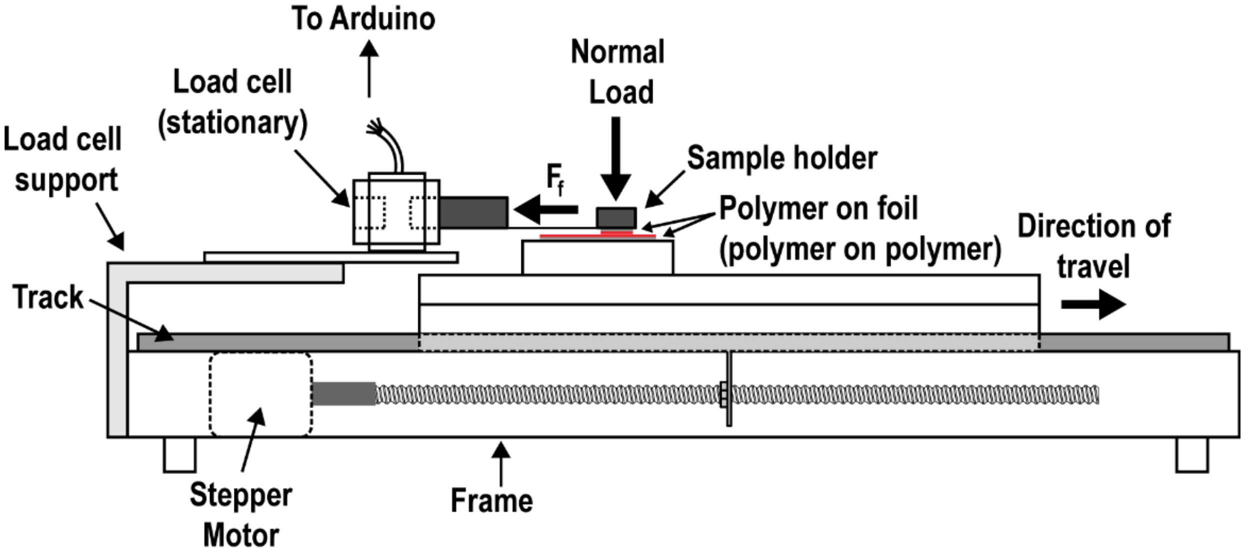

Figure 5.11 Schematic of configuration for measuring polymer-polymer static and kinetic coefficients of friction.

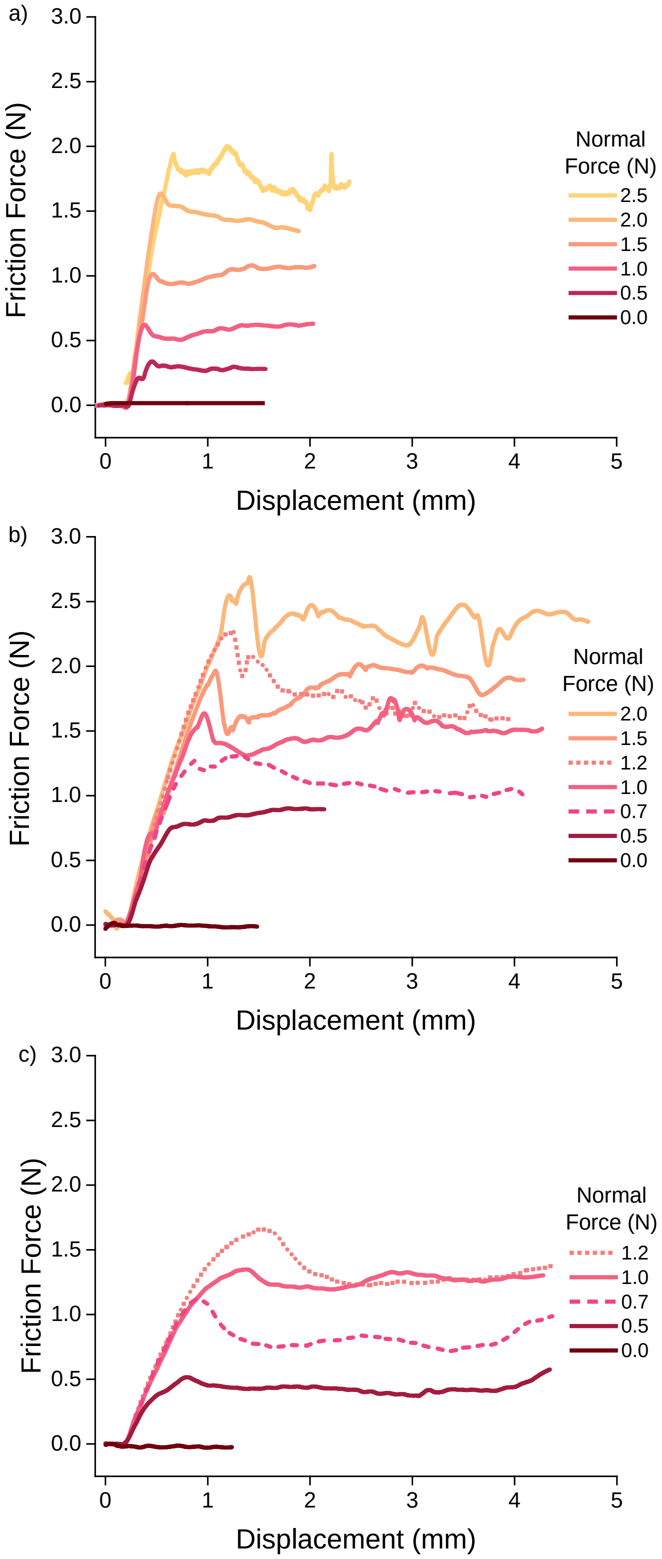

Figure 5.12 Force-displacement curves at various applied normal forces for a) PEAA-TMA, b) PEAA-TEA, and c) PEAA-TPA conditioned at 12% relative humidity.

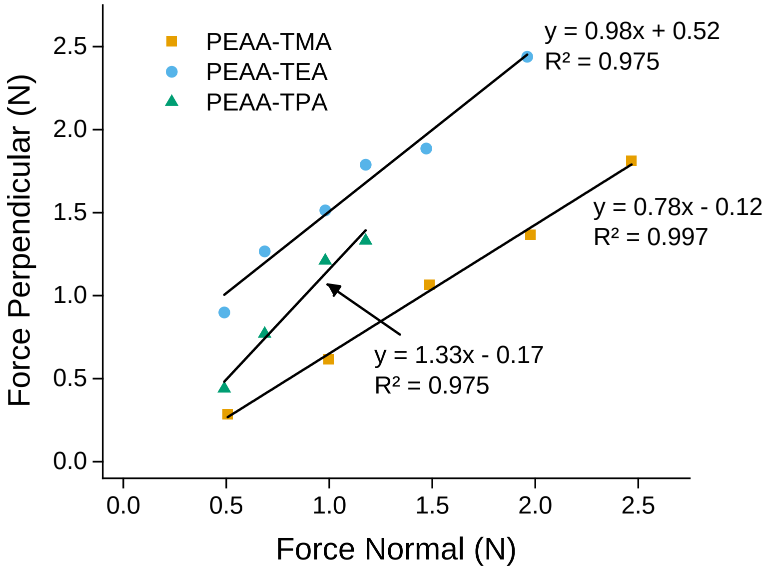

Figure 5.13 Calculation of coefficients of friction, assuming $F_P = \mu_k F_N$, for PEAA-TMA, PEAA-TEA, and PEAA-TPA conditioned at 12% relative humidity.

Roughness. The surface roughness of ionomer samples prepared for electroadhesive tests were investigated with optical profilometry at 5, 10, and 50x magnification. A form correction was applied before computing roughness statistics (either tilt or Gaussian curve correction). The measured roughness was found to depend on the magnification during imaging, decreasing with increasing magnification (Table D.1, Figure D.5-Figure D.13). The rms surface roughness (R_q) for PEAA-TMA, PEAA-TEA, and PEAA-TPA was relatively low, 18, 16, and 37 nm respectively, at 50x optical zoom.

5.5.7 Voltage-dependent structure stiffening

(Data contributed by Colin Ladd)

To measure the effect of the electrically-induced adhesion, a sandwich structure consisting of (E|P)/(P|E) was prepared (E = electrode, P = polymer, Figure 5.14a). The effective flexural modulus of the sandwich structure was obtained under a variety of voltages using a custom-built three-point bending apparatus. Polymer samples (80 mm length x 19 mm width x 1.20 mm total thickness) that had been cast, heat pressed onto aluminum electrodes, and then conditioned at 12% relative humidity for 3 d were assembled into a sandwich structure. The force required to deflect the center of the structure was measured. The effective flexural rigidity, E_{R}, was calculated according to classical beam theory[216]

$$E_{\mathrm{R}} = \frac{L^3 F}{4 b d_{\mathrm{t}}^3 D} \tag{5.13}$$

where L is the span between the supports, F is the applied force, D is the displacement, b is the width of the structure, and d_{t} is the total thickness of the structure.

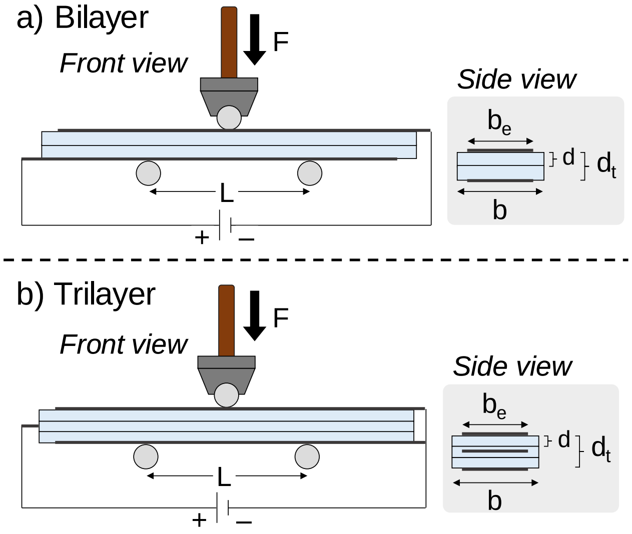

Figure 5.14 Diagram of three-point bending apparatus. Sample is placed on two supports and a force is applied to the center of the sample via a load cell. A power supply is connected to each electrode and a potential is applied prior to sample displacement.

The effective flexural rigidity, which is a function of the adhesion between the polymer layers, was found to depend on the counterion and the applied voltage (Figure 5.14). Consistent with the expected effects of plasticizing the material, the zero voltage flexural modulus decreased with increasing alkyl chain length of the ammonium ion. Upon applying a potential to the system, no significant change is initially observed, with E_{eff} remaining consistent over the first few hundred volts. Around 250-350 V, E_{eff} sharply increases with applied voltage. The samples suffered dielectric breakdown at potentials greater than 450 V for all ionomers under these experimental conditions. Leakage currents decreased as counterion size increased.

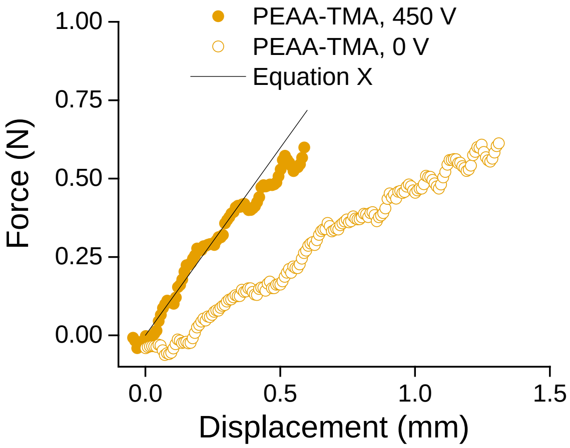

Figure 5.15 Force required to deflect bilayer structure of PEAA-TMA at 0 V and 450 V. Solid line calculated according to eq. (5.13)

As applied voltage increased the ionomers exhibited dramatic stiffening whereas the virgin PEAA control system retained its initial flexibility. Although each material exhibited a different initial modulus, the absolute magnitude of the modulus increase observed was similar and in the range or 36-44 MPa. Normalization with respect to the initial modulus gave increases of 154, 200, and 244% relative to the 0V control for PEAA-TMA, PEAA-TEA, and PEAA-TPA, respectively.

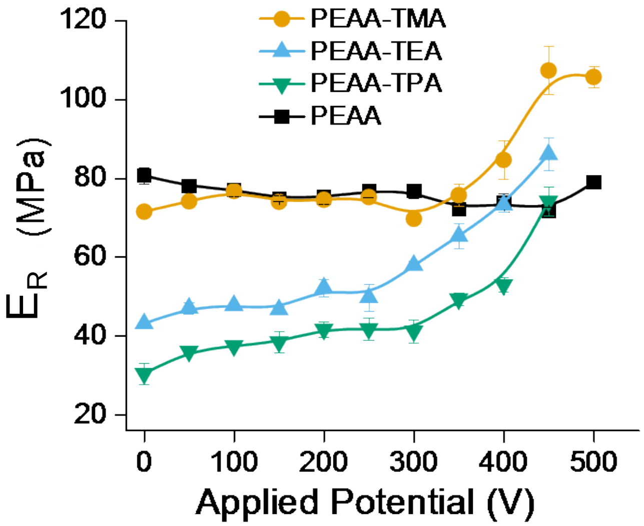

Figure 5.16 Effective flexural rigidity of sandwich structure as a function of applied potential. Error bars represent the standard deviation of the calculated moduli measured in triplicate at each potential.

5.5.8 Trilayer structure stiffening

A three-layer structure composed of (E|P)/(P|E|P)/(P|E) using PEAA-TMA ionomer was also tested at 12% RH to demonstrate the macroscopic response and the effect of layering on the effective flexural rigidity (Figure 5.14b). The initial E_R of the unbiased structure at 0 V was 27 MPa. Upon applying a potential of 450 V, the E_R of the structure increased to 58 MPa, a change of 31 MPa. Figure 5.17 shows a PEAA-TMA three-layer laminate with under a load of 2.5 N. The difference in E_R can be visualized by the deflection of the structure under the same load with and without applied potential.

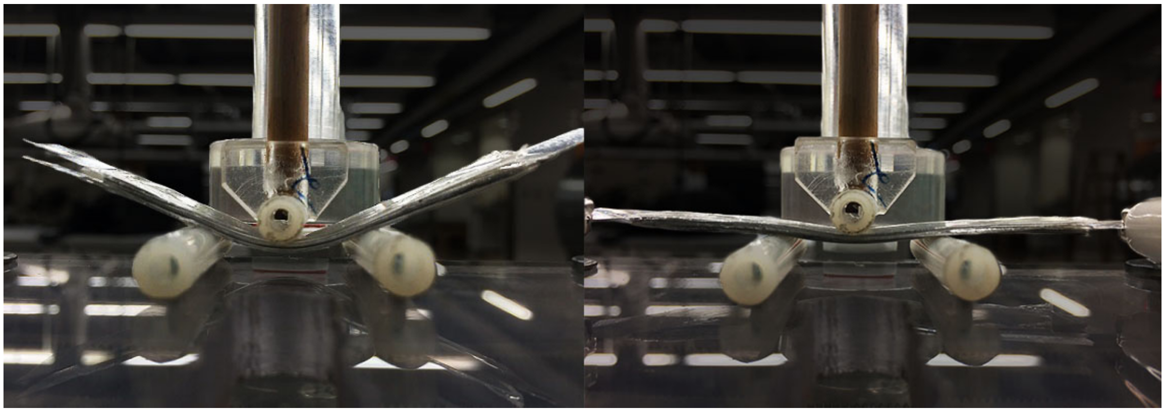

Figure 5.17 Tri-layer PEAA-TMA sample at 12% RH under an applied load of 2.5 N at 0 V (left) and 450 V (right) applied potential.

5.6 DISCUSSION

5.6.1 Counterion-dependent properties of the ionomers

The morphology and thermal behavior of the polymers shows a strong dependence on counterion as is expected. The acid precursor, PEAA, is a semicrystalline polymer.[213] The exchange of protons for the bulky tetralkylammonium ions disrupts the crystalline regions.[217] The T_gs' of the tetraalkylammonium ion series follows the expected trend--as alkyl chain length of the counterions increases, the glass transition temperature decreases.[218-219] Larger counterions (TMA^+ = 0.28 nm, TEA^+ = 0.34 nm, TPA^+ = 0.38 nm)[220] increase free volume of the polymer while simultaneously distributing the positive charge on the ion over a larger volume which weakens the ionic crosslinks. Although all three tested materials absorbed substantial water as a function of % RH. the degree depended on the counterion. The mass of water absorbed as a function of polymer weight would be expected to depend primarily on two factors 1) The degree of association between the pendant anion and the counterion which would be expected to decrease with size such that the TPA-neutralized ionomer should absorb the most water and 2) the hydrophobicity of the sample, as reflected in the density of ions. By this argument, the TPA sample, which will have the lowest density of ions by weight due to the higher MW of the ion, should absorb less water overall. Given the observed trend, hydrophobicity appears to be the dominating factor.

The effects of neutralization were also directly reflected in the mechanical properties of the materials. Virgin PEAA was significantly stronger than any of the ionomers, due to the presence of crystalline domains and a less plastic polymer matrix.[221] For the tetraalkylammonium neutralized materials, the modulus of PEAA-TMA was substantially higher than those of either the TEA- or TPA-neutralized ionomers. The elastic modulus of the PEAA-TMA decreased as a function RH, however, while the other two ionomers changed little.

The dependence of the pattern of resistivity observed for the ionomers is not simple as the movement of ions/electrons depends on T_g, the intrinsic mobility of the cations themselves, and the water concentration. One overall trend does emerge. All materials exhibit a decrease in resistivity as a function of increased humidity. TMA which both absorbs more water and plasticizes to a greater degree, exhibits the most dramatic drop and ultimately leads to the most conductive material. In contrast, the resistivity of PEAA-TPA, which bears the least coordinating ion, drops quickly initially but eventually levels out at a higher resistivity than the other two samples at high RH.

5.6.2 Structure stiffening

The PEAA-tetraalkylammonium ionomer laminates described herein are capable of quickly changing mechanical properties under an applied potential. As determined by flexural rigidity measurements, assuming a fully bonded laminate material (to aid in the ease of comparing on/off states), the change in E_R for the bilayer structures does not depend strongly on identity of the counterion at a fixed relative humidity (12% RH). The baseline flexural rigidity, however, was found to depend significantly on the counterion identity, decreasing with increasing counterion size, consistent with plasticization effects associated with longer counterion alkyl chain lengths. The range over which E_R may be tuned is then determined by the counterion's influence on the baseline mechanical properties of the ionomer, which offers a new route to tune the mechanical properties on an electroadhesive systems outside of changing the polymer identity entirely. The E_R did not respond strongly to the applied potential until ~ 300 V, where E_R began to increase steadily.

The E_R of the laminates, while increasing substantially under an applied voltage of 450 V, did not exhibit the four-fold increase that is predicted by beam theory for a fully bonded bilayer structure. This deviation is not surprising since this model treats O V control as fully unbonded (Case 1, as described in the introduction) when, in reality, the measured E_R under no voltage must necessarily include the inherent adhesion between the two layers. These fundamental adhesions are expressed in this bending experiment as coefficients of friction because the shear stress transfer between layers depends upon the applied normal force, in this case arising from the electroadhesive force, and the coefficient of friction between the contacting polymer surfaces as $F_P = \mu F_N$. As such the 0 V control experiments fall under Case 2 and do not represent the ideal fully unbonded scenario. Moreover, the state of the system under 450 V cannot be confidently labeled as a higher degree of bonding Case 2 or fully-bonded Case 3 because, in part, sample arcing prevents the collection of data past 450 V. Despite these limitations, the relative roles of the tetraalkyl counterions in determining the adhesion behavior can clearly be seen and compared.

5.7 CONCLUSIONS

In conclusion, we have reported the first systematic investigation on the effect of counterion identity in ion containing electroadhesive systems. Unlike previously studied structures, these polymers achieve electroadhesion using the Johnsen-Rahbek mechanism rather than typical coulombic forces. This mechanism has been shown to depend on the material properties that are affected by the identity of the counterion used to neutralize the ionomer; namely the glass transition temperature, electrical resistivity, and elastic modulus. The degree of electroadhesion, and thus the stiffness, for each structure can be controlled by changing the potential applied across the system.

5.8 MATERIALS AND METHODS

5.8.1 Materials

Poly(ethylene-*co*-acrylic acid) (PEAA) 20 wt.% acrylic acid (M_w = 41 kDa, 9 mol% AA), a 25 wt.% aqueous tetramethylammonium hydroxide (TMAH) solution, a 25 wt.% aqueous tetraethylammonium hydroxide (TEAH) solution, a 25 wt.% aqueous tetrapropylammonium hydroxide (TPAH) solution, and a 40 wt.% aqueous tetrabutylammonium hydroxide (TBAH) solution were purchased from Sigma-Aldrich and used as received. Aluminum shim stock 0.1 mm thick was purchased from McMaster-Carr.

5.8.2 Neutralization of PEAA

A typical neutralization was carried out following a procedure adapted from Cipriano and Longoria (Scheme 5.1).[222] PEAA (10.0 g, 27.8 mmol AA) and an aqueous solution of tetramethylammonium hydroxide (25% w/w, 10.2 g, 28.0 mmol TMAH) were combined in a round-bottom flask. To the flask, 100 mL of dH_2O was added and the mixture was stirred and heated at 70 °C until the PEAA beads dissolved, indicating neutralization of the acrylic acid was complete (about 12 h). The solution was concentrated in a hot water bath to a final concentration of ~250 g/L. Neutralizations with TEAH and TPAH proceeded similarly. Due to TBAH's propensity to crystallize below 30 °C, attempts at obtaining homogenous samples were unsuccessful.

5.8.3 Size-exclusion chromatography

Relative molecular weight of unneutralized PEAA was determined on a Waters Gel-Permeation Chromatograph with a Waters 2414 refractive index detector. PEAA was dissolved in THF at a concentration of ~1 mg/mL and was filtered prior to injection. 100 uL was injected into the column and the resulting molecular weight was calculated with reference to polystyrene standards (1-500 kDa).

5.8.4 Fabrication of ionomer-electrode samples

A strip of aluminum 1 cm wide by 7.5 cm long was cut from sheet stock (80 µm thickness) and the edges were filed to remove any burrs that could interfere with coating. The strip was then polished with hexanes and acetone and clamped to a smooth high density polyethylene plate. A thick bead of ionomer solution was applied across the width of the strip and a pulldown bar was drawn down the length of the strip in one smooth motion. Pulldown bars with spacings of 0.17 mm, 0.34 mm, and 0.75 mm were utilized to fabricate samples of consistent thickness by subsequently drawing down polymer solution with increasing pulldown bar spacing until the total thickness of the sample reached approximately 0.60 mm. Between each application of the polymer solution, the entire plate was transferred to a 60 °C oven until the solution became slightly tacky. Following the final application of solution, the plate was transferred to the oven until the sample was dry to the touch. The sample was then physically removed with a razor blade and excess polymer was trimmed to within 3-4 mm of the electrode. Typical final sample dimensions were 80 mm x 19 mm x 0.61 mm. Polymer surfaces were hot pressed using a glass plate at 50 °C to a final thickness of 0.60 mm, total structure thickness 1.20mm.

5.8.5 Flexural modulus measurements

Relative humidity was controlled using saturated aqueous salt solutions according to ASTM E104. Prior to data collection, each sample was dried in a vacuum oven and conditioned in a sealed vessel containing a saturated LiCl solution (12% relative humidity) for three days to ensure a consistent water content.[223] Force-deflection measurements of both unbiased and biased samples were carried out on a custom-built computer-controlled three-point bending apparatus. All measurements were made using a 25.4 mm span. A stepper motor displaced the sample at a constant rate 1 mm/min and the force required to bend the sample was recorded with a 10 lb compression load cell. Measurements were obtained in a dry nitrogen atmosphere to prevent the atmospheric wetting of the surface of the sample. Force vs. displacement curves were plotted and the slope of the resulting line was used to calculate the effective flexural modulus of the sample as per classical beam theory.[224] Each measurement was taken in triplicate in order to determine reproducibility of the process. Biased samples were tested by sandwiching the structure between two glass slides (25 mm x 75 mm x 1 mm) and applying a 1 N preload force to ensure intimate contact of the surfaces prior to applying a potential. The glass slides were removed and the deflection of the sample was measured as before. For each subsequent test, prior to applying potential the sandwich structure was separated in order to dissipate any residual adhesion and provide a fresh interface for charging.

5.8.6 Friction measurements

Polymers samples were cut from films made using the draw down bar method on aluminum foil as described in fabrication of ionomer-electrode samples above. A square sample ~70 mm x 70 mm was cut from the polymer/foil film and the electrode side affixed to a holder using doublesided tape. The polymer-polymer surfaces were placed in contact and a series of normal forces, F_N, were applied (0-2.5 N). The perpendicular force, F_P, was measured at 90° from normal during sliding at a constant velocity of 3.3 mm/min (Figure 5.11). The kinetic friction force, F_k, was determined from the plot of F_P vs displacement, when F_P remained constant after static friction was overcome. The kinetic coefficient of friction was then calculated from the slope of F_k versus F_N, assuming $F_P = \mu_k F_N$.

5.8.7 Young's modulus

The elastic modulus of each polymer was determined using an ADMET MTESTQuattro mechanical tester in tensile mode. Using a cutter fashioned according to ASTM D638 – Standard Test Method for Tensile Properties of Plastics, dumbbell samples with length 35 mm, gauge 14.75 mm, width 3 mm, and uniform thickness ranging from 0.1-0.3 mm were cut from drop cast films. Films were prepared in polystyrene petri dishes and oven dried at 60 °C before cutting. Samples were then conditioned at 7, 12, 23, 43, 70, or 85% RH for 2 days prior to testing. Samples were elongated at a constant rate of 10 mm/min and the tensile modulus was calculated by taking the maximum slope of the initial stress-strain curve over a 2% strain range. Reported moduli are the average of 2-3 specimens per each polymer.

5.8.8 Water content

Wet samples conditioned at various relative humidities for mechanical testing were weighed (0.1-0.2 g per sample) and dried in a vacuum oven at 45 °C for 3 days. Before and after drying, FTIR spectra were collected for all samples to determine if samples of the same ionomer series had the same water content after drying. The mass fraction of water was determined by dividing the change in mass by the wet mass of polymer. The mole fraction of water per counterion was determined by assuming dried samples did not contain any residual water.

5.8.9 Optical profilometry

Polymer samples were prepared as described for friction measurements and in fabrication of ionomer-electrode samples above. All surface measurements were taken with a Bruker ContourGT optical profilometer and analyzed with BrukerReader software. Optical images and surface profiles were obtained at three magnifications, 5, 10, and 50x and roughness statistics computed after applying either a tilt or Gaussian curvature correction, depending on the magnification (See Appendix D.4 Optical Profilometry Data).

5.8.10 Differential scanning calorimetry

Thermal properties of each polymer were evaluated by differential scanning calorimetry. About 4 mg of polymer was conditioned to dryness in a vacuum oven kept at 50 °C overnight. The sample was transferred to an aluminum DSC pan and hermetically sealed to prevent the uptake of water. The sample was subjected to two heating cycles from 0 °C to 70 °C at 10 °C/min and the glass transition temperature was determined from the second heating cycle. Measurements were performed on a Perkin Elmer DSC 6000 calibrated with indium metal.

5.8.11 Impedance spectroscopy

Dielectric impedance spectroscopy was performed using an Agilent 4294A impedance analyzer. Samples for impedance measurements were fabricated by first drop casting a free-standing polymer film on a glass plate in an oven at 60 °C followed by hot pressing the partially dried polymer at 90 °C to obtain a uniform surface and thickness (170-250 μm). Samples were vacuum oven-dried and conditioned at various relative humidities as described for the water uptake experiment above. The obtained polymer films were sandwiched between two polished brass electrodes (6.47 mm diameter) and the real and imaginary impedance obtained over the frequency range of 40 Hz to 110 MHz at RT.

5.8.12 Thermogravimetric analysis

Thermal degradation data was collected on a TA Instruments TGA Q500. Approximately 15 mg of sample was loaded into a tared platinum pan and the percent mass change was measured over the course of each run (See Appendix D.1 Thermal Data). The temperature was ramped from 20 °C to 200 °C at 2 °C/min under a constant flow of nitrogen (60 mL/min).

6.0 CONCLUSIONS

Materials and structures typically remained fixed in their mechanical properties once prepared. Here, two techniques were presented with which the mechanical properties of a polymeric system or structure may by modified using electricity. In the first project, the use of redox chemistry to alter the crosslink density of hydrogel materials containing electrochemically labile metal-ligand coordination using copper or iron was described. Copper hydrogels were electrochemically reduced from hard to soft states. Electrochemical oxidation was impeded by the formation of a skin layer on the electrode, limiting diffusion of copper ions to and away from the electrode surface. These materials have excellent shape memory properties and could also be electrochemically patterned with distinct soft and hard regions.

The second metal-based system using iron was found to be electrochemically reversible between soft and hard states. Diffusion limited processes dictated long electrochemical transition times. The inclusion of graphene oxide within these materials improved their mechanical properties. Decreasing sample thickness from 3 mm to ~100 µm decreased the metal ion diffusion distance and the transition time between soft and hard states from many hours to minutes. The modulus range was also improved with the inclusion of GO. Potentiometric titrations established complex formation between Fe^{3+} and carboxylate ligands of the hydrogels whereas Fe^{2+} showed little to no coordination. Mössbauer spectroscopy established high spin iron in both +2 and +3 oxidation states. Magnetic susceptibility measurements suggested the formation of polynuclear iron clusters within the hydrogels.

The final project focused on using electricity to reversibly pin the layers of multi-layered laminate structures using electroadhesion. Structure-function relationships for a series of tetraalkylammonium ionomers prepared from poly(ethylene-co-acrylic acid) were investigated at a range of relative humidities. The counterion was found to have little influence on the electroadhesive response. The counterion was found to influence the baseline mechanical properties of the structure, with larger alkyl chains plasticizing the polymer resulting in softer materials. The resistivity, moduli, and thermal properties of these ionomers were found to depend on the relative humidity at which the materials were conditioned. The degree of electroadhesion, and thus the stiffness, for each structure can be controlled by changing the potential applied across the system.

While the materials presented in the first project, which utilize metal-ion based reversible crosslinks, provide an elegant example of stimuli-responsive materials with reversibly switchable mechanical properties, practical application of these hydrogels is limited. As the electrochemical process is diffusion-limited thin samples are required for fast transition times. The redox-based mechanism also requires the use of an acidic solvent reservoir containing Fe^{2+} to maintain a high concentration of iron in the gel when switching between hard and soft states. The solvent reservoir presents a larger hurdle to practical applications as containing liquid electrolyte and hydrogel would require a cumbersome containment system. The liquid electrolyte could be eliminated by preparing a hydrogel with two distinct halves. One half would contain the typical hydrogel preparation while the second half would be composed of crosslinked poly(sodium styrene sulfonate) (PSS), which does not coordinate iron ions. In this configuration, the crosslinked PSS would be saturated with iron ions which may freely diffuse through the PSS network and participate in redox reactions, providing charge balance without contributing to a change in modulus as no crosslinking occurs.

The electroadhesion-active laminate structures composed of polymeric ionomers presented in the second project present a significant advancement in the development of materials and structures with electrically reversible mechanical properties. These structures do not require solvent, have nearly instantaneous response times, have higher flexural moduli in both on and off states, and show a greater change in modulus between on and off states. Additionally, the range of flexural moduli accessible may be quickly expanded by simply increasing the number of layers in the laminate structure. In the current iteration presented here, flexural modulus changes are presented from soft to hard states. In applications, the reverse direction may be more desirable. As the power requirement for maintaining electroadhesion is relatively low (e.g. a few mW for several hours), continuous application of electrical potential is not impractical, even for remote applications. However, since these ionomers are sensitive to water content, these structures do require proper environmental conditions for operation, specifically the proper relative humidity. Further development of materials which show greater insensitivity to environmental conditions are needed to advance the use of materials utilizing the Johnsen-Rahbek effect for electroadhesive laminate structures.

Appendix A

SUPPORTING INFORMATION FOR CHAPTER 2

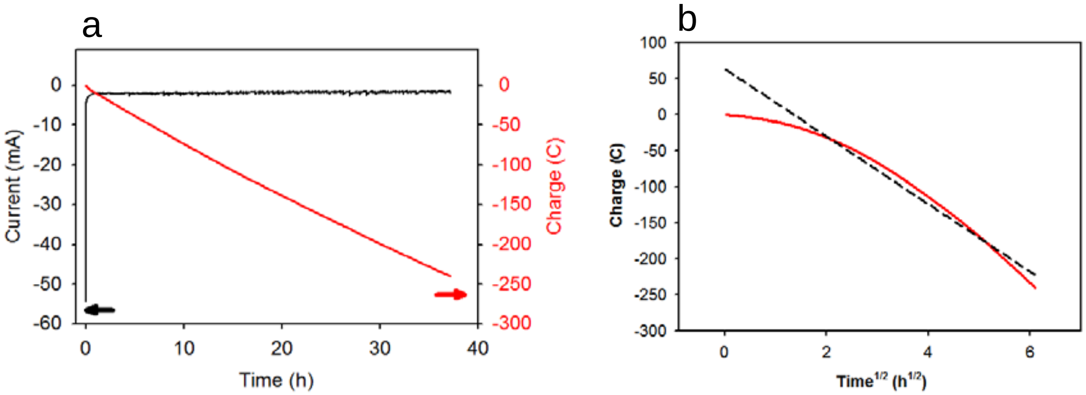

Figure A.1 (a) Chronoamperometric and chronocoulometric curves for the third segment of the first reduction at -0.8 V of an ~2 mm thick iron-doped hydrogel. The hydrogel color change from red-orange to light orange/yellow was consistent with reduction. (b) Charge vs. square root of time. Linear fit of data (dashed line) shown for reference.

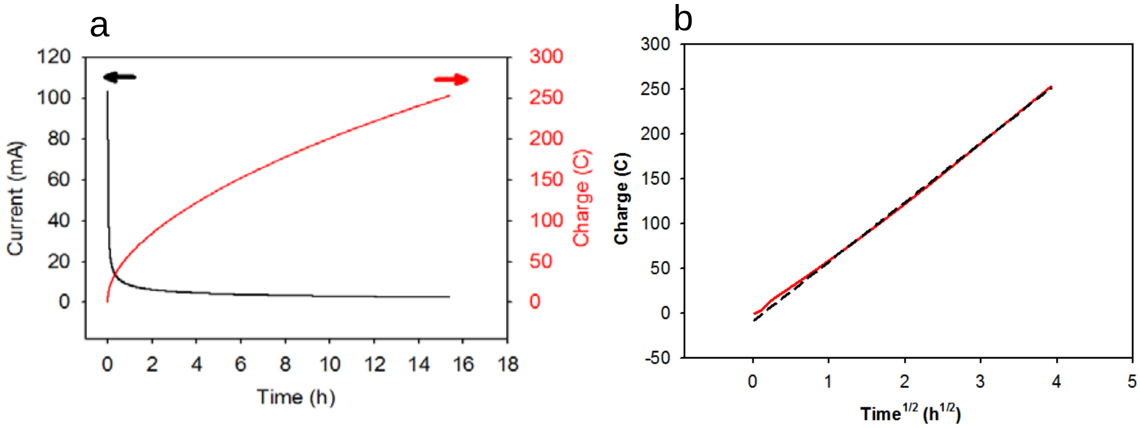

Figure A.2 (a) Chronoamperometric and chronocoulometric curves for the first oxidation at +1.2 V of an ~2 mm thick iron-doped hydrogel. The hydrogel was homogeneously darker orange and stiffer to the touch (confirmed by mechanical testing) than that observed in the previous cycle. (b) Charge vs. square root of time. Linear fit of data (dashed line) shown for reference.

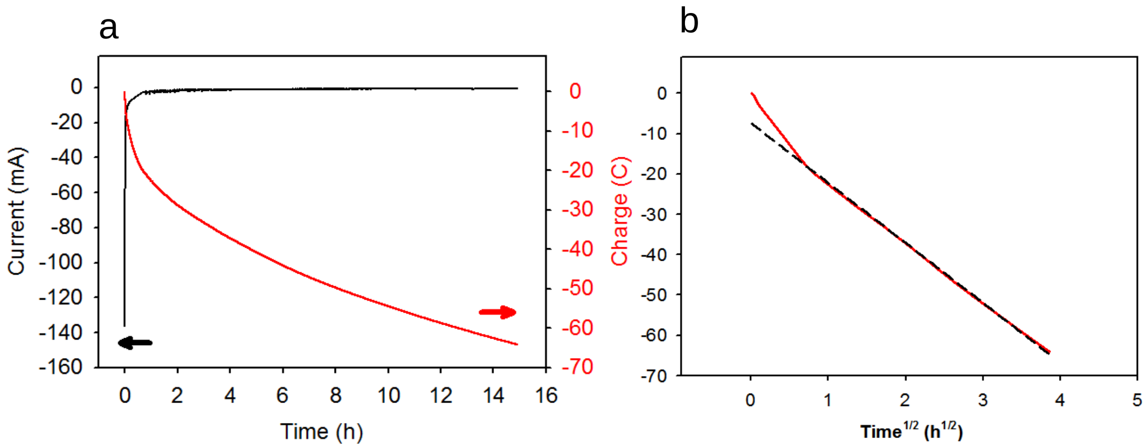

Figure A.3 (a) Chronoamperometric and chronocoulometric curves for the second reduction at -0.8 V of an ~2 mm thick iron-doped hydrogel. Color change from darker to lighter orange/yellow (with some heterogeneity). The sample was softer to the touch (confirmed by mechanical testing) than that observed in the previous cycle. (b) Charge vs. square root of time. Linear fit of data (dashed line) shown for reference.

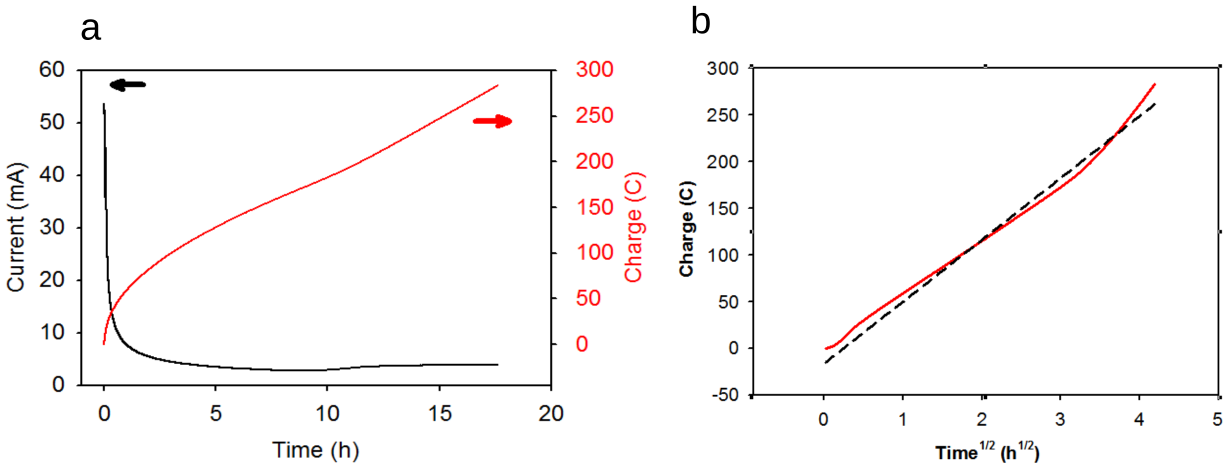

Figure A.4 (a) Chronoamperometric and chronocoulometric curves for the second oxidation at +1.2 V of an ~2 mm thick iron-doped hydrogel. The hydrogel was homogeneously darker orange and stiffer to the touch (confirmed by mechanical testing) than that observed in the previous cycle. (b) Charge vs. square root of time. Linear fit of data (dashed line) shown for reference.

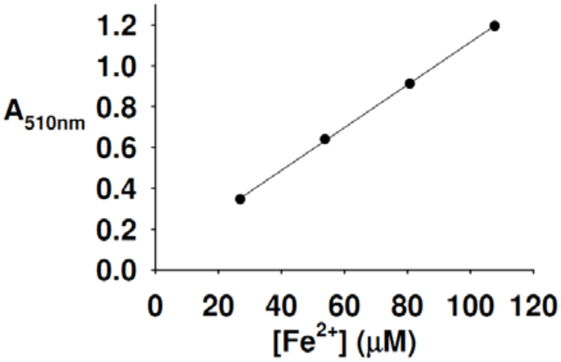

Figure A.5 Calibration curve of $FeCl_2$ standards (0.025 M, in conc. HCl) diluted in sodium acetate buffer (0.1 M, pH=4) to the linear range of the instrument.

Appendix B

SUPPORTING INFORMATION FOR CHAPTER 3

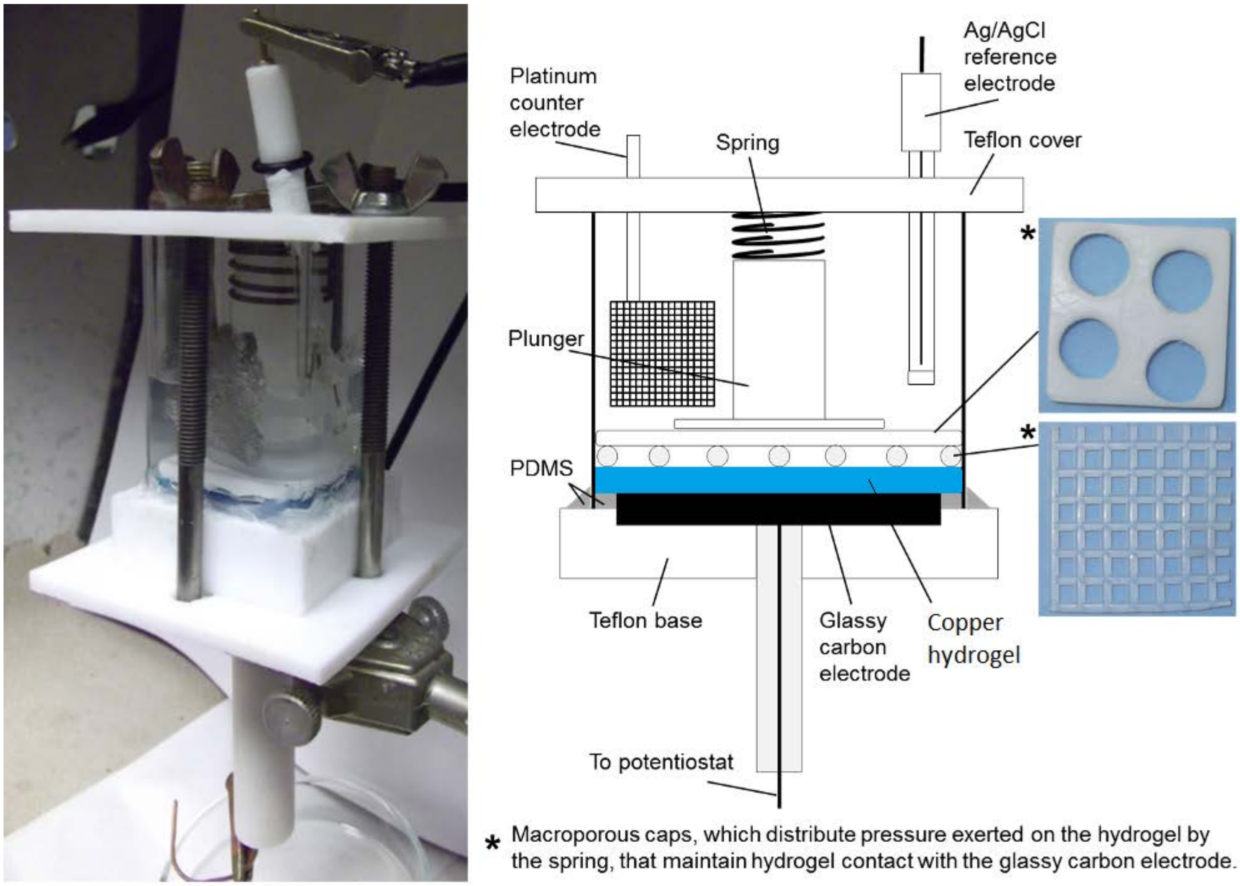

* Macroporous caps, which distribute pressure exerted on the hydrogel by the spring, that maintain hydrogel contact with the glassy carbon electrode.

Figure B.1 Left: Photograph of electrochemical setup. Right: A diagram of the components for the electrochemical setup.

Figure B.2 A diagram of nine samples doping with different concentrations of copper and urea to determine the optimum concentration for future doping experiments.

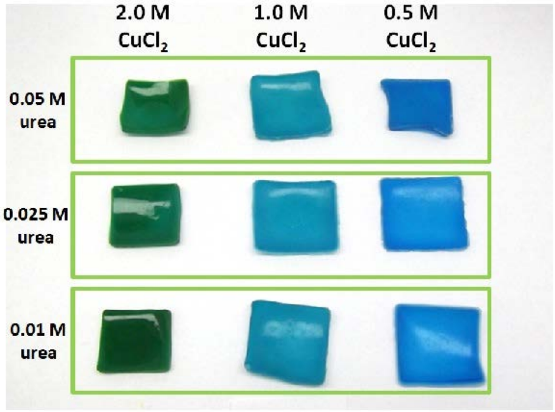

Figure B.3 A 3 x 3 array of hydrogels that gives an indication of the optimum concentrations of $CuCl_2$ and urea necessary for successful doping conditions.

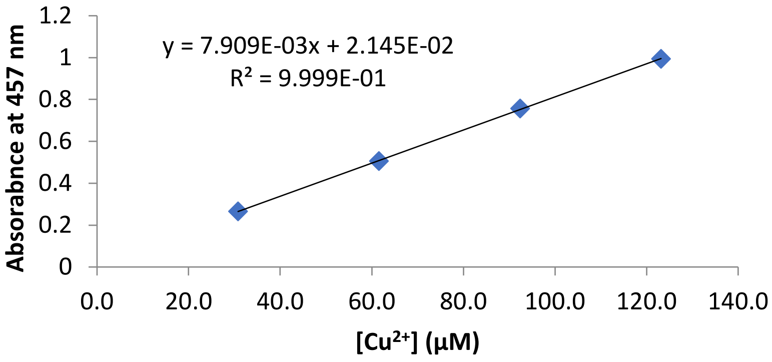

Figure B.4 Calibration curve for copper quantitation method.

Appendix C

SUPPORTING INFORMATION FOR CHAPTER 4

C.1 GRAPHENE OXIDE CHARACTERIZATION

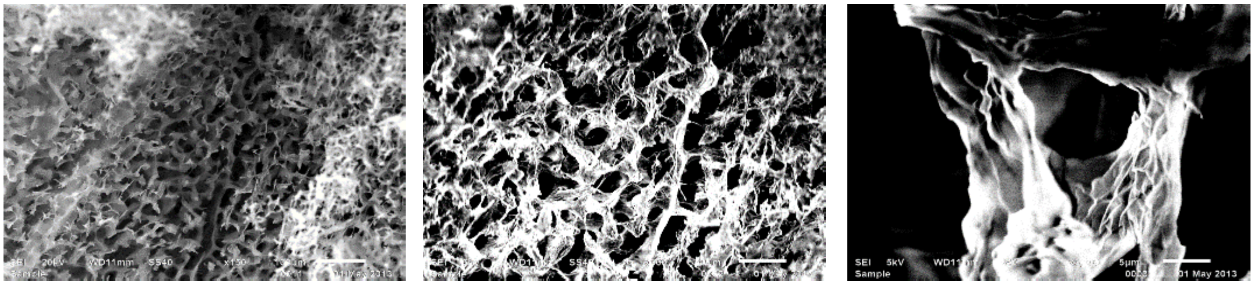

Figure C.1 Scanning electron microscopy (SEM) images of lyophilized GO dispersion (12.5 mg/mL) at different magnifications.

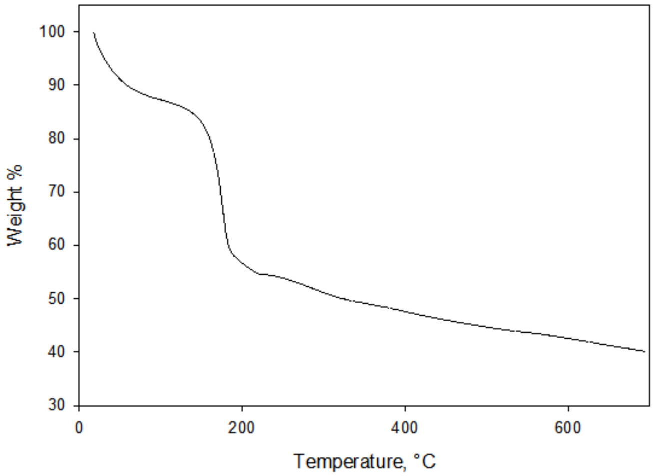

Figure C.2 Thermogravimetric analysis of graphene oxide (GO).

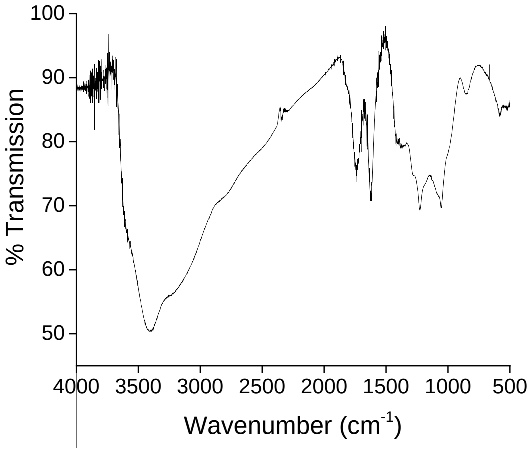

Figure C.3 Fourier Transform-IR (FT-IR) spectrum of GO.

Thermogravimetric analysis (TGA) of graphene oxide (GO, Figure C.2) showed a mass loss of *ca.* 14% below 100ºC, likely due to loss of water. Another sharp mass loss of ca. 30% was observed at 180º C and was assigned to the thermal decomposition of oxygenated functional groups in GO. The FT-IR spectrum of GO (Figure C.3) showed peaks attributable to water, C=O, and C-O groups.

C.2 GRAN PLOT METHOD

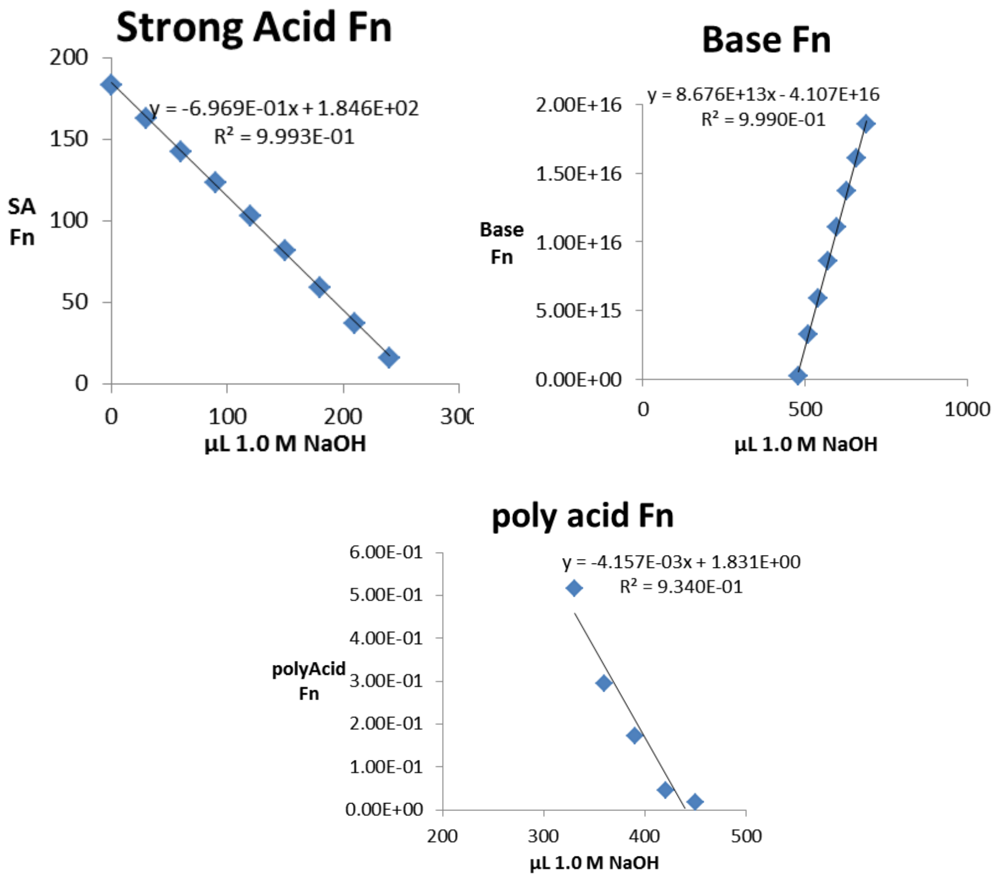

Figure C.4 Gran plots for the determination of strong acid, total acid, and weak acid content of the OR-gel measured in 0.1 M KNO_3.

The carboxylic acid content of the OR-gel was determined by potentiometric titration and analyzed using the Gran plot method.[163] The OR-gel was washed with dH_2O and acidified with excess 1 M HCl and neutralized with 1 M NaOH. The excess strong acid was determined by plotting the following equation (strong acid fn)

$$(V_0 + V) \cdot 10^{-pH} \tag{C.1}$$

where V_0 is the initial volume of the titration and V is the volume of base added, against the total volume of base added. The y-intercept was taken as the total volume of base required to neutralize the strong acid in the system. Similarly, the weak acid content could be estimated by plotting (weak acid fn)

$$V \cdot 10^{-pH/n} \tag{C.2}$$

where n is an empirical constant, against the total volume of base added. Finally, the total acid of the system was determined by plotting (base fn)

$$(V_0 + V) \cdot 10^{pH} \tag{C.3}$$

against the total volume of base added. The difference between the y-intercepts of the base function and the strong acid function gives the weak acid content of the system.

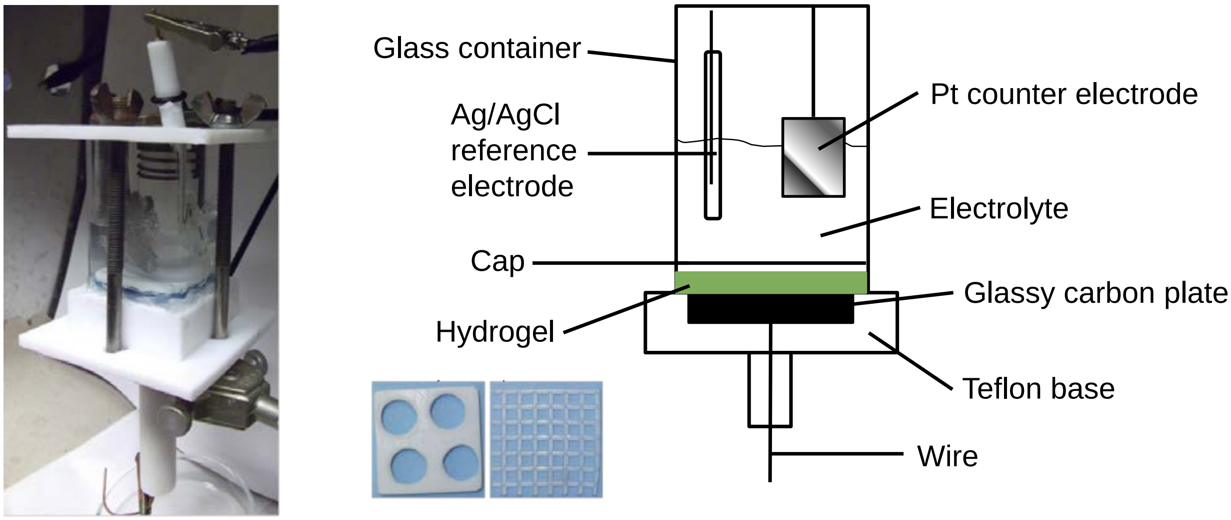

Figure C.5 Electrochemical cell design. **Left:** Experimental setup and **Right:** schematic of cell. Reproduced from.[58]

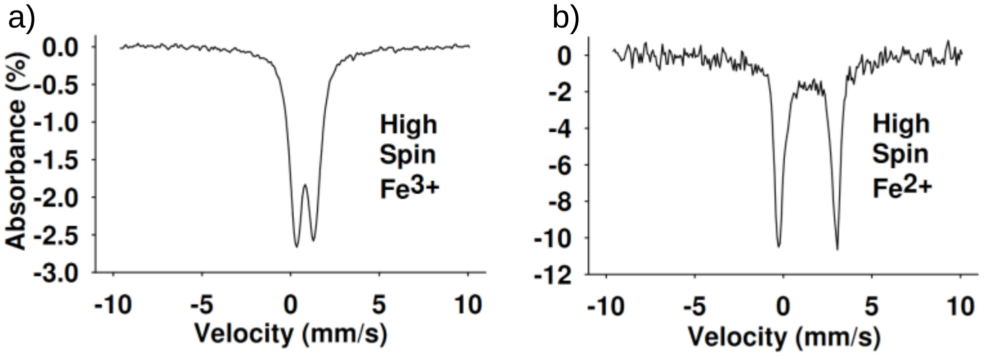

Figure C.6 Mössbauer spectra of a) **Fe^{3+}-gel** prepared by electrochemical oxidation of **Fe^{2+}-gel** and b) **Fe^{2+}-gel** prepared by electrochemical reduction of **Fe^{3+}-gel**. Reproduced in part from.[58]

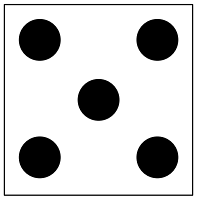

Figure C.7 Approximate indentation testing locations on hydrogel 25 mm x 25 mm, one test per corner and one at center. Probe diameter, 6.2 mm.

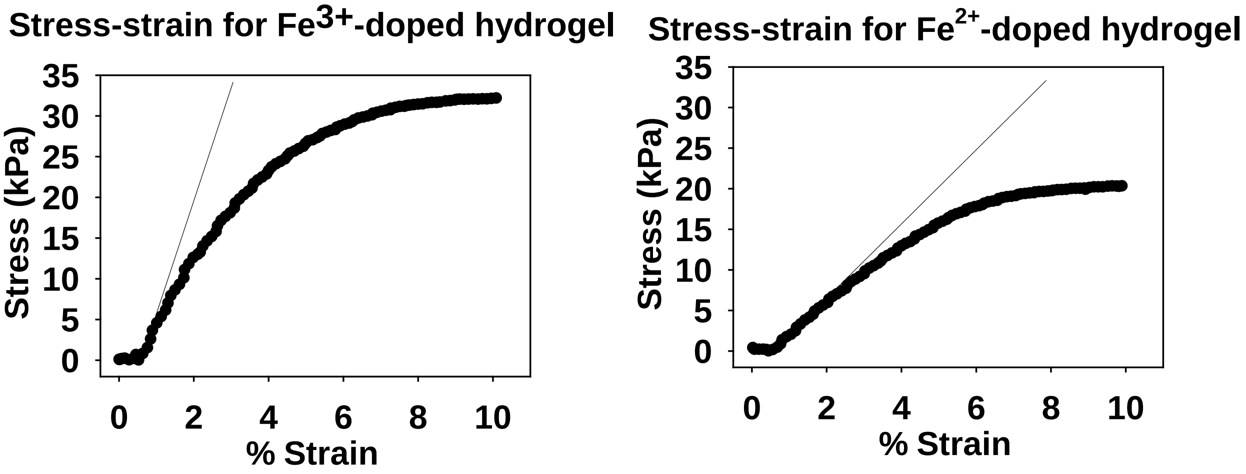

Figure C.8 Indentation test stress-strain curves for **Fe^{3+}-gel** (left) and **Fe^{2+}-gel** (right); straight line represents region of curve from ~0 to 1-2 % strain where slope was measured to determine modulus.

Appendix D

SUPPORTING INFORMATION FOR CHAPTER 5

D.1 THERMAL DATA

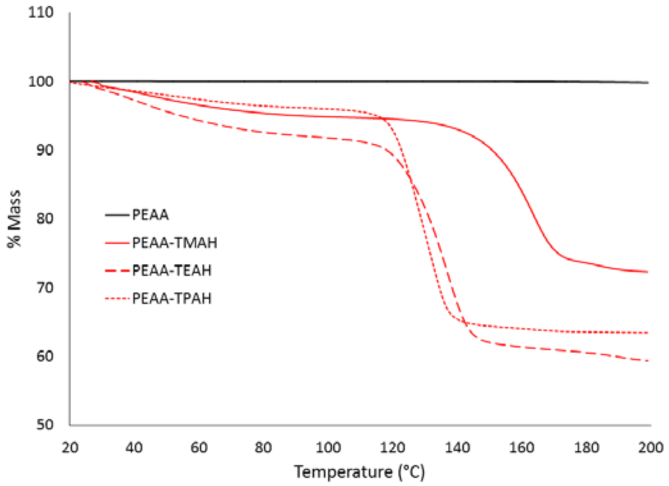

Figure D.1 Mass-loss plots were obtained for each sample by loading 15 mg into a platinum pan and ramping the temperature from 20 °C to 200 °C at 2 °C/min. PEAA shows no change in mass, while the neutralized ionomers exhibit significant mass loss after ~120 °C, most likely due to decomposition and production of an amine.

D.2 DIELECTRIC IMPEDANCE SPECTROSCOPY – DERIVATION AND CALCULATIONS

Dielectric impedance data were collected using an Agilent 4294A dielectric impedance analyzer over the frequency range of 40 Hz – 110 MHz. Samples 170 – 250 μm in thickness were sandwiched between polished brass electrodes. The resistivity was calculated from the real and imaginary components of impedance as detailed below. Here, * is used to denote a complex quantity, e.g. the complex impedance is given by $Z^* = Z' + iZ''$, where Z' is the real component of impedance, Z'' is the imaginary component of impedance and $i = j = \sqrt{-1}$. The complex impedance is also commonly represented as

$$Z^* = R + iX \tag{D.1}$$

where R is the resistance (real component of impedance) and X is the reactance (imaginary component of impedance).

The real resistivity, ρ', can be derived the complex admittance, Y^*,

$$Y^* = \frac{1}{Z^*} = G + iB \tag{D.2}$$

where G is the conductance and B is the susceptance. We can rewrite the admittance in terms of the magnitude of impedance, $|z|$, and the phase angle, θ as follows:

$$Y^* = \frac{1}{|Z|cos\theta + i|Z|sin\theta} \tag{D.3}$$

where the magnitude of impedance is given by:

$$|Z| = [(Z')^2 + (Z'')^2]^{\frac{1}{2}} \tag{D.4}$$

The magnitude of impedance as a function of frequency is shown in Figure D.2 for PEAA-TMA at different relative humidities.

Multiplying the numerator and denominator by $|Z|cos\theta - i|Z|sin\theta$:

$$Y^* = \frac{(|Z|cos\theta - i|Z|sin\theta)}{(|Z|cos\theta + i|Z|sin\theta)(|Z|cos\theta - i|Z|sin\theta)} \quad \text{(D.5)}$$

Distributing,

$$= \frac{|Z|cos\theta - j|Z|sin\theta}{(|Z|^2 \cos^2\theta - j^2|Z|^2 \sin^2\theta)} \quad \text{(D.6)}$$

Noting $j^2 = -1$

$$= \frac{|Z|cos\theta - j|Z|sin\theta}{(|Z|^2 \cos^2\theta + |Z|^2 \sin^2\theta)} \quad \text{(D.7)}$$

Collecting $|Z|^2$ terms,

$$= \frac{|Z|(cos\theta - jsin\theta)}{|Z|^2(\cos^2\theta + \sin^2\theta)} \quad \text{(D.8)}$$

Simplifying,

$$= \frac{(cos\theta - jsin\theta)}{|Z|(\cos^2\theta + \sin^2\theta)} \quad \text{(D.9)}$$

Since $\sin^2\theta + \cos^2\theta = 1$, we now have

$$Y^* = \frac{1}{|Z|}(cos\theta - jsin\theta) \quad \text{(D.10)}$$

Distributing, we obtain:

$$Y^* = \frac{1}{|Z|}cos\theta - \frac{1}{|Z|}jsin\theta \quad \text{(D.11)}$$

From the definition of admittance

$$Y^* = G + jB \quad \text{(D.12)}$$

We can relate the conductance G to the first term

$$G = \frac{\sigma' A}{d} = \frac{1}{|Z|}cos\theta \quad \text{(D.13)}$$

and solve for the real component of conductivity

$$\sigma' = \frac{dcos\theta}{A|Z|} \quad \text{(D.14)}$$

Taking the inverse of conductivity yields the resistivity

$$\rho' = \frac{A|Z|}{d cos\theta} \tag{D.15}$$

where A is the sample area, $|Z|$ is magnitude of impedance, d is the sample thickness, and θ is the phase angle. The phase angle θ was calculated as the arctangent of the imaginary and real components of impedance,

$$\theta = \text{atan}\frac{Z''}{Z'} \tag{D.16}$$

The variation of the phase angle as a function of frequency is shown below in Figure D.3 for PEAA-TMA.

The DC resistivity was measured where the slope of the resistivity versus frequency plot goes to 0, i.e. where the resistivity becomes frequency independent.

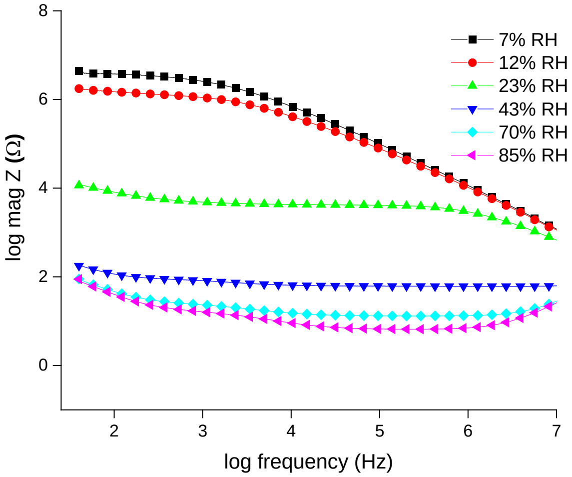

Figure D.2 Magnitude of impedance as a function of frequency for PEAA-TMA 7, 12, 23, 43, 70, and 85 % relative humidity.

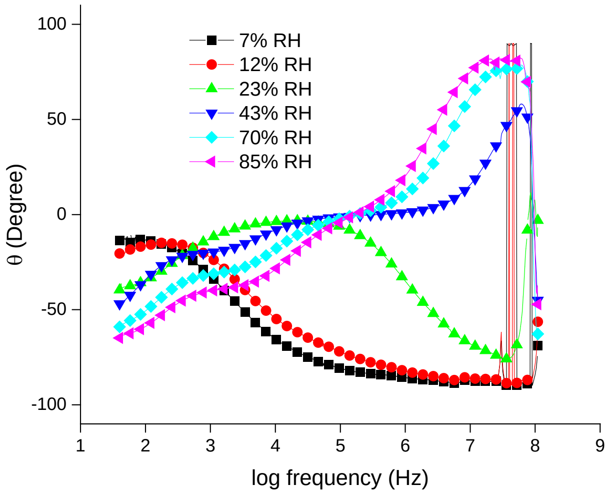

Figure D.3 Variation of phase angle for PEAA-TMA 7, 12, 23, 43, 70, and 85 % relative humidity.

D.3 ELASTIC BEAM THEORY

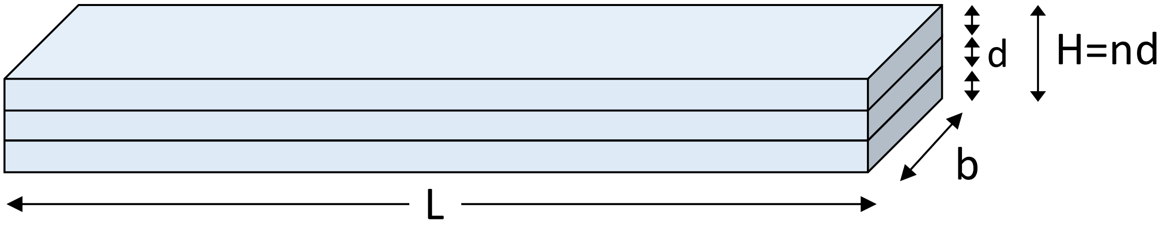

Figure D.4 Diagram of multilayered beam.

Consider a beam of span L, width b, and height H composed of n unbonded layers with thickness d. When a force is applied at the midpoint of the beam, the deflection D at the midpoint of the beam is given by the moment of inertia I, the applied force F, and the flexural modulus of the beam E_f,

$$D = \frac{L^3 F}{48 I E_\mathrm{f}} \tag{D.17}$$

where I for a solid rectangular cross-section composed of n unbonded layers is

$$I = \frac{1}{12} n b d^3 \tag{D.18}$$

The unbonded flexural modulus is then given by:

$$E_\mathrm{off} = \frac{L^3 m_\mathrm{off}}{4 n b d^3} \tag{D.19}$$

where $m_\mathrm{off} = F/D$ is the slope of the initial straight-line portion of the load versus deflection curve. If the layers of the structure are considered **fully bonded**, the moment of inertia becomes

$$I = \frac{1}{12} b (nd)^3 \tag{D.20}$$

where $nd = H$ is the total thickness of the beam. The flexural modulus now depends on the number of layers by a factor of n^3 as:

$$E_\mathrm{on} = \frac{L^3 m_\mathrm{on}}{4 n^3 b d^3} \tag{D.21}$$

The ratio of flexural modulus between on and off states, $E_{\mathrm{on}}/E_{\mathrm{off}}$, should then depend on the number of layers and the slope of the F/D curves as,

$$\frac{E_{\mathrm{on}}}{E_{\mathrm{off}}} = \frac{1}{n^2}\frac{m_{\mathrm{on}}}{m_{\mathrm{off}}} \tag{D.22}$$

assuming a perfectly bonded state for E_{on}.

An equivalent expression for the flexural modulus as discussed in the Main Text is

$$E_{\mathrm{on}} = \frac{L^3 m}{4bd_t^3} \tag{D.23}$$

where d_t is the total thickness of the structure ($d_t = nd$ for layers of uniform thickness). To aid in the comparison between on/off states, all calculations were made using the total thickness of the structure, i.e. assuming a fully bonded state in all cases, even at 0 V.

D.4 OPTICAL PROFILOMETRY DATA

(Contributed by Emily Barker)

Table D.1 Roughness parameters for PEAA-TMA, PEAA-TEA, and PEAA-TPA conditioned at 12% relative humidity.

Polymer	**Correction**	**Zoom**	**R_a (μm)**[a]	**R_q (μm)**[b]	**R_p (μm)**[c]	**R_v (μm)**[d]	**R_t (μm)**[e]
PEAA-TMA	Tilt	5x	0.875	1.29	1.52	-3.64	5.17
	Gaussian	5x	0.009	0.014	1.04	-1.18	2.22
	Tilt	10x	0.108	0.163	0.298	-0.653	0.951
	Gaussian	10x	0.015	0.019	0.271	-0.188	0.459
	Tilt	50x	0.014	0.018	0.071	-0.124	0.196
PEAA-TEA	Tilt	5x	0.764	0.976	1.00	-2.08	3.08
	Gaussian	5x	0.009	0.014	0.912	-0.798	1.71
	Tilt	10x	0.075	0.119	1.61	-0.175	1.78
	Gaussian	10x	0.014	0.021	0.780	-0.265	1.05
	Tilt	50x	0.013	0.016	0.564	-0.121	0.685
PEAA-TPA	Tilt	5x	0.361	0.471	2.30	-1.23	3.53
	Gaussian	5x	0.012	0.017	0.920	-0.662	1.58
	Gaussian	10x	0.019	0.025	0.820	-0.491	1.31
	Tilt	50x	0.029	0.037	0.169	-0.261	0.430

[a] Average roughness

[b] Root-mean-square (rms) roughness

[c] Maximum peak height

[d] Maximum valley depth

[e] Maximum height of profile ($R_t = R_p + R_v$)

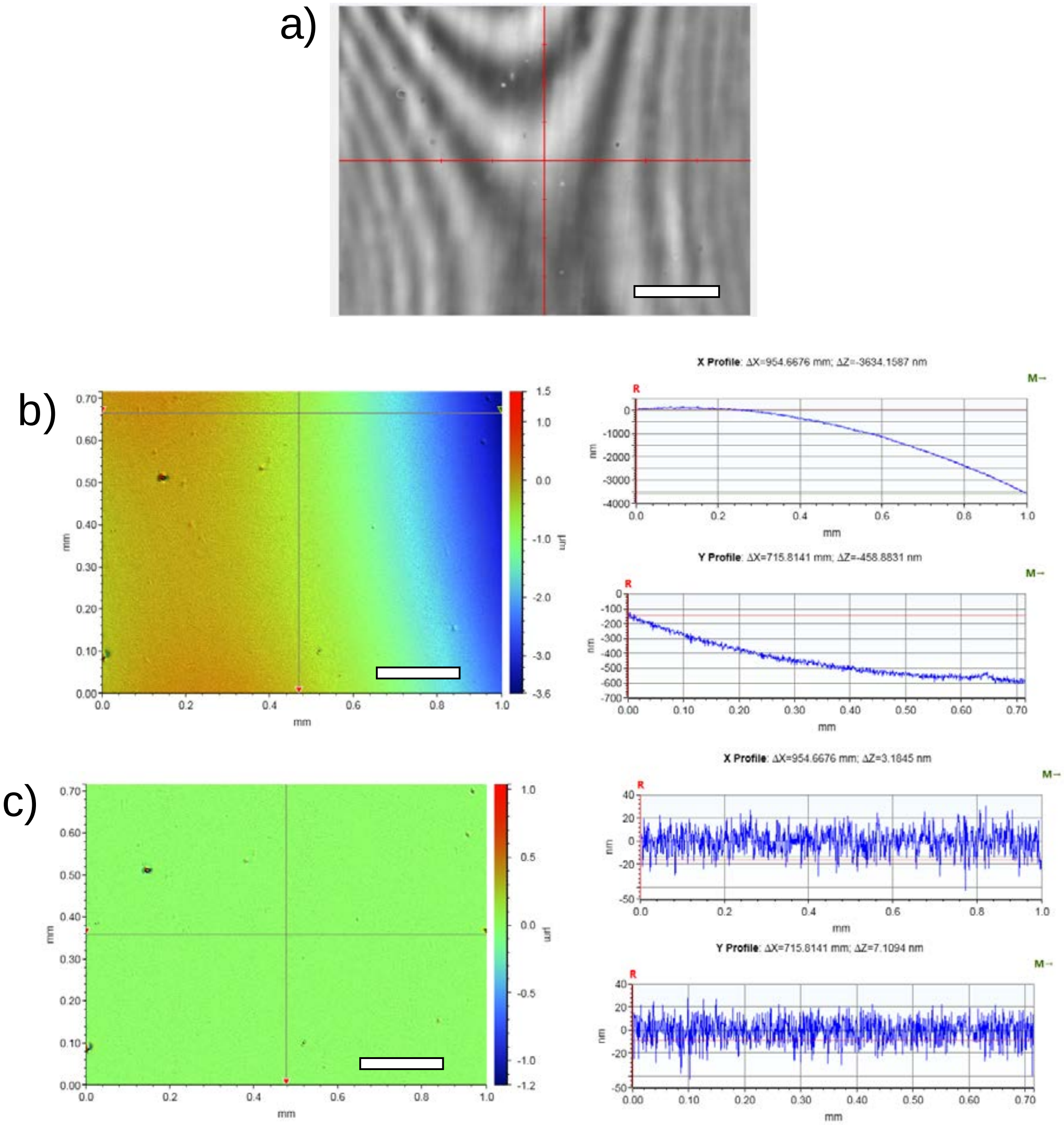

Figure D.5 PEAA-TMA at 5x magnification. a) optical image; b) with tilt correction applied and x-, y- profiles; c) with Gaussian correction applied and x-, y- profiles. Scale bars = 200 µm.

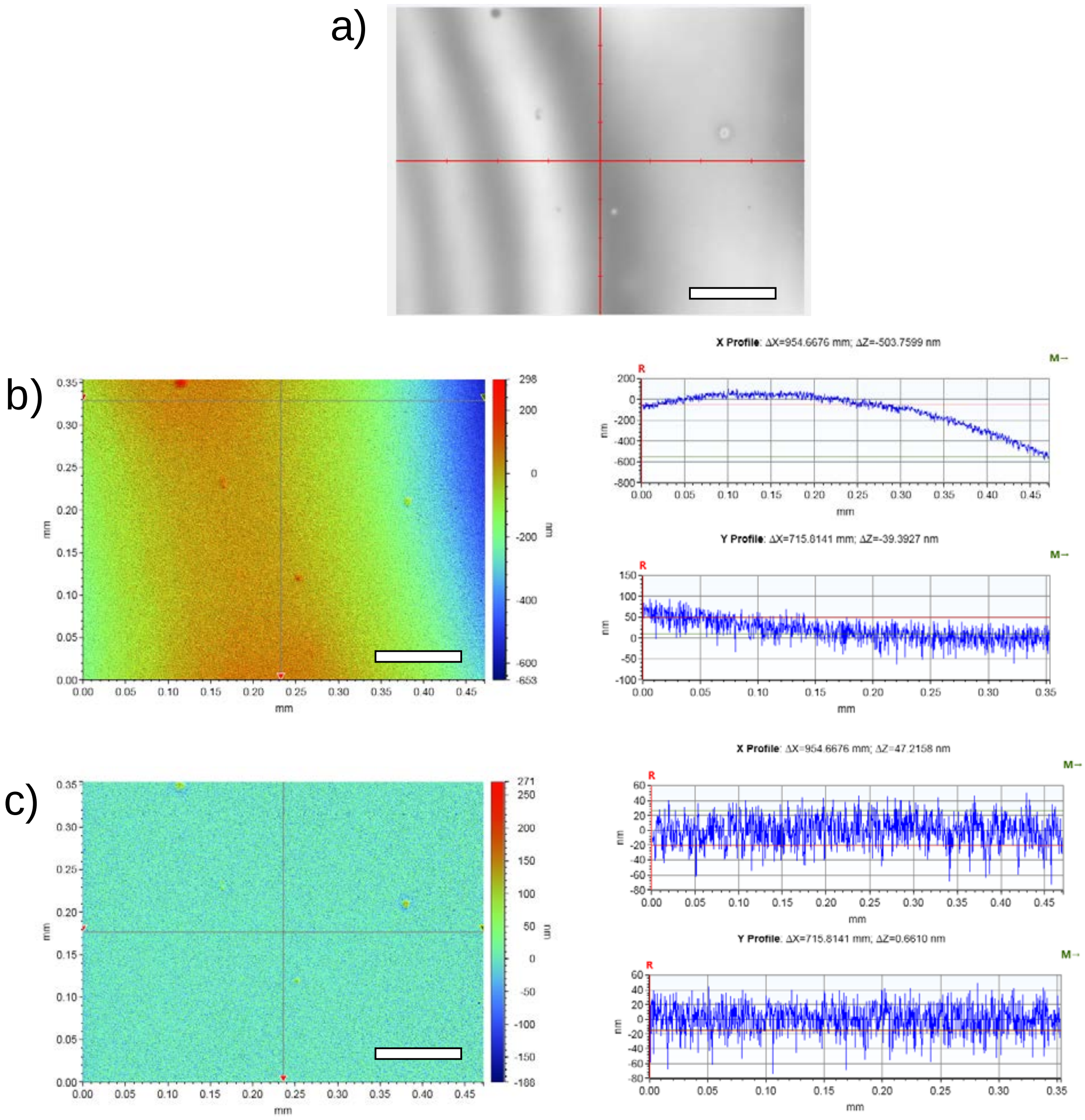

Figure D.6 PEAA-TMA at 10x magnification. a) optical image; b) with tilt correction applied and x-, y- profiles; c) with Gaussian correction applied and x-, y- profiles. Scale bars = 100 µm.

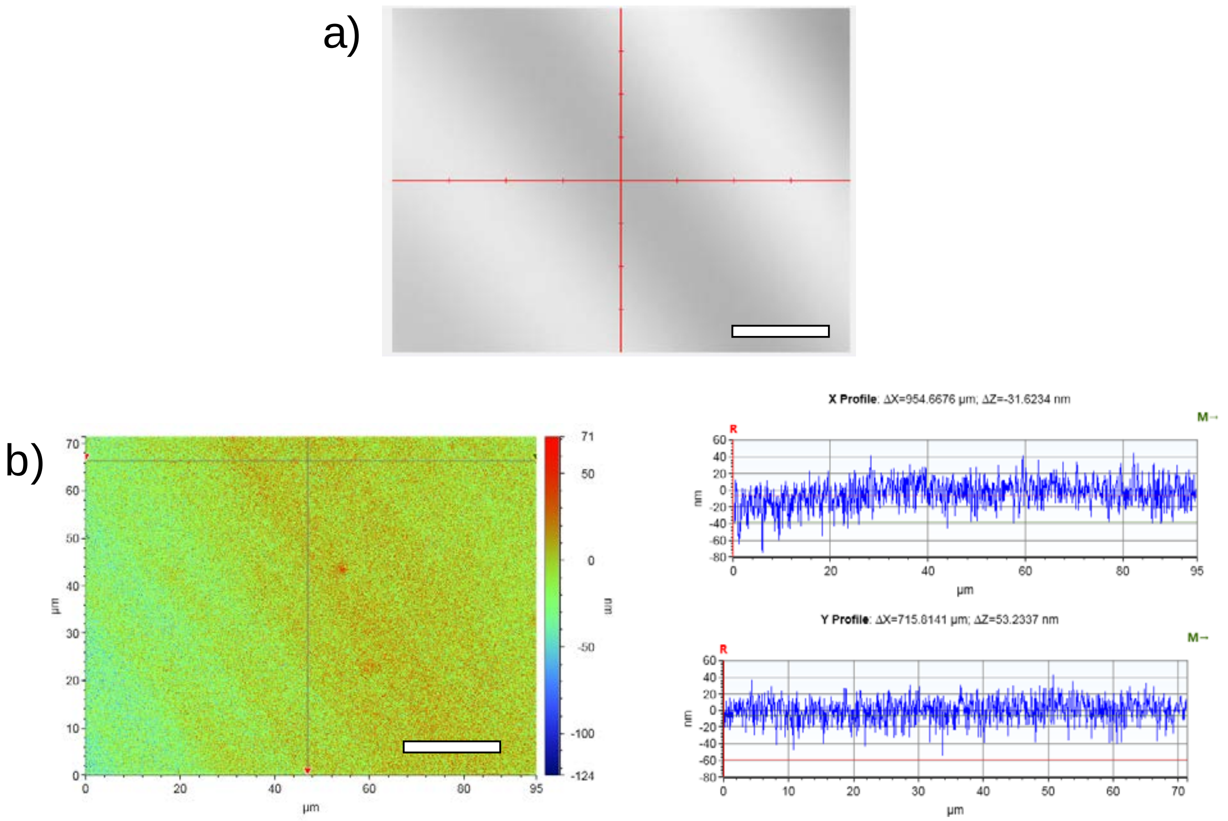

Figure D.7 PEAA-TMA at 50x magnification. a) optical image; b) with tilt correction applied and x-, y- profiles. Scale bars = 20 µm.

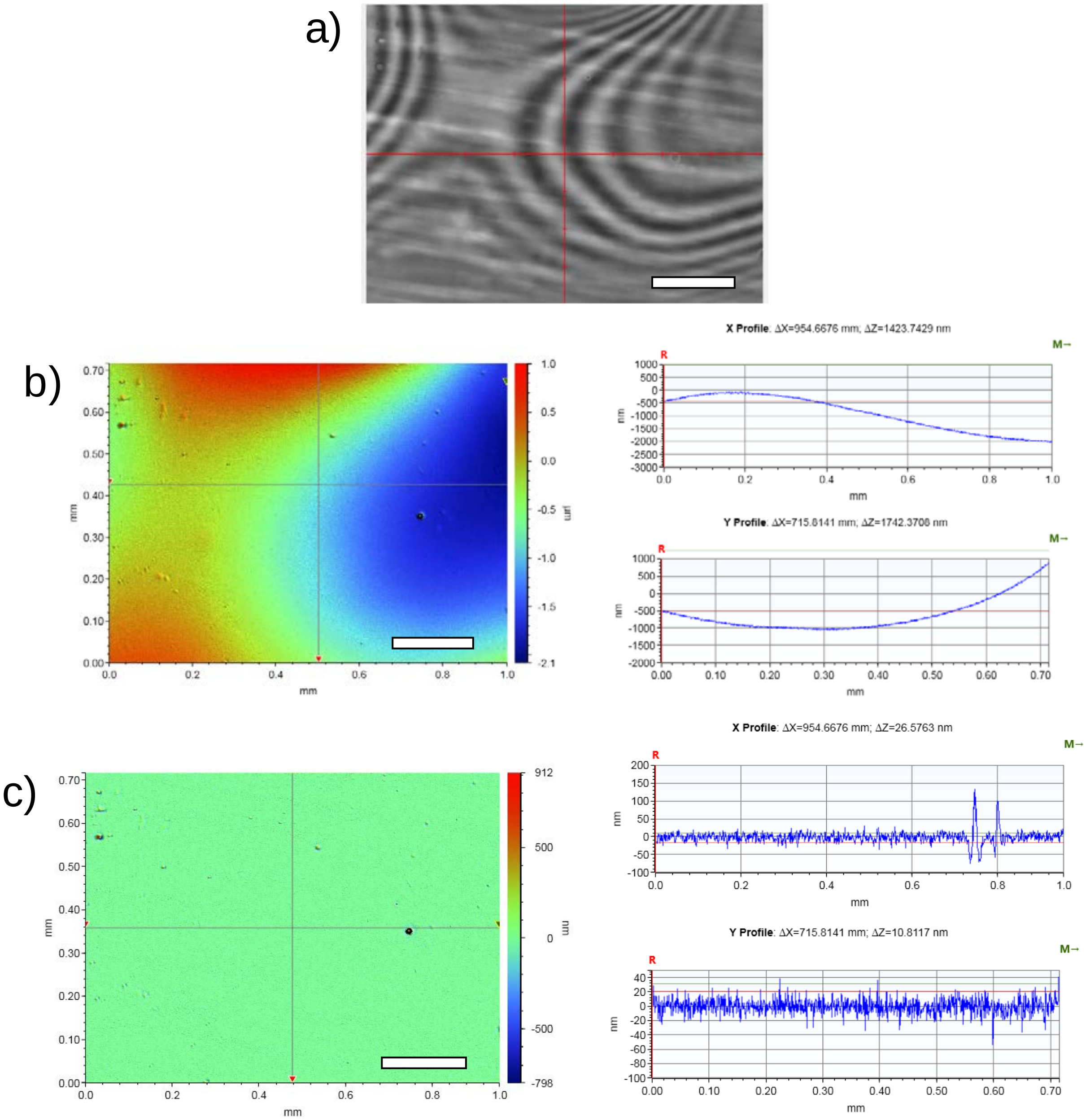

Figure D.8 PEAA-TEA at 5x magnification. a) optical image; b) with tilt correction applied and x-, y- profiles; c) with Gaussian correction applied and x-, y- profiles. Scale bars = 200 µm.

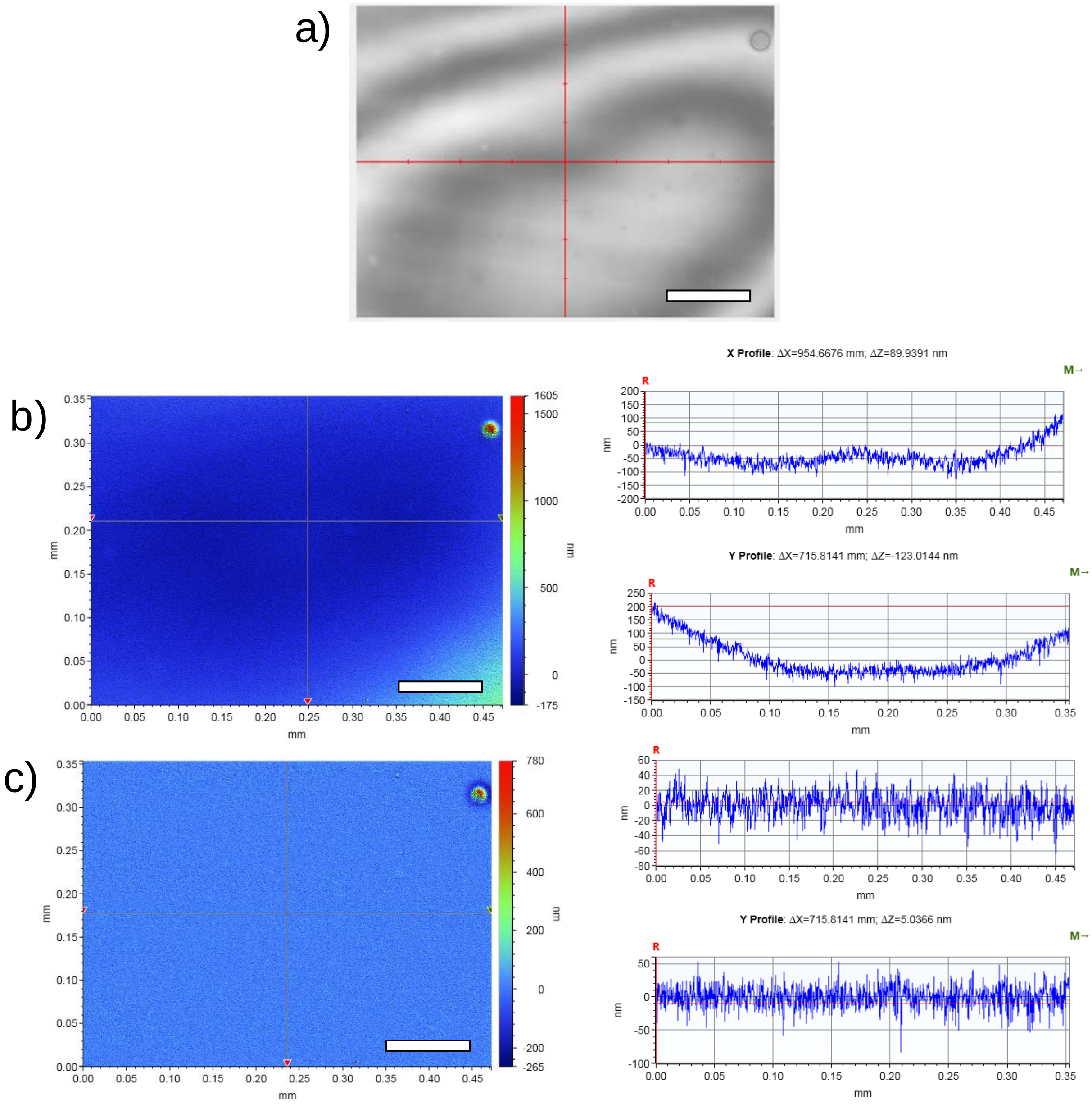

Figure D.9 PEAA-TEA at 10x magnification. a) optical image; b) with tilt correction applied and x-, y- profiles; c) with Gaussian correction applied and x-, y- profiles. Scale bars = 100 μm.

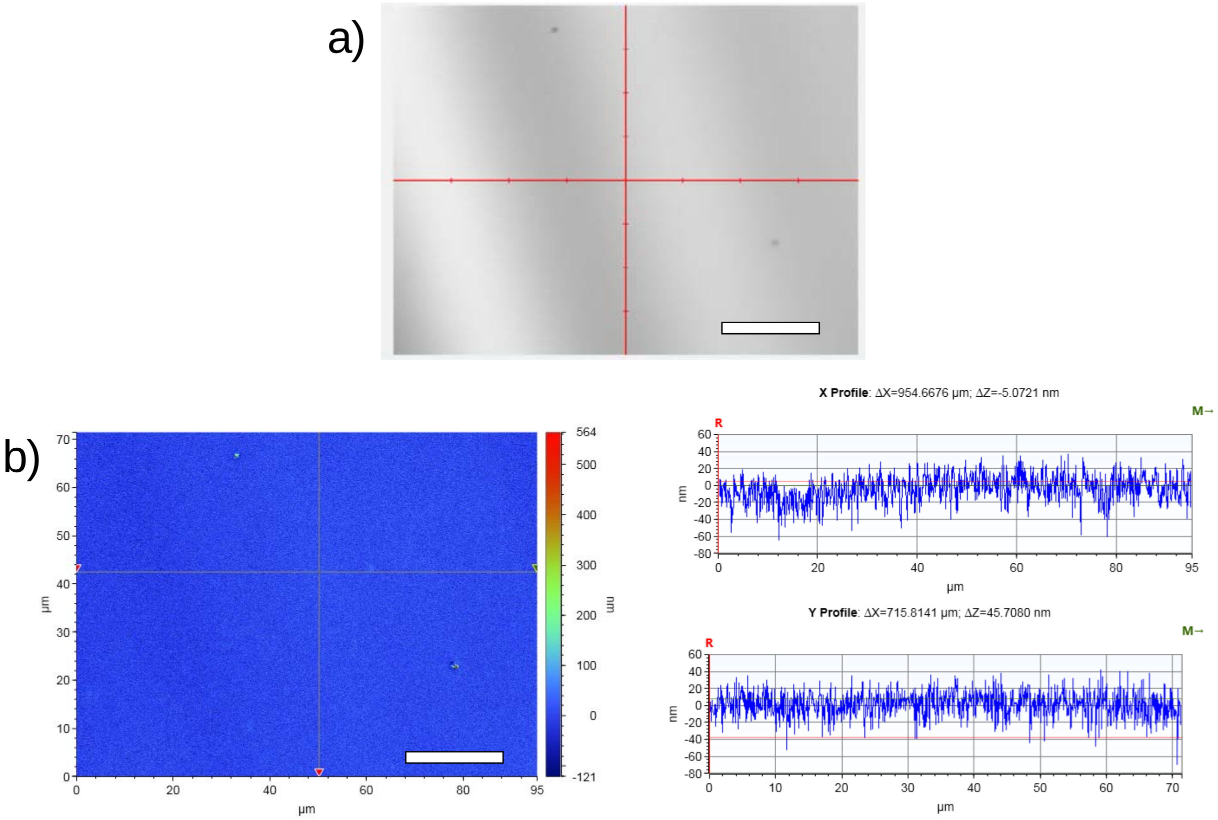

Figure D.10 PEAA-TEA at 50x magnification. a) optical image; b) with tilt correction applied and x-, y- profiles; Scale bars = 20 µm.

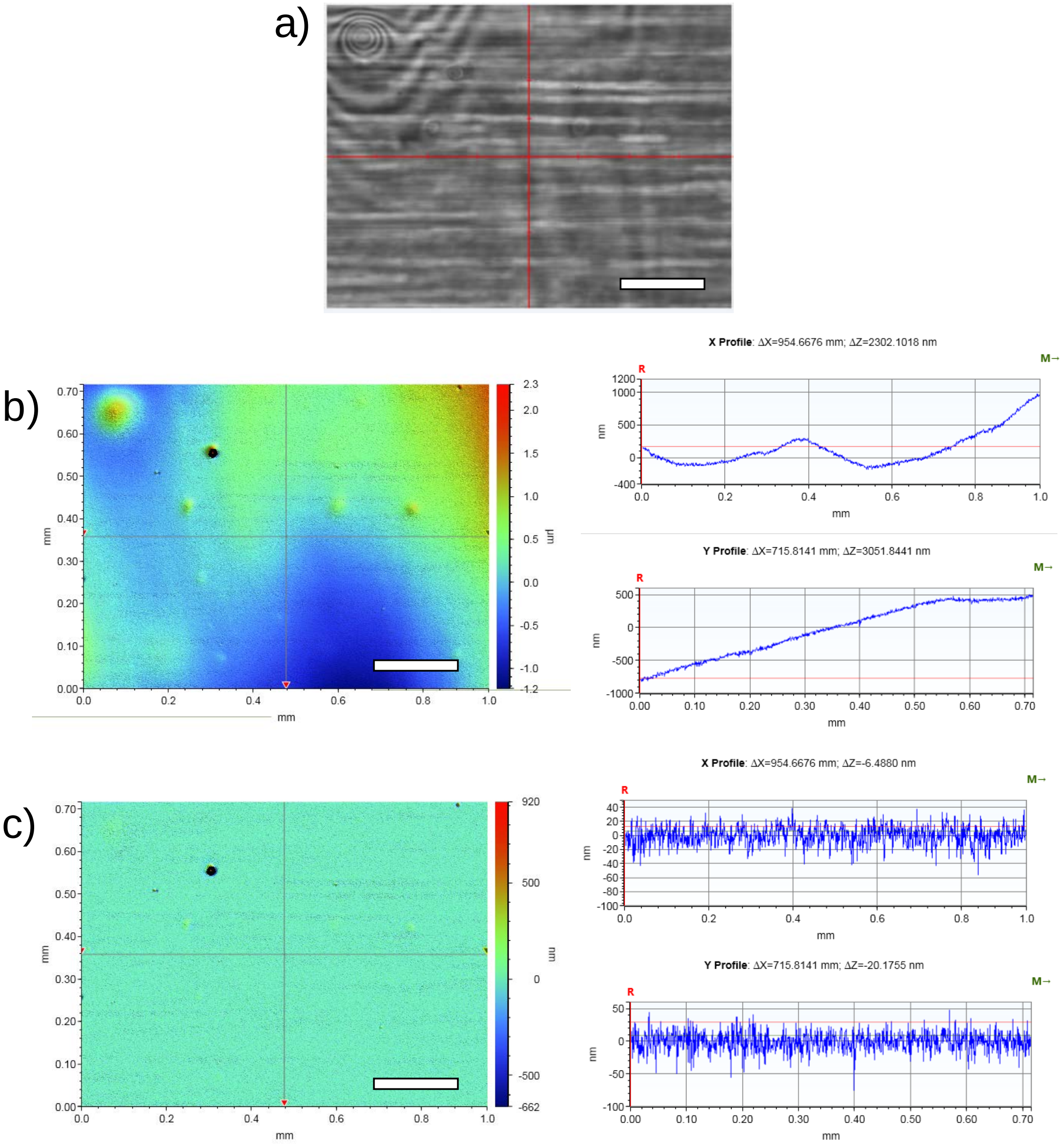

Figure D.11 PEAA-TPA at 5x magnification. a) optical image; b) with tilt correction applied and x-, y- profiles; c) with Gaussian correction applied and x-, y- profiles. Scale bars = 200 µm.

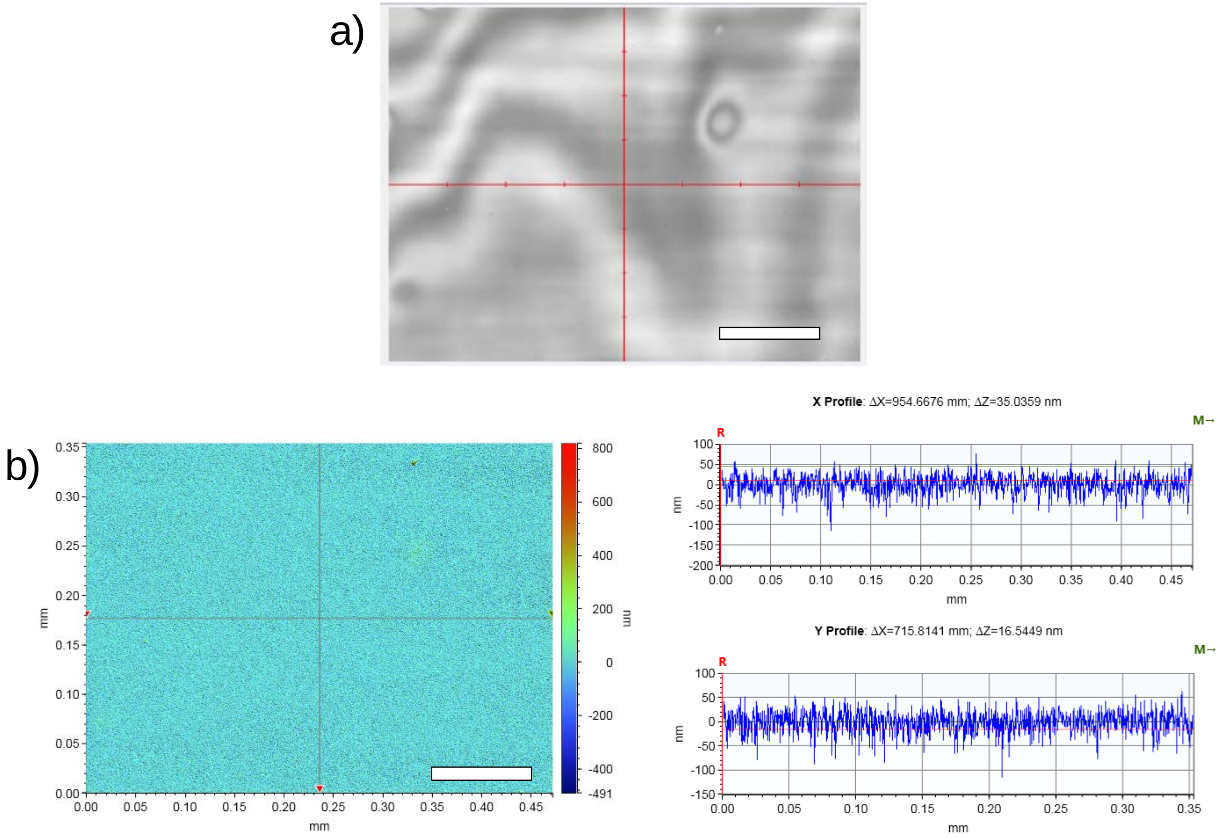

Figure D.12 PEAA-TPA at 10x magnification. a) optical image; b) with tilt correction applied and x-, y- profiles. Scale bars = 100 µm.

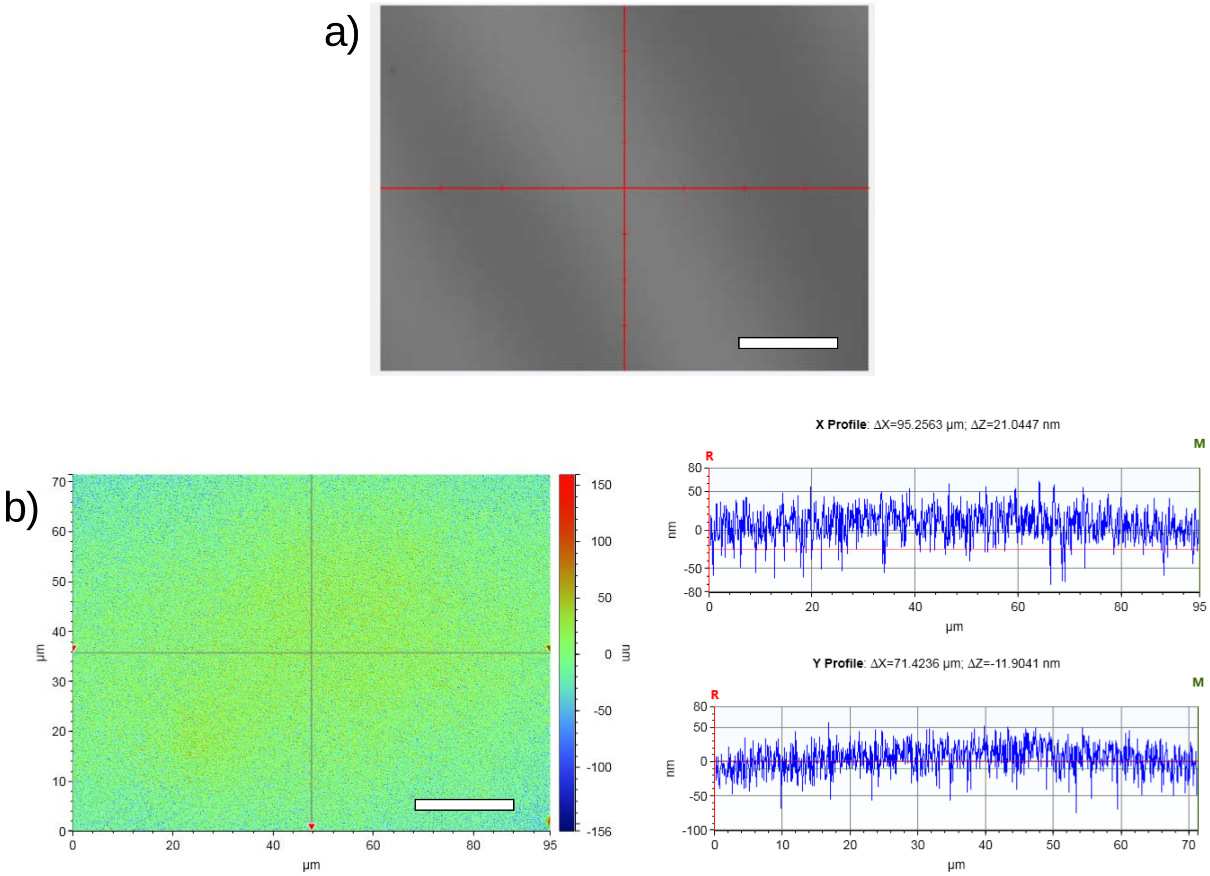

Figure D.13 PEAA-TPA at 50x magnification. a) optical image; b) with tilt correction applied and x-, y- profiles. Scale bars = 20 µm.

BIBLIOGRAPHY

1. Gaharwar, A. K.; Peppas, N. A.; Khademhosseini, A., Nanocomposite hydrogels for biomedical applications. *Biotechnol. Bioeng.* **2014,** *111* (3), 441-453.
2. Huo, M.; Yuan, J.; Tao, L.; Wei, Y., Redox-responsive polymers for drug delivery: from molecular design to applications. *Polym. Chem.* **2014,** *5* (5), 1519-1528.
3. Censi, R.; Di Martino, P.; Vermonden, T.; Hennink, W. E., Hydrogels for protein delivery in tissue engineering. *Journal of Controlled Release* **2012,** *161* (2), 680-692.
4. Buenger, D.; Topuz, F.; Groll, J., Hydrogels in sensing applications. *Prog. Polym. Sci.* **2012,** *37* (12), 1678-1719.
5. Ionov, L., Biomimetic Hydrogel-Based Actuating Systems. *Adv. Funct. Mater.* **2013,** *23* (36), 4555-4570.
6. Stumpel, J. E.; Broer, D. J.; Schenning, A. P. H. J., Stimuli-responsive photonic polymer coatings. *Chem. Commun. (Cambridge, U. K.)* **2014,** *50* (100), 15839-15848.
7. Geever, L. M.; Higginbotham, C. L.; Lyons, J. G.; Kennedy, J. E. In *History and continued development of drug delivery systems based on smart negative temperature sensitive hydrogels*, Nova Science Publishers, Inc.: 2009; pp 103-140.
8. Shiga, T., Deformation and Viscoelastic Behavior of Polymer Gels in Electric Fields. In *Neutron Spin Echo Spectroscopy Viscoelasticity Rheology*, Springer Berlin Heidelberg: 1997; Vol. 134, pp 131-163.
9. Filipcsei, G.; Csetneki, I.; Szilágyi, A.; Zrínyi, M., Magnetic Field-Responsive Smart Polymer Composites. In *Oligomers - Polymer Composites - Molecular Imprinting*, Springer Berlin Heidelberg: 2007; Vol. 206, pp 137-189.
10. Eliyahu-Gross, S.; Bitton, R., Environmentally responsive hydrogels with dynamically tunable properties as extracellular matrix mimetic. *Rev. Chem. Eng.* **2013,** *29* (3), 159-168.
11. Sui, X.; Feng, X.; Hempenius, M. A.; Vancso, G. J., Redox active gels: synthesis, structures and applications. *Journal of Materials Chemistry B* **2013,** *1* (12), 1658-1672.
12. Haq, M. A.; Su, Y.; Wang, D., Mechanical properties of PNIPAM based hydrogels: A review. *Materials Science and Engineering: C* **2017,** *70, Part 1*, 842-855.
13. Capadona, J. R.; Shanmuganathan, K.; Tyler, D. J.; Rowan, S. J.; Weder, C., Stimuli-Responsive Polymer Nanocomposites Inspired by the Sea Cucumber Dermis. *Science (Washington, DC, U. S.)* **2008,** *319* (5868), 1370-1374.
14. Beblo, R. V.; Weiland, L. M., Light Activated Shape Memory Polymer Characterization. *Journal of Applied Mechanics* **2008,** *76* (1), 011008-011008-8.
15. Beblo, R. V.; Weiland, L. M., Light Activated Shape Memory Polymer Characterization—Part II. *Journal of Applied Mechanics* **2011,** *78* (6), 061016-061016-9.
16. Heinzmann, C.; Coulibaly, S.; Roulin, A.; Fiore, G. L.; Weder, C., Light-Induced Bonding and Debonding with Supramolecular Adhesives. *ACS Applied Materials & Interfaces* **2014,** *6* (7), 4713-4719.
17. Carey, B. J.; Patra, P. K.; Ci, L.; Silva, G. G.; Ajayan, P. M., Observation of Dynamic Strain Hardening in Polymer Nanocomposites. *ACS Nano* **2011,** *5* (4), 2715-2722.

18. Agrawal, A.; Chipara, A. C.; Shamoo, Y.; Patra, P. K.; Carey, B. J.; Ajayan, P. M.; Chapman, W. G.; Verduzco, R., Dynamic self-stiffening in liquid crystal elastomers. *Nature Communications* **2013,** *4*, 1739.
19. Wang, J.; Piskun, I.; Craig, S. L., Mechanochemical Strengthening of a Multi-mechanophore Benzocyclobutene Polymer. *ACS Macro Letters* **2015,** *4* (8), 834-837.
20. Gossweiler, G. R.; Hewage, G. B.; Soriano, G.; Wang, Q.; Welshofer, G. W.; Zhao, X.; Craig, S. L., Mechanochemical Activation of Covalent Bonds in Polymers with Full and Repeatable Macroscopic Shape Recovery. *ACS Macro Letters* **2014,** *3* (3), 216-219.
21. Annovazzi, L.; Genna, F., An engineering, multiscale constitutive model for fiber-forming collagen in tension. *Journal of Biomedical Materials Research Part A* **2010,** *92A* (1), 254-266.
22. Motte, S.; Kaufman, L. J., Strain stiffening in collagen I networks. *Biopolymers* **2013,** *99* (1), 35-46.
23. Wanliang, S.; Tong, L.; Carmel, M., Soft-matter composites with electrically tunable elastic rigidity. *Smart Materials and Structures* **2013,** *22* (8), 085005.
24. Wanliang, S.; Stuart, D.; Abbas, T.; Carmel, M., Rigidity-tuning conductive elastomer. *Smart Materials and Structures* **2015,** *24* (6), 065001.
25. Aida, T.; Meijer, E. W.; Stupp, S. I., Functional Supramolecular Polymers. *Science (Washington, DC, United States)* **2012,** *335* (6070), 813-817.
26. Appel, E. A.; Biedermann, F.; Rauwald, U.; Jones, S. T.; Zayed, J. M.; Scherman, O. A., Supramolecular Cross-Linked Networks via Host-Guest Complexation with Cucurbit[8]uril. *J. Am. Chem. Soc.* **2010,** *132* (40), 14251-14260.
27. de Greef, T. F. A.; Meijer, E. W., Materials science: Supramolecular polymers. *Nature* **2008,** *453* (7192), 171-173.
28. Tsitsilianis, C., Responsive reversible hydrogels from associative "smart" macromolecules. *Soft Matter* **2010,** *6* (11), 2372-2388.
29. Jaber, J. A.; Schlenoff, J. B., Mechanical Properties of Reversibly Cross-Linked Ultrathin Polyelectrolyte Complexes. *Journal of the American Chemical Society* **2006,** *128* (9), 2940-2947.
30. Reisch, A.; Moussallem, M. D.; Schlenoff, J. B., Electrochemically Addressed Cross-Links in Polyelectrolyte Multilayers: Cyclic Duravoltammetry. *Langmuir* **2011,** *27* (15), 9418-9424.
31. De Greef, T. F. A.; Smulders, M. M. J.; Wolffs, M.; Schenning, A. P. H. J.; Sijbesma, R. P.; Meijer, E. W., Supramolecular Polymerization. *Chem. Rev. (Washington, DC, U. S.)* **2009,** *109* (11), 5687-5754.
32. Li, W.; Kim, Y.; Li, J.; Lee, M., Dynamic self-assembly of coordination polymers in aqueous solution. *Soft Matter* **2014,** *10* (29), 5231-5242.
33. Gracia, R.; Mecerreyes, D., Polymers with redox properties: materials for batteries, biosensors and more. *Polymer Chemistry* **2013,** *4* (7), 2206-2214.
34. Harada, A.; Takashima, Y.; Nakahata, M., Supramolecular Polymeric Materials via Cyclodextrin-Guest Interactions. *Acc. Chem. Res.* **2014,** *47* (7), 2128-2140.
35. Hempenius, M. A.; Cirmi, C.; Lo Savio, F.; Song, J.; Vancso, G. J., Poly(ferrocenylsilane) Gels and Hydrogels with Redox-Controlled Actuation. *Macromol. Rapid Commun.* **2010,** *31* (9-10), 772-783.
36. Yan, X.; Wang, F.; Zheng, B.; Huang, F., Stimuli-responsive supramolecular polymeric materials. *Chemical Society Reviews* **2012,** *41* (18), 6042-6065.

37. Peng, F.; Li, G.; Liu, X.; Wu, S.; Tong, Z., Redox-responsive gel-sol/sol-gel transition in poly(acrylic acid) aqueous solution containing Fe(III) ions switched by light. *J. Am. Chem. Soc.* **2008,** *130* (48), 16166-16167.
38. He, S.; Ren, B.; Liu, X.; Tong, Z., Reversible Electrogelation in Poly(acrylic acid) Aqueous Solutions Triggered by Redox Reactions of Counterions. *Macromolecular Chemistry and Physics* **2010,** *211* (23), 2497-2502.
39. Wei, Z.; He, J.; Liang, T.; Oh, H.; Athas, J.; Tong, Z.; Wang, C.; Nie, Z., Autonomous self-healing of poly(acrylic acid) hydrogels induced by the migration of ferric ions. *Polymer Chemistry* **2013,** *4* (17), 4601-4605.
40. Narayanan, R. P.; Melman, G.; Letourneau, N. J.; Mendelson, N. L.; Melman, A., Photodegradable Iron(III) Cross-Linked Alginate Gels. *Biomacromolecules* **2012,** *13* (8), 2465-2471.
41. Giammanco, G. E.; Carrion, B.; Coleman, R. M.; Ostrowski, A. D., Photoresponsive Polysaccharide-Based Hydrogels with Tunable Mechanical Properties for Cartilage Tissue Engineering. *ACS Applied Materials & Interfaces* **2016,** *8* (23), 14423-14429.
42. Gasnier, A.; Royal, G.; Terech, P., Metallo-Supramolecular Gels Based on a Multitopic Cyclam Bis-Terpyridine Platform. *Langmuir* **2009,** *25* (15), 8751-8762.
43. Miller, A. K.; Li, Z.; Streletzky, K. A.; Jamieson, A. M.; Rowan, S. J., Redox-induced polymerisation/depolymerisation of metallo-supramolecular polymers. *Polymer Chemistry* **2012,** *3* (11), 3132-3138.
44. Kawano, S.; Fujita, N.; Shinkai, S., A Coordination Gelator That Shows a Reversible Chromatic Change and Sol-Gel Phase-Transition Behavior upon Oxidative/Reductive Stimuli. *J. Am. Chem. Soc.* **2004,** *126* (28), 8592-8593.
45. Palleau, E.; Morales, D.; Dickey, M. D.; Velev, O. D., Reversible patterning and actuation of hydrogels by electrically assisted ionoprinting. *Nat Commun* **2013,** *4*.
46. Varghese, S.; Lele, A.; Mashelkar, R., Metal-ion-mediated healing of gels. *Journal of Polymer Science Part A: Polymer Chemistry* **2006,** *44* (1), 666-670.
47. Nakahata, M.; Takashima, Y.; Harada, A., Redox-Responsive Macroscopic Gel Assembly Based on Discrete Dual Interactions. *Angewandte Chemie International Edition* **2014,** *53* (14), 3617-3621.
48. Nakahata, M.; Takashima, Y.; Yamaguchi, H.; Harada, A., Redox-responsive self-healing materials formed from host–guest polymers. *Nature Communications* **2011,** *2*, 511.
49. Nakahata, M.; Takashima, Y.; Hashidzume, A.; Harada, A., Redox-Generated Mechanical Motion of a Supramolecular Polymeric Actuator Based on Host–Guest Interactions. *Angewandte Chemie International Edition* **2013,** *52* (22), 5731-5735.
50. Puzzo, D. P.; Arsenault, A. C.; Manners, I.; Ozin, G. A., Electroactive Inverse Opal: A Single Material for All Colors. *Angewandte Chemie International Edition* **2009,** *48* (5), 943-947.
51. Arsenault, A. C.; Puzzo, D. P.; Manners, I.; Ozin, G. A., Photonic-crystal full-colour displays. *Nat Photon* **2007,** *1* (8), 468-472.
52. Grieshaber, D.; Voros, J.; Zambelli, T.; Ball, V.; Schaaf, P.; Voegel, J.-C.; Boulmedais, F., Swelling and Contraction of Ferrocyanide-Containing Polyelectrolyte Multilayers upon Application of an Electric Potential. *Langmuir* **2008,** *24* (23), 13668-13676.
53. Gyarmati, B.; Nemethy, A.; Szilagyi, A., Reversible response of poly(aspartic acid) hydrogels to external redox and pH stimuli. *RSC Advances* **2014,** *4* (17), 8764-8771.

54. Zhang, P.; Deng, F.; Peng, Y.; Chen, H.; Gao, Y.; Li, H., Redox- and pH-responsive polymer gels with reversible sol-gel transitions and self-healing properties. *RSC Advances* **2014,** *4* (88), 47361-47367.
55. Chujo, Y.; Sada, K.; Naka, A.; Nomura, R.; Saegusa, T., Synthesis and redox gelation of disulfide-modified polyoxazoline. *Macromolecules* **1993,** *26* (5), 883-7.
56. Gyarmati, B.; Nemethy, A.; Szilagyi, A., Reversible response of poly(aspartic acid) hydrogels to external redox and pH stimuli. *RSC Adv.* **2014,** *4* (17), 8764-8771.
57. Li, Y.; Park, T.; Quansah, J. K.; Zimmerman, S. C., Synthesis of a Redox-Responsive Quadruple Hydrogen-Bonding Unit for Applications in Supramolecular Chemistry. *Journal of the American Chemical Society* **2011,** *133* (43), 17118-17121.
58. Calvo-Marzal, P.; Delaney, M. P.; Auletta, J. T.; Pan, T.; Perri, N. M.; Weiland, L. M.; Waldeck, D. H.; Clark, W. W.; Meyer, T. Y., Manipulating Mechanical Properties with Electricity: Electroplastic Elastomer Hydrogels. *ACS Macro Letters* **2011**, 204-208.
59. Ahn, S. K.; Kasi, R. M.; Kim, S. C.; Sharma, N.; Zhou, Y. X., Stimuli-responsive polymer gels. *Soft Matter* **2008,** *4* (6), 1151-1157.
60. Sui, X.; Feng, X.; Hempenius, M. A.; Vancso, G. J., Redox active gels: synthesis, structures and applications. *J. Mater. Chem. B* **2013,** *1* (12), 1658-1672.
61. Brannon-Peppas, L.; Harland, R. S., *Absorbent Polymer Technology*. Elsevier: 1990.
62. Ratner, B. D.; Hoffman, A. S.; Schoen, F. J.; Lemons, J. E., *Biomaterials Science - An Introduction to Materials in Medicine (2nd Edition)*. Elsevier: 2004.
63. Naficy, S.; Brown, H. R.; Razal, J. M.; Spinks, G. M.; Whitten, P. G., Progress Toward Robust Polymer Hydrogels. *Australian Journal of Chemistry* **2011,** *64* (8), 1007-1025.
64. Gong, J. P., Why are double network hydrogels so tough? *Soft Matter* **2010,** *6* (12), 2583-2590.
65. Anseth, K. S.; Bowman, C. N.; Brannon-Peppas, L., Mechanical properties of hydrogels and their experimental determination. *Biomaterials* **1996,** *17* (17), 1647-1657.
66. Mathiowitz, E., *Encyclopedia of Controlled Drug Delivery, Volumes 1-2*. John Wiley & Sons: 1999.
67. Hiemenz, P. C., *Polymer Chemistry - The Basic Concepts*. Marcel Dekker: New York, 1984.
68. Temenoff, J. S.; Athanasiou, K. A.; Lebaron, R. G.; Mikos, A. G., Effect of poly(ethylene glycol) molecular weight on tensile and swelling properties of oligo(poly(ethylene glycol) fumarate) hydrogels for cartilage tissue engineering. *J. Biomed. Mater. Res., Part A* **2002,** *59* (3), 429-437.
69. Haraguchi, K.; Takehisa, T., Nanocomposite Hydrogels: A Unique Organic–Inorganic Network Structure with Extraordinary Mechanical, Optical, and Swelling/De-swelling Properties. *Advanced Materials* **2002,** *14* (16), 1120-1124.
70. Shibayama, M., Structure-mechanical property relationship of tough hydrogels. *Soft Matter* **2012,** *8* (31), 8030-8038.
71. Haraguchi, K.; Farnworth, R.; Ohbayashi, A.; Takehisa, T., Compositional Effects on Mechanical Properties of Nanocomposite Hydrogels Composed of Poly(N,N-dimethylacrylamide) and Clay. *Macromolecules* **2003,** *36* (15), 5732-5741.
72. Allen, M. J.; Tung, V. C.; Kaner, R. B., Honeycomb Carbon: A Review of Graphene. *Chemical Reviews* **2010,** *110* (1), 132-145.
73. Du, J.; Cheng, H.-M., The Fabrication, Properties, and Uses of Graphene/Polymer Composites. *Macromolecular Chemistry and Physics* **2012**, 1060-1077.
74. Huang, X.; Qi, X.; Boey, F.; Zhang, H., Graphene-based composites. *Chemical Society Reviews* **2012,** *41* (2), 666-686.

75. Xu, Y.; Shi, G., Assembly of chemically modified graphene: methods and applications. *Journal of Materials Chemistry* **2011,** *21* (Copyright (C) 2012 American Chemical Society (ACS). All Rights Reserved.), 3311-3323.
76. Potts, J. R.; Dreyer, D. R.; Bielawski, C. W.; Ruoff, R. S., Graphene-based polymer nanocomposites. *Polymer* **2011,** *52* (Copyright (C) 2012 American Chemical Society (ACS). All Rights Reserved.), 5-25.
77. Bai, H.; Li, C.; Shi, G., Functional composite materials based on chemically converted graphene. *Advanced Materials* **2011,** *23,* 1089-1115.
78. Kuilla, T.; Bhadra, S.; Yao, D. H.; Kim, N. H.; Bose, S.; Lee, J. H., Recent advances in graphene based polymer composites. *Prog. Polym. Sci.* **2010,** *35* (11), 1350-1375.
79. Hummers, W. S.; Offeman, R. E., Preparation of Graphitic Oxide. *Journal of the American Chemical Society* **1958,** *80* (6), 1339-1339.
80. Bonanni, A.; Ambrosi, A.; Pumera, M., On Oxygen-Containing Groups in Chemically Modified Graphenes. *Chemistry – A European Journal* **2012,** *18* (15), 4541-4548.
81. Huang, Y.; Zeng, M.; Ren, J.; Wang, J.; Fan, L.; Xu, Q., Preparation and swelling properties of graphene oxide/poly(acrylic acid-co-acrylamide) super-absorbent hydrogel nanocomposites. *Colloids Surf., A* **2012,** *401* (Copyright (C) 2012 American Chemical Society (ACS). All Rights Reserved.), 97-106.
82. Shen, J.; Yan, B.; Li, T.; Long, Y.; Li, N.; Ye, M., Mechanical, thermal and swelling properties of poly(acrylic acid)-graphene oxide composite hydrogels. *Soft Matter* **2012,** *8* (6), 1831-1836.
83. Glover, A. J.; Cai, M.; Overdeep, K. R.; Kranbuehl, D. E.; Schniepp, H. C., In Situ Reduction of Graphene Oxide in Polymers. *Macromolecules* **2011,** *44* (24), 9821-9829.
84. Li, Z.; Shen, J.; Ma, H.; Lu, X.; Shi, M.; Li, N.; Ye, M., Preparation and characterization of pH- and temperature-responsive hydrogels with surface-functionalized graphene oxide as the crosslinker. *Soft Matter* **2012,** *8* (Copyright (C) 2012 American Chemical Society (ACS). All Rights Reserved.), 3139-3145.
85. Haraguchi, K.; Song, L., Microstructures Formed in Co-Cross-Linked Networks and Their Relationships to the Optical and Mechanical Properties of PNIPA/Clay Nanocomposite Gels. *Macromolecules* **2007,** *40* (15), 5526-5536.
86. Liu, R.; Liang, S.; Tang, X.-Z.; Yan, D.; Li, X.; Yu, Z.-Z., Tough and highly stretchable graphene oxide/polyacrylamide nanocomposite hydrogels. *J. Mater. Chem.* **2012,** *22* (Copyright (C) 2012 American Chemical Society (ACS). All Rights Reserved.), 14160-14167.
87. Liu, J.; Chen, C.; He, C.; Zhao, J.; Yang, X.; Wang, H., Synthesis of Graphene Peroxide and Its Application in Fabricating Super Extensible and Highly Resilient Nanocomposite Hydrogels. *ACS Nano* **2012**.
88. Dreyer, D. R.; Park, S.; Bielawski, C. W.; Ruoff, R. S., The chemistry of graphene oxide. *Chemical Society Reviews* **2010,** *39* (1), 228-240.
89. Bai, H.; Li, C.; Wang, X.-L.; Shi, G.-Q., On the Gelation of Graphene Oxide. *J. Phys. Chem. C* **2011,** *115*, 5545-5551.
90. Park, S.; Lee, K.-S.; Bozoklu, G.; Cai, W.; Nguyen, S. T.; Ruoff, R. S., Graphene Oxide Papers Modified by Divalent Ions—Enhancing Mechanical Properties via Chemical Cross-Linking. *Acs Nano* **2008,** *2* (3), 572-578.
91. Fromm, J.; Lautner, S., Electrical signals and their physiological significance in plants. *Plant, Cell Environ.* **2007,** *30* (Copyright (C) 2011 American Chemical Society (ACS). All Rights Reserved.), 249-257.

92. Hochachka, P. W., *Muscles as Molecular and Metabolic Machines*. CRC Press: Boca Raton, 1994.
93. Urban, M. W., Stratification, stimuli-responsiveness, self-healing, and signaling in polymer networks. *Prog. Polym. Sci.* **2009,** *34* (8), 679-687.
94. Wrigglesworth, J., *Energy and Life*. Taylor & Francis, Inc.: Bristol, 1997.
95. Liu, F.; Urban, M. W., Recent advances and challenges in designing stimuli-responsive polymers. *Prog. Polym. Sci.* **2010,** *35* (1-2), 3-23.
96. Wojtecki, R. J.; Meador, M. A.; Rowan, S. J., Using the dynamic bond to access macroscopically responsive structurally dynamic polymers. *Nat. Mater.* **2011,** *10* (1), 14-27.
97. Cohen Stuart, M. A.; Huck, W. T. S.; Genzer, J.; Mueller, M.; Ober, C.; Stamm, M.; Sukhorukov, G. B.; Szleifer, I.; Tsukruk, V. V.; Urban, M.; Winnik, F.; Zauscher, S.; Luzinov, I.; Minko, S., Emerging applications of stimuli-responsive polymer materials. *Nat. Mater.* **2010,** *9* (2), 101-113.
98. Ahn, S.-k.; Kasi, R. M.; Kim, S.-C.; Sharma, N.; Zhou, Y., Stimuli-responsive polymer gels. *Soft Matter* **2008,** *4* (6), 1151-1157.
99. Pasparakis, G.; Vamvakaki, M., Multiresponsive polymers: nano-sized assemblies, stimuli-sensitive gels and smart surfaces. *Polymer Chemistry* **2011,** *2* (6), 1234-1248.
100. Whittell, G. R.; Hager, M. D.; Schubert, U. S.; Manners, I., Functional soft materials from metallopolymers and metallosupramolecular polymers. *Nat. Mater.* **2011,** *10* (Copyright (C) 2011 American Chemical Society (ACS). All Rights Reserved.), 176-188.
101. Nair, K. P. N.; Breedveld, V.; Weck, M., Multiresponsive Reversible Polymer Networks Based on Hydrogen Bonding and Metal Coordination. *Macromolecules* **2011,** *44*, 3346-3357.
102. Capadona, J. R.; Shanmuganathan, K.; Tyler, D. J.; Rowan, S. J.; Weder, C., Stimuli-Responsive Polymer Nanocomposites Inspired by the Sea Cucumber Dermis. *Science* **2008,** *319* (5868), 1370-1374.
103. Oku, T.; Furusho, Y.; Takata, T., A concept for recyclable cross-linked polymers: Topologically networked polyrotaxane capable of undergoing reversible assembly and disassembly. *Angewandte Chemie-International Edition* **2004,** *43* (8), 966-969.
104. Higaki, Y.; Otsuka, H.; Takahara, A., A thermodynamic polymer cross-linking system based on radically exchangeable covalent bonds. *Macromolecules* **2006,** *39* (6), 2121-2125.
105. Inglis, A. J.; Nebhani, L.; Altintas, O.; Schmidt, F. G.; Barner-Kowollik, C., Rapid Bonding/Debonding on Demand: Reversibly Cross-Linked Functional Polymers via Diels-Alder Chemistry. *Macromolecules* **2010,** *43* (13), 5515-5520.
106. Shahinpoor, M.; Kim, K. J., Ionic polymer-metal composites: I. Fundamentals. *Smart Materials and Structures* **2001,** *10* (4), 819-833.
107. Shankar, R.; Ghosh, T. K.; Spontak, R. J., Dielectric elastomers as next-generation polymeric actuators. *Soft Matter* **2007,** *3* (9), 1116-1129.
108. Fei, S.-T.; Phelps, M. V. B.; Wang, Y.; Barrett, E.; Gandhi, F.; Allcock, H. R., A redox responsive polymeric gel based on ionic crosslinking. *Soft Matter* **2006,** *2* (5), 397-401.
109. Spruijt, E.; Choi, E.-Y.; Huck, W. T. S., Reversible Electrochemical Switching of Polyelectrolyte Brush Surface Energy Using Electroactive Counterions. *Langmuir* **2008,** *24* (19), 11253-11260.
110. Tomatsu, I.; Hashidzume, A.; Harada, A., Redox-responsive hydrogel system using the molecular recognition of beta -cyclodextrin. *Macromol. Rapid Commun.* **2006,** *27* (4), 238-241.

111. Tsuchiya, K.; Orihara, Y.; Kondo, Y.; Yoshino, N.; Ohkubo, T.; Sakai, H.; Abe, M., Control of Viscoelasticity Using Redox Reaction. *J. Am. Chem. Soc.* **2004,** *126* (39), 12282-12283.
112. Wang, C.; Chen, Q.; Sun, F.; Zhang, D.; Zhang, G.; Huang, Y.; Zhao, R.; Zhu, D., Multistimuli Responsive Organogels Based on a New Gelator Featuring Tetrathiafulvalene and Azobenzene Groups: Reversible Tuning of the Gel-Sol Transition by Redox Reactions and Light Irradiation. *J. Am. Chem. Soc.* **2010,** *132* (9), 3092-3096.
113. Deng, G.; Tang, C.; Li, F.; Jiang, H.; Chen, Y., Covalent Crosslinked Polymer Gels with Reversible Sol-Gel Transition and Self-Healing Properties. *Macromolecules* **2010,** *43* (3), 1191-1194.
114. White, H. S.; Leddy, J.; Bard, A. J., Polymer films on electrodes. 8. Investigation of charge-transport mechanisms in Nafion polymer modified electrodes. *J. Am. Chem. Soc.* **1982,** *104* (18), 4811-4817.
115. Du, F.; Wu, K.; Yang, Y.; Liu, L.; Gan, T.; Xie, X., Synthesis and electrochemical probing of water-soluble poly(sodium 4-styrenesulfonate-co-acrylic acid)-grafted multiwalled carbon nanotubes. *Nanotechnology* **2008,** *19* (8), 085716.
116. Abras, A.; Figueiredo de Oliveira, E., Synthesis and Mössbauer study of iron oxalate coordination polymers of the type Fe(C2O4)(L)x(H2O2-x) *Hyperfine Interactions* **1991,** *66* (1), 271-278.
117. D'Antonio, M. C.; Wladimirsky, A.; Palacios, D.; Coggiolaa, L.; González-Baró, A. C.; Baran, E. J.; Mercader, R. C., Spectroscopic investigations of iron(II) and iron(III) oxalates. *Journal of the Brazilian Chemical Society* **2009,** *20*, 445-450.
118. Gallagher, P. K.; Kurkjian, C. R., A Study of the Thermal Decomposition of Some Complex Oxalates of Iron(III) Using the Mössbauer Effect. *Inorganic Chemistry* **1966,** *5* (2), 214-219.
119. Wrobleski, J. T.; Brown, D. B., Synthesis, magnetic susceptibility, and spectroscopic properties of single- and mixed-valence iron oxalate, squarate, and dihydroxybenzoquinone coordination polymers. *Inorganic Chemistry* **1979,** *18* (10), 2738-2749.
120. Delaney, M.; Weiland, L. M. In *Experimental Characterization of Electroplastic Elastomers*, ASME 2009 Conference on Smart Materials, Adaptive Structures and Intelligent Systems SMASIS2009, Oxnard, California, Sept. 21-23 Oxnard, California, 2009.
121. Viollier, E.; Inglett, P. W.; Hunter, K.; Roychoudhury, A. N.; Van Cappellen, P., The ferrozine method revisited: Fe(II)/Fe(III) determination in natural waters. *Applied Geochemistry* **2000,** *15* (6), 785-790.
122. Hoffman, A. S., Stimuli-responsive polymers: Biomedical applications and challenges for clinical translation. *Advanced Drug Delivery Reviews* **2013,** *65* (1), 10-16.
123. Islam, M. R.; Lu, Z. Z.; Li, X.; Sarker, A. K.; Hu, L.; Choi, P.; Li, X.; Hakobyan, N.; Serpe, M. J., Responsive polymers for analytical applications: A review. *Analytica Chimica Acta* **2013,** *789*, 17-32.
124. Stuart, M. A. C.; Huck, W. T. S.; Genzer, J.; Muller, M.; Ober, C.; Stamm, M.; Sukhorukov, G. B.; Szleifer, I.; Tsukruk, V. V.; Urban, M.; Winnik, F.; Zauscher, S.; Luzinov, I.; Minko, S., Emerging applications of stimuli-responsive polymer materials. *Nature Materials* **2010,** *9* (2), 101-113.
125. Roy, D.; Cambre, J. N.; Sumerlin, B. S., Future perspectives and recent advances in stimuli-responsive materials. *Prog. Polym. Sci.* **2010,** *35* (1-2), 278-301.
126. Gracia, R.; Mecerreyes, D., Polymers with redox properties: materials for batteries, biosensors and more. *Polym. Chem.* **2013,** *4* (7), 2206-2214.

127. Sun, L.; Huang, W. M.; Ding, Z.; Zhao, Y.; Wang, C. C.; Purnawali, H.; Tang, C., Stimulus-responsive shape memory materials: A review. *Materials & Design* **2012,** *33*, 577-640.

128. Nair, K. P. N.; Breedveld, V.; Weck, M., Multiresponsive Reversible Polymer Networks Based on Hydrogen Bonding and Metal Coordination. *Macromolecules* **2011**.

129. Calvo-Marzal, P.; Delaney, M. P.; Auletta, J. T.; Pan, T.; Perri, N. M.; Weiland, L. M.; Waldeck, D. H.; Clark, W. W.; Meyer, T. Y., Manipulating Mechanical Properties with Electricity: Electroplastic Elastomer Hydrogels. *ACS Macro Lett.* **2012,** *1*, 204-208.

130. Elhabiri, M.; Albrecht-Gary, A.-M., Supramolecular edifices and switches based on metals. *Coordination Chemistry Reviews* **2008,** *252* (10+11), 1079-1092.

131. Ding, F. Y.; Shi, X. W.; Jiang, Z. W.; Liu, L.; Cai, J.; Li, Z. Y.; Chen, S.; Du, Y. M., Electrochemically stimulated drug release from dual stimuli responsive chitin hydrogel. *Journal of Materials Chemistry B* **2013,** *1* (12), 1729-1737.

132. Durot, S.; Reviriego, F.; Sauvage, J. P., Copper-complexed catenanes and rotaxanes in motion: 15 years of molecular machines. *Dalton Transactions* **2010,** *39* (44), 10557-10570.

133. Kalny, D.; Elhabiri, M.; Moav, T.; Vaskevich, A.; Rubinstein, I.; Shanzer, A.; Albrecht-Gary, A.-M., A new molecular switch: redox-driven translocation mechanism of the copper cation. *Chem. Commun. (Cambridge, U. K.)* **2002,** (13), 1426-1427.

134. Yan, X. Z.; Wang, F.; Zheng, B.; Huang, F. H., Stimuli-responsive supramolecular polymeric materials. *Chemical Society Reviews* **2012,** *41* (18), 6042-6065.

135. Delaney, M.; Clark, W.; Weiland, L. M.; Meyer, T. Y.; Pan, T., Experimental Characterization of Electroplastic Elastomers. In *ASME 2010 Conference on Smart Materials, Adaptive Structures and Intelligent Systems SMASIS2010*, Philadelphia, 2010.

136. Kranenburg, J. M.; Tweedie, C. A.; van Vliet, K. J.; Schubert, U. S., Challenges and Progress in High-Throughput Screening of Polymer Mechanical Properties by Indentation. *Advanced Materials* **2009,** *21* (35), 3551-3561.

137. Delaney, M.; Clark, W. W.; Weiland, L. M.; Meyer, T.; Pan, T., Experimental Characterization of Electroplastic Elastomers. *ASME Conference Proceedings* **2010,** *2010* (44168), 121-127.

138. Gahler, A. R., Colorimetric Determination of Copper with Neo-Cuproine. *Analytical Chemistry* **1954,** *26* (3), 577-579.

139. Peisach, J.; Blumberg, W. E., Structural implications derived from the analysis of electron paramagnetic resonance spectra of natural and artificial copper proteins. *Archives of Biochemistry and Biophysics* **1974,** *165* (2), 691-708.

140. Calvo-Marzal, P.; Delaney, M. P.; Auletta, J. T.; Pan, T.; Perri, N. M.; Weiland, L. M.; Waldeck, D. H.; Clark, W. W.; Meyer, T. Y., Manipulating Mechanical Properties with Electricity: Electroplastic Elastomer Hydrogels. *ACS Macro Letters* **2012**, 204-208.

141. Yang, Y.; Urban, M. W., Self-healing polymeric materials. *Chemical Society Reviews* **2013,** *42* (17), 7446-7467.

142. Durot, S.; Reviriego, F.; Sauvage, J.-P., Copper-complexed catenanes and rotaxanes in motion: 15 years of molecular machines. *Dalton Transactions* **2010,** *39* (44), 10557-10570.

143. Kalny, D.; Elhabiri, M.; Moav, T.; Vaskevich, A.; Rubinstein, I.; Shanzer, A.; Albrecht-Gary, A.-M., A new molecular switch: redox-driven translocation mechanism of the copper cation. *Chemical Communications* **2002,** (13), 1426-1427.

144. Kawano, S.-i.; Fujita, N.; Shinkai, S., A Coordination Gelator That Shows a Reversible Chromatic Change and Sol−Gel Phase-Transition Behavior upon Oxidative/Reductive Stimuli. *Journal of the American Chemical Society* **2004,** *126* (28), 8592-8593.

145. Harris, R. D.; Auletta, J. T.; Motlagh, S. A. M.; Lawless, M. J.; Perri, N. M.; Saxena, S.; Weiland, L. M.; Waldeck, D. H.; Clark, W. W.; Meyer, T. Y., Chemical and Electrochemical Manipulation of Mechanical Properties in Stimuli-Responsive Copper-Cross-Linked Hydrogels. *ACS Macro Letters* **2013,** *2* (12), 1095-1099.
146. Palleau, E.; Morales, D.; Dickey, M. D.; Velev, O. D., Reversible patterning and actuation of hydrogels by electrically assisted ionoprinting. *Nature Communications* **2013,** *4*.
147. Cong, H.-P.; Wang, P.; Yu, S.-H., Stretchable and Self-Healing Graphene Oxide-Polymer Composite Hydrogels: A Dual-Network Design. *Chem. Mater.* **2013,** *25* (16), 3357-3362.
148. Zhang, H.; Zhai, D.; He, Y., Graphene oxide/polyacrylamide/carboxymethyl cellulose sodium nanocomposite hydrogel with enhanced mechanical strength: preparation, characterization and the swelling behavior. *RSC Advances* **2014,** *4* (84), 44600-44609.
149. Wu, L.; Ohtani, M.; Takata, M.; Saeki, A.; Seki, S.; Ishida, Y.; Aida, T., Magnetically Induced Anisotropic Orientation of Graphene Oxide Locked by in Situ Hydrogelation. *ACS Nano* **2014,** *8* (5), 4640-4649.
150. Yao, F.; Güneş, F.; Ta, H. Q.; Lee, S. M.; Chae, S. J.; Sheem, K. Y.; Cojocaru, C. S.; Xie, S. S.; Lee, Y. H., Diffusion Mechanism of Lithium Ion through Basal Plane of Layered Graphene. *Journal of the American Chemical Society* **2012,** *134* (20), 8646-8654.
151. Liu, J.; Chen, C.; He, C.; Zhao, J.; Yang, X.; Wang, H., Synthesis of Graphene Peroxide and Its Application in Fabricating Super Extensible and Highly Resilient Nanocomposite Hydrogels. *ACS Nano* **2012,** *6* (9), 8194-8202.
152. Liu, J.; Song, G.; He, C.; Wang, H., Self-Healing in Tough Graphene Oxide Composite Hydrogels. *Macromol. Rapid Commun.* **2013,** *34* (12), 1002-1007.
153. Cong, H.-P.; Wang, P.; Yu, S.-H., Highly Elastic and Superstretchable Graphene Oxide/Polyacrylamide Hydrogels. *Small* **2014,** *10* (3), 448-453.
154. Fan, J.; Shi, Z.; Wang, J.; Yin, J., Glycidyl methacrylate-modified gum arabic mediated graphene exfoliation and its use for enhancing mechanical performance of hydrogel. *Polymer* **2013,** *54* (15), 3921-3930.
155. Lin, J.; Tang, Q.; Wu, J.; Hao, S., The synthesis and electrical conductivity of a polyacrylate/graphite hydrogel. *Reactive and Functional Polymers* **2007,** *67* (4), 275-281.
156. Liu, K.; Li, Y.; Xu, F.; Zuo, Y.; Zhang, L.; Wang, H.; Liao, J., Graphite/poly (vinyl alcohol) hydrogel composite as porous ringy skirt for artificial cornea. *Materials Science and Engineering: C* **2009,** *29* (1), 261-266.
157. Tang, Q.; Lin, J.; Wu, J., The preparation and electrical conductivity of polyacrylamide/graphite conducting hydrogel. *Journal of Applied Polymer Science* **2008,** *108* (3), 1490-1495.
158. Fan, S.; Tang, Q.; Wu, J.; Hu, D.; Sun, H.; Lin, J., Two-step synthesis of polyacrylamide/poly(vinyl alcohol)/polyacrylamide/graphite interpenetrating network hydrogel and its swelling, conducting and mechanical properties. *Journal of Materials Science* **2008,** *43* (17), 5898-5904.
159. Feng, H.; Li, Y.; Li, J., Strong reduced graphene oxide-polymer composites: hydrogels and wires. *RSC Adv.* **2012,** *2* (17), 6988-6993.
160. Hirata, M.; Gotou, T.; Horiuchi, S.; Fujiwara, M.; Ohba, M., Thin-film particles of graphite oxide 1:: High-yield synthesis and flexibility of the particles. *Carbon* **2004,** *42* (14), 2929-2937.

161. Cong, H.-P.; Ren, X.-C.; Wang, P.; Yu, S.-H., Macroscopic Multifunctional Graphene-Based Hydrogels and Aerogels by a Metal Ion Induced Self-Assembly Process. *Acs Nano* **2012,** *6* (Copyright (C) 2012 American Chemical Society (ACS). All Rights Reserved.), 2693-2703.
162. Fan, Z.-J.; Kai, W.; Yan, J.; Wei, T.; Zhi, L.-J.; Feng, J.; Ren, Y.-m.; Song, L.-P.; Wei, F., Facile Synthesis of Graphene Nanosheets via Fe Reduction of Exfoliated Graphite Oxide. *Acs Nano* **2010,** *5* (1), 191-198.
163. Gran, G., Determination of the equivalence point in potentiometric titrations. Part II. *Analyst* **1952,** *77* (920), 661-671.
164. Grabiel, C. E.; Decker, D. L., Copolymerization characteristics of sodium styrenesulfonate. *Journal of Polymer Science* **1962,** *59* (168), 425-431.
165. Morlay, C.; Cromer, M.; Mouginot, Y.; Vittori, O., Potentiometric study of Cu(II) and Ni(II) complexation with two high molecular weight poly(acrylic acids). *Talanta* **1998,** *45* (6), 1177-1188.
166. Gregor, H. P.; Luttinger, L. B.; Loebl, E. M., Metal–Polyelectrolyte Complexes. I. The Polyacrylic Acid–Copper Complex. *The Journal of Physical Chemistry* **1955,** *59* (1), 34-39.
167. Mouginot, Y.; Morlay, C.; Cromer, M.; Vittori, O., Potentiometric study of copper(II) and nickel(II) complexation by a cross-linked poly(acrylic acid) gel. *Analytica Chimica Acta* **2000,** *407* (1–2), 337-345.
168. Andelman, J. B.; Hoeschele, G. K.; Gregor, H. P., Metal-Polyelectrolyte Complexes. VI. Preparation and Properties of a New Polychelate–Polyvinylmethylglyoxime. *The Journal of Physical Chemistry* **1959,** *63* (2), 206-210.
169. Hoeschele, G. K.; Andelman, J. B.; Gregor, H. P., Metal–Polyelectrolyte Complexes. V. Preparation and Properties of a New Polychelate–Polyvinylacetonyl Ketone. *The Journal of Physical Chemistry* **1958,** *62* (10), 1239-1244.
170. Diani, J.; Fayolle, B.; Gilormini, P., A review on the Mullins effect. *European Polymer Journal* **2009,** *45* (3), 601-612.
171. Yokoi, H.; Nishi, H., Interaction mode between poly(acrylic acid) and ferric ions. Gelation mechanism of the system. *Chem. Lett.* **1989,** (10), 1765-8.
172. Dziobkowski, C. T.; Wrobleski, J. T.; Brown, D. B., Magnetic properties and Moessbauer spectra of several iron(III)-dicarboxylic acid complexes. *Inorganic Chemistry* **1981,** *20* (3), 671-678.
173. Johnson, M. K.; Powell, D. B.; Cannon, R. D., Vibrational spectra of carboxylato complexes—III. Trinuclear 'basic' acetates and formates of chromium(III), iron(III) and other transition metals. *Spectrochimica Acta, Part A: Molecular Spectroscopy* **1981,** *37* (11), 995-1006.
174. Fernandes, C.; Stadler, E.; Drago, V.; Jorge da Cunha, C.; Hiroko Kuwabara, I., Mössbauer, vibrational and electronic spectroscopy of trinuclear μ-oxo iron(III) acetate clusters with pyridine and derivatives as ligands. *Spectrochimica Acta Part A: Molecular and Biomolecular Spectroscopy* **1996,** *52* (14), 1815-1821.
175. Blake, A. B.; Sinn, E.; Yavari, A.; Murray, K. S.; Moubaraki, B., Oxo-centred trinuclear acetate complexes containing mixed-metal clusters. Crystal structure of a chromium(III)iron(III)nickel(II) complex and magnetic properties of a dichromium(III)magnesium(II) complex [double dagger]. *Journal of the Chemical Society, Dalton Transactions* **1998,** (1), 45-50.

176. Amani, V.; Safari, N.; Khavasi, H. R., Solution and solid state characterization of oxo-centered trinuclear iron(III) acetate complexes [Fe3(μ3-O)(μ-OAc)6(L)3]+. *Spectrochimica Acta Part A: Molecular and Biomolecular Spectroscopy* **2012,** *85* (1), 17-24.

177. Falk, B.; Garramone, S.; Shivkumar, S., Diffusion coefficient of paracetamol in a chitosan hydrogel. *Materials Letters* **2004,** *58* (26), 3261-3265.

178. Suk, J. W.; Piner, R. D.; An, J.; Ruoff, R. S., Mechanical Properties of Monolayer Graphene Oxide. *ACS Nano* **2010,** *4* (11), 6557-6564.

179. Kulkarni, D. D.; Choi, I.; Singamaneni, S. S.; Tsukruk, V. V., Graphene Oxide−Polyelectrolyte Nanomembranes. *Acs Nano* **2010,** *4* (8), 4667-4676.

180. Affdl, J. C. H.; Kardos, J. L., The Halpin-Tsai equations: A review. *Polymer Engineering & Science* **1976,** *16* (5), 344-352.

181. Auletta, J. T.; Ledonne, G. J.; Gronborg, K. C.; Ladd, C. D.; Liu, H.; Clark, W. W.; Meyer, T. Y., Stimuli-responsive iron-cross-linked hydrogels that undergo redox-driven switching between hard and soft states. *Macromolecules* **2015,** *48* (6), 1736-1747.

182. Calvo-Marzal, P.; Delaney, M. P.; Auletta, J. T.; Pan, T.; Perri, N. M.; Weiland, L. M.; Waldeck, D. H.; Clark, W. W.; Meyer, T. Y., Manipulating mechanical properties with electricity: Electroplastic elastomer hydrogels. *ACS Macro Letters* **2012,** *1* (1), 204-208.

183. Gabriel, M.; Farhan, G., Multi-layered controllable stiffness beams for morphing: energy, actuation force, and material strain considerations. *Smart Materials and Structures* **2010,** *19* (4), 045002.

184. Mather, P. T. L., Xiaofan; and Rousseau, Ingrid A. , Shape Memory Polymer Research. *Annual Review of Materials Research* **2009,** *39* (1), 445-471.

185. Ruffatto, D.; Parness, A.; Spenko, M., *Improving controllable adhesion on both rough and smooth surfaces with a hybrid electrostatic/gecko-like adhesive*. 2014; Vol. 11.

186. Ruffatto, D.; Shah, J.; Spenko, M. In *Optimization and experimental validation of electrostatic adhesive geometry,* Aerospace Conference, 2013 IEEE, 2-9 March 2013; 2013; pp 1-8.

187. Graule, M. A.; Chirarattananon, P.; Fuller, S. B.; Jafferis, N. T.; Ma, K. Y.; Spenko, M.; Kornbluh, R.; Wood, R. J., Perching and takeoff of a robotic insect on overhangs using switchable electrostatic adhesion. *Science* **2016,** *352* (6288), 978-982.

188. Radon, D.; Kenji, S.; Kunio, T.; Wataru, T.; Takeshi, K.; Shigeki, S., Electrostatic chuck consisting of polymeric electrostatic inductive fibers for handling of objects with rough surfaces. *Smart Materials and Structures* **2013,** *22* (9), 095010.

189. Shultz, C. D.; Peshkin, M. A.; Colgate, J. E. In *Surface haptics via electroadhesion: Expanding electrovibration with Johnsen and Rahbek*, World Haptics Conference (WHC), 2015 IEEE, 22-26 June 2015; 2015; pp 57-62.

190. Qin, S.; McTeer, A., Wafer dependence of Johnsen--Rahbek type electrostatic chuck for semiconductor processes. *Journal of Applied Physics* **2007,** *102* (6), 064901.

191. Qin, S.; McTeer, A., Deep-depletion breakdown of Johnsen–Rahbek type electrostatic chuck operation for semiconductor processes. *Journal of Applied Physics* **2008,** *104* (9), -.

192. Shim, G. I.; Sugai, H., Dechuck Operation of Coulomb Type and Johnsen-Rahbek Type of Electrostatic Chuck Used in Plasma Processing. *Plasma Fusion Res.* **2008,** *3* (051).

193. Sogard, M. R.; Mikkelson, A. R.; Nataraju, M.; Turner, K. T.; Engelstad, R. L., Analysis of Coulomb and Johnsen-Rahbek electrostatic chuck performance for extreme ultraviolet lithography. *Journal of Vacuum Science & Technology B* **2007,** *25* (6), 2155-2161.

194. Sogard, M. R.; Mikkelson, A. R.; Ramaswamy, V.; Engelstad, R. L. In *Analysis of Coulomb and Johnsen-Rahbek electrostatic chuck performance in the presence of particles for EUV lithography*, 2009; pp 72710H-72710H-14.
195. Callum, J. C. H.; Robin, M. N.; Fabrizio, S.; Ian, P. B.; Kevin, D. P., Morphing hybrid honeycomb (MOHYCOMB) with in situ Poisson's ratio modulation. *Smart Materials and Structures* **2016,** *25* (8), 085008.
196. Bergamini, A.; Christen, R.; Maag, B.; Motavalli, M., A sandwich beam with electrostatically tunable bending stiffness. *Smart Materials and Structures* **2006,** *15* (3), 678.
197. Bergamini, A.; Christen, R.; Motavalli, M., Electrostatically tunable bending stiffness in a GFRP–CFRP composite beam. *Smart Materials and Structures* **2007,** *16* (3), 575.
198. Kuder, I. K.; Arrieta, A. F.; Raither, W. E.; Ermanni, P., Variable stiffness material and structural concepts for morphing applications. *Progress in Aerospace Sciences* **2013,** *63*, 33-55.
199. Greenwood, J. A., Constriction resistance and the real area of contact. *British Journal of Applied Physics* **1966,** *17* (12), 1621.
200. Greenwood, J. A.; Williamson, J. B. P., Contact of Nominally Flat Surfaces. *Proceedings of the Royal Society of London A: Mathematical, Physical and Engineering Sciences* **1966,** *295* (1442), 300-319.
201. Johnsen, A.; Rahbek, K., A physical phenomenon and its applications to telegraphy, telephony, etc. *Electrical Engineers, Journal of the Institution of* **1923,** *61* (320), 713-725.
202. Watanabe, T.; Kitabayashi, T.; Nakayama, C., Electrostatic Force and Absorption Current of Alumina Electrostatic Chuck. *Japanese Journal of Applied Physics* **1992,** *31* (Part 1, No. 7), 2145.
203. Kanno, S.; Kato, K.; Yoshioka, K.; Nishio, R.; Tsubone, T., Prediction of clamping pressure in a Johnsen-Rahbek-type electrostatic chuck based on circuit simulation. *Journal of Vacuum Science & Technology B* **2006,** *24* (1), 216-223.
204. Balakrishnan, C., Johnsen-Rahbek Effect with an Electronic Semi-Conductor. *British Journal of Applied Physics* **1950,** *1* (8), 211.
205. Stuckes, A. D., Some theoretical and practical considerations of the Johnsen-Rahbek effect. *Proceedings of the IEE - Part B: Radio and Electronic Engineering* **1956,** *103* (8), 125-131.
206. Atkinson, R., A simple theory of the Johnsen-Rahbek effect. *Journal of Physics D: Applied Physics* **1969,** *2* (3), 325.
207. Watanabe, T.; Kitabayashi, T., Effect of Additives on the Electrostatic Force of Alumina Electrostatic Chucks. *Journal of the Ceramic Society of Japan* **1992,** *100* (1157), 1-6.
208. Di Lillo, L.; Carnelli, D. A.; Bergamini, A.; Busato, S.; Ermanni, P., Quasi-static electric properties of insulating polymers at a high voltage for electro-bonded laminates. *Smart Materials and Structures* **2011,** *20* (5), 057002.
209. Di Lillo, L.; Raither, W.; Bergamini, A.; Zündel, M.; Ermanni, P., Tuning the mechanical behaviour of structural elements by electric fields. *Applied Physics Letters* **2013,** *102* (22), 224106.
210. Ginés, R.; Bergamini, A.; Christen, R.; Motavalli, M.; Ermanni, P., Frictional behaviour of polymer films under mechanical and electrostatic loads. *Smart Materials and Structures* **2013,** *22* (7), 075023.
211. Tabata, O.; Konishi, S.; Cusin, P.; Ito, Y.; Kawai, F.; Hirai, S.; Kawamura, S. In *Microfabricated tunable bending stiffness device*, Micro Electro Mechanical Systems, 2000.

MEMS 2000. The Thirteenth Annual International Conference on, 23-27 Jan 2000; 2000; pp 23-27.

212. Callum, J. C. H.; Ian, P. B.; Kevin, D. P., Electrostatic adhesion for added functionality of composite structures. *Smart Materials and Structures* **2016,** *25* (2), 025016.

213. Baughman, T. W.; Chan, C. D.; Winey, K. I.; Wagener, K. B., Synthesis and Morphology of Well-Defined Poly(ethylene-co-acrylic acid) Copolymers. *Macromolecules* **2007,** *40* (18), 6564-6571.

214. Rúan-Esparza, L.; Soto, V.; Gómez-Salazar, S.; Rabelero, M.; Ávalos-Borja, M.; Luna-Bárcenas, G.; Prokhorov, E.; Nuño-Donlucas, S. M., Poly[ethylene-co-(acrylic acid)]-based nanocomposites: Thermal and mechanical properties and their structural characteristics studied by Raman spectroscopy. *Polymer Composites* **2011,** *32* (8), 1181-1189.

215. Schönhals, A.; Kremer, F., Analysis of Dielectric Spectra. In *Broadband Dielectric Spectroscopy*, Kremer, F.; Schönhals, A., Eds. Springer Berlin Heidelberg: Berlin, Heidelberg, 2003; pp 59-98.

216. ASTM, Standard Test Methods for Flexural Properties of Unreinforced and Reinforced Plastics and Electrical Insulating Materials. ASTM International: 2010; Vol. Standard D790.

217. Seitz, M. E.; Chan, C. D.; Opper, K. L.; Baughman, T. W.; Wagener, K. B.; Winey, K. I., Nanoscale Morphology in Precisely Sequenced Poly(ethylene-co-acrylic acid) Zinc Ionomers. *Journal of the American Chemical Society* **2010,** *132* (23), 8165-8174.

218. Weiss, R. A.; Agarwal, P. K.; Lundberg, R. D., Control of ionic interactions in sulfonated polystyrene ionomers by the use of alkyl-substituted ammonium counterions. *Journal of Applied Polymer Science* **1984,** *29* (9), 2719-2734.

219. Green, M. D.; Salas-de la Cruz, D.; Ye, Y.; Layman, J. M.; Elabd, Y. A.; Winey, K. I.; Long, T. E., Alkyl-Substituted N-Vinylimidazolium Polymerized Ionic Liquids: Thermal Properties and Ionic Conductivities. *Macromolecular Chemistry and Physics* **2011,** *212* (23), 2522-2528.

220. Marcus, Y., Tetraalkylammonium Ions in Aqueous and Non-aqueous Solutions. *Journal of Solution Chemistry* **2008,** *37* (8), 1071-1098.

221. Stevens, M. P., *Polymer Chemistry: An Introduction*. Addison-Wesley Publishing Company, Advanced Book Program: 1975.

222. Cipriano, R. A.; Longoria, J. J., Electroresponsive polymer systems. Google Patents: 1996.

223. Greenspan, L., Humidity Fixed Points of Binary Saturated Aqueous Solutions. *Journal of Research of the National Bureau of Standards - A. Physics and Chemistry* **1976,** *81A* (1), 8.

224. Timoshenko, S.; Goodier, J. N., *Theory of Elasticity*. 2nd ed.; McGraw-Hill: 1951.